A Search for the Top Quark decaying to the Charged Higgs Boson in $p\bar{p}$ collisions at $\sqrt{s}$=1.8 TeV

A thesis presented

by

Colin Philip Jessop

to

The Department of Physics

in partial fulfillment of the requirements
for the degree of

Doctor of Philosophy

in the subject of

Physics

Harvard University
Cambridge, Massachussetts
December 1993

© 1993 by Colin Philip Jessop
All rights reserved.

Abstract

We present results of a search for the top quark decaying to a charged Higgs boson (H) in $p\bar{p}$ collisions at $\sqrt{s} = 1.8$ TeV at the Fermilab Tevatron. Using 4.1 pb^{-1} of data collected during the 1988-89 CDF run, we have searched for evidence of $t\bar{t}$ production assuming that $t \rightarrow Hb$ and $H \rightarrow \tau\nu_\tau$. We find no evidence for this decay and are able to exclude regions in the (m_t, m_H) plane for different $Br(H \rightarrow \tau\nu_\tau)$. We also interpret these results for the two Higgs doublet model.

Contents

Abstract ii

Table of Contents iii

List of Tables vii

List of Figures viii

Acknowledgments xvi

1 Introduction and Theory 1

1.1 Evidence for the existence of the top quark 2

1.2 The Higgs boson 6

1.3 Constraints on the Higgs bosons 15

1.4 Naturalness and the Higgs Boson 16

1.5 The two Higgs doublet model 18

1.6 The top quark decaying to a charged Higgs 23

1.7 Experimental limits on $m_t, m_{H^+}, \tan\beta$ 25

1.7.1 LEP constraints 25

1.7.2 Constraints from low energy data (mixing and CP violation) 26

1.7.3 Penguin decays of bottom quark 28

1.7.4 Constraints on m_t 29

1.7.5 Limits from $p\bar{p}$ experiments 31

1.8 Theoretical Constraints on $m_t, m_{H^+}, \tan\beta$ 32
1.9 CDF search region 33

2 The Collider Detector at Fermilab **40**
2.1 Tracking detectors 43
2.1.1 The vertex time projection chamber 45
2.1.2 The central tracking chamber 48
2.2 Calorimeters 50
2.2.1 The central calorimeters 51
2.2.2 Plug calorimeters 52
2.2.3 The forward calorimeters 53
2.3 The muon detectors 53
2.4 Trigger 54
2.4.1 Level 0 trigger 54
2.4.2 Level 1 trigger 55
2.4.3 Level 2 trigger 55
2.4.4 Level 3 trigger 56
2.5 Front end electronics and detector readout 56
2.6 1988-1989 run 58

3 Event Reconstruction and Selection **60**
3.1 Event reconstruction 61
3.1.1 Vertex reconstruction 61
3.1.2 Energy reconstruction 62
3.1.3 Track reconstruction 63
3.2 Top to Higgs signature 64
3.2.1 Other possible signatures 65
3.3 Missing transverse energy trigger 66
3.3.1 Description of the trigger 66
3.3.2 Estimation of trigger efficiency 68
3.4 Data stream selection 75

3.4.1 Jet clustering algorithm 75
3.4.2 The data stream - event topology cuts 76
3.5 Defining a hadronic tau algorithm 82
3.5.1 Hadronic tau cluster requirements 83
3.5.2 Hadronic tau track requirements 86
3.5.3 Electron removal 90
3.5.4 Summary of tau algorithm cuts 95
3.6 Testing the hadronic tau algorithm 97
3.7 Defining a top to charged Higgs signature using hadronic taus $\not{E}_T$ and jets 103
3.8 Calculation of overall efficiency 104

4 Computing the Expected Number of Signal events and the Error 106

4.1 Theoretical calculation of $t\bar{t}$ cross sections 107
4.1.1 Outline of the calculation 107
4.1.2 Uncertainties in the calculation 108
4.2 The ISAJET Monte Carlo 114
4.3 Systematic errors in N_{expect} 119
4.3.1 Uncertainty in energy scale (E_{es}) 119
4.3.2 Modeling of gluon radiation (E_{gl}) 119
4.3.3 Uncertainty in tau branching ratio (E_{br}) 120
4.3.4 Monte Carlo statistics (E_{mc}) 120
4.3.5 Uncertainty in trigger efficiency (E_{tr}) 121
4.3.6 Uncertainty in integrated luminosity (E_{lu}) 121
4.3.7 Uncertainty in Peterson fragmentation parameter 121
4.3.8 Uncertainty in underlying event modeling 121
4.4 N_{expect} for different m_{H^+}, m_t for $Br(H^+ \rightarrow \tau\nu_\tau) = 1.0$, $Br(t \rightarrow H^+b) = 1.0$ 121

4.5 N_{expect} for different m_{H^+}, m_t for $Br(H^+ \to \tau\nu_\tau) < 1.0$, $Br(t \to H^+b) < 1.0$ 122

5 Results **129**

5.1 Signal with background 130

5.2 Subtraction of QCD and electron background 131

5.3 Estimation of vector boson background 131

5.4 Final result 134

6 Limits **135**

6.1 Model independent limits 136

6.2 Limits for the two Higgs doublet model 137

6.2.1 Model I 137

6.2.2 Model II 138

6.2.3 Model III 138

6.2.4 Model IV 139

7 Conclusions **140**

A Electron Cuts **141**

B $W \to \tau\nu$ analysis cuts **142**

List of Tables

1.1 Averages of Z decay data observables with references 4

1.2 The possible couplings of the Higgs doublets to fermions in the two Higgs doublet model. 20

3.1 A summary of the data stream selection cuts and the efficiencies for simulated (ISAJET) $p\bar{p} \rightarrow t\bar{t} \rightarrow H^+H^-b\bar{b}$, $H^\pm \rightarrow \tau\nu$ events (m_{H^+}=50 GeV, m_t=70 GeV) . The efficiencies are calculated sequentially. The total is the product. 81

3.2 Tau decay branching ratios 82

3.3 The probability of a track from the underlying event with: $P_T >$ 1.0, 2.5 GeV lying in the 7.5 ^{o} cone , $P_T >$ 1.0 GeV lying in the 7.5 ^{o} -17.5 ^{o} annulus. 88

3.4 A summary of the tau algorithm cuts and the efficiencies for simulated (ISAJET) $p\bar{p} \rightarrow t\bar{t} \rightarrow H^+H^-b\bar{b}$, $H^\pm \rightarrow \tau\nu$ events (m_{H^+}=50 GeV, m_t=70 GeV) . The efficiencies are calculated sequentially. The total is the product. 95

4.1 The $t\bar{t}$ production cross sections at 1.8 TeV from Ellis *et al.*, with upper and lower bounds due to the theoretical uncertainty in the calculation 110

4.2 Acceptances and errors for $p\bar{p} \rightarrow t\bar{t} \rightarrow H^+H^-b\bar{b} \rightarrow \tau^+\tau^-b\bar{b}$ . . 126

4.3 Acceptances and errors for $p\bar{p} \rightarrow t\bar{t} \rightarrow H^+W^-b\bar{b} \rightarrow \tau^+W^-b\bar{b}$ . . 127

4.4 Acceptances and errors for $p\bar{p} \rightarrow t\bar{t} \rightarrow H^+H^-b\bar{b} \rightarrow \tau c\bar{s}b\bar{b}$ 128

List of Figures

1-1 The Feynman diagrams for the processes $B(B \to l^+l^-X)$, $B(B \to l\nu_l)$, which involve flavor changing neutral currents. 3

1-2 Allowed regions of the (I_3^L, I_3^R) plane, inferred from Z decay data. The circular region allows two possible half integer assignments, (I_3^L, I_3^R)=(0,-0.5) or (-0.5,0). The allowed region between the intersecting straight lines discriminates between the two possibilities and allows only (I_3^L, I_3^R)=(-0.5,0.0) 5

1-3 The Higgs potential. The minima is the physical vacuum. Rotational perturbations around the minima correspond to massless Goldstone bosons. Radial perturbations about the minima correspond to massive Higgs bosons. 11

1-4 A comparison of the charged Higgs and W^+ boson couplings for quarks. U denotes the "up" type quarks u,c,t and d denotes the "down" type quarks d,s,b. The couplings of the charged Higgs to the lepton currents is similar except that m_u is replaced by m_l, m_d is replaced by m_ν=0, and A_u is replaced by A_l. 21

1-5 The Feynman diagrams for $B - \bar{B}$ mixing, and for top quark decay involving the charged Higgs. The dominant decay modes of the charged Higgs are $c\bar{s}, \tau\nu_\tau$. 22

1-6 The branching ratio of $H^+ \to \tau\nu_\tau$ for the two Higgs doublet model 23

1-7 The excluded regions of the m_{H^+}, $Br(H^+ \to \tau\nu_\tau)$ plane from L3 data at 95 % confidence limit 26

1-8 The Feynman "penguin" diagram for the process $b \to s\gamma$ 28

1-9 The dependence of the total width of the W^+ boson on the mass of the top quark. 30

1-10 The excluded regions of m_t, m_{H^+} for $Br(H^+ \rightarrow \tau\nu_\tau) > 0.95$ from UA1 experiment, at 95 % confidence limit. Also shown are the limits on m_{H^+} and m_t which are independent of $Br(H^+ \rightarrow \tau\nu_\tau)$ from LEP data. The region in which W^+ boson decays are suppressed $m_t < m_{W^+} + m_b$, $m_{H^+} < m_t - m_b$ is also shown . . . 31

1-11 The excluded regions of the m_t, m_{H^+} plane for $Br(H^+ \rightarrow \tau\nu_\tau) > 0.5, 1.0$ from UA2 experiment, at 95 % confidence limit. Also shown are the limits on m_{H^+} and m_t which are independent of $Br(H^+ \rightarrow \tau\nu_\tau)$. The region in which W^+ boson decays are suppressed $m_t < m_{W^+} + m_b$, $m_{H^+} < m_t - m_b$ is also shown . . . 32

1-12 The $Br(t \rightarrow H^+b)$ for $m_t = 70.0$ GeV , $m_{H^+} = 50$ GeV for model I of the two Higgs doublet model. 35

1-13 The $Br(t \rightarrow H^+b)$ for m_t, m_{H^+} in Model I of the two Higgs doublet model. 36

1-14 The branching ratio, $Br(t \rightarrow H^+b)$, for $m_t = 80.0$ GeV and different m_{H^+} showing the minimum at $\tan\beta_{min}$. 37

1-15 The minimum $Br(t \rightarrow H^+b)$ for m_t, m_{H^+} at $\tan\beta_{min}$. 38

2-1 The Collider Detector at Fermilab (CDF) showing the movable central detector and fixed forward/background detector. Only half the detector is shown. The other half is the mirror image of that shown. 42

2-2 The definition of a co-ordinate system for the CDF detector. . . 43

2-3 The vertex time projection chamber. 44

2-4 A typical event in the vertex time projection chamber. The reconstructed track segments for the eight octants are shown. . 47

2-5 The superlayer structure of the central tracking chamber. 48

2-6 The $\eta - \phi$ segmentation of the CDF calorimeter. Also shown is the size of a cone cluster with a 0.4 radius. This is the cone clustering radius used in the analysis. 50
2-7 A CEM module. 51
2-8 A schematic of the CDF FASTBUS based DAQ system. 57
2-9 The integrated luminosity delivered compared to the integrated luminosity collected. 58

3-1 The $\not{E}_T$ for simulated (ISAJET) $p\bar{p} \rightarrow t\bar{t} \rightarrow H^+H^-b\bar{b}$, $H^\pm \rightarrow \tau\nu$ events (m_{H^+}=50 GeV, m_t=70 GeV) and for jets from a jet trigger data set. The jet data set is formed by requiring a jet cluster with $E_T > 20$ GeV. The normalization of the two distributions is arbitrary. Also shown is the $\not{E}_T$ trigger efficiency. 68
3-2 The $\not{E}_T$ trigger efficiency from data. The two plots are from a) an inclusive electron data set which required a 12 GeV electromagnetic trigger cluster b) a jet data set which required a 60 GeV trigger cluster. 70
3-3 The trigger efficiency for the electromagnetic cluster requirement of the $\not{E}_T$ trigger ($E_{T1}^{em} > 8$ GeV, $|\eta| < 2.4$) computed from a jet data data set which required a trigger cluster with $E_T > 60$ GeV. Only non-trigger clusters were used to avoid bias. 71
3-4 The $\not{E}_T$ trigger efficiency calculated with simulated data and compared to electron and jet data. The simulation is ISAJET followed by a detector and trigger simulation. The electron data required a trigger cluster with electromagnetic energy $E_T > 12$ GeV. The jet data set required a trigger cluster with $E_T > 60$ GeV 72

3-5 The E_{T1}^{em} trigger efficiency from simulation data compared to jet data. The simulated data is ISAJET followed by a detector and trigger simulation. The jet data required a trigger cluster with $E_T > 60$ GeV. 73

3-6 The azimulthal angle between the leading jet and next-to- leading jet for simulated (ISAJET) $p\bar{p} \rightarrow t\bar{t} \rightarrow H^+H^-b\bar{b}$, $H^\pm \rightarrow \tau\nu$ events (m_{H^+}=50 GeV, m_t=70 GeV) and for jet events from a data set which required a trigger cluster of $E_T > 20$ GeV. The normalization is arbitrary. 77

3-7 The $\not{E}_T$ for a) the $\not{E}_T$ data set after the trigger and $\not{E}_T$ filter and b) simulated (ISAJET) $p\bar{p} \rightarrow t\bar{t} \rightarrow H^+H^-b\bar{b}$, $H^\pm \rightarrow \tau\nu$ events (m_{H^+}=50 GeV, m_t=70 GeV) after the same cuts. 78

3-8 The Z_{vertex} for a) $\not{E}_T$ data set events after the trigger and $\not{E}_T$ filter cuts have been passed and b) for simulated (ISAJET) $p\bar{p} \rightarrow t\bar{t} \rightarrow H^+H^-b\bar{b}$, $H^\pm \rightarrow \tau\nu$ events (m_{H^+}=50 GeV, m_t=70 GeV) after the same cuts. 79

3-9 The dependence of $\sigma_{\not{E}_x}/(\sum E_T)^{1/2}$ on $\sum E_T$ in minimum bias events in which we expect no $\not{E}_T$. A straight line fit indicates that the slope is 0.47. 80

3-10 The missing transverse energy significance for a) the $\not{E}_T$ data set events, after the trigger, $\not{E}_T$ filter, Z_{vertex} and $\not{E}_T$ cuts, and b) simulated (ISAJET) $p\bar{p} \rightarrow t\bar{t} \rightarrow H^+H^-b\bar{b}$, $H^\pm \rightarrow \tau\nu$ events (m_{H^+}=50 GeV, m_t=70 GeV) after the same cuts 80

3-11 The reconstructed/generated energy for taus as a function of cone cluster radius. The taus are from simulated (ISAJET) $p\bar{p} \rightarrow t\bar{t} \rightarrow H^+H^-b\bar{b}$, $H^\pm \rightarrow \tau\nu$ events (m_{H^+}=50 GeV, m_t=70 GeV) 84

3-12 a) The generated η of taus in simulated (ISAJET) $p\bar{p} \rightarrow t\bar{t} \rightarrow H^+H^-b\bar{b}$, $H^\pm \rightarrow \tau\nu$ events (m_{H^+}=50 GeV, m_t=70 GeV) . b) The generated P_T and reconstructed E_T of taus with $0.1 < |\eta| < 1.0$. All events are required to pass the trigger and data stream requirements. Also shown are the selection cuts $0.1 < |\eta| < 1.0$, $E_T > 15$ GeV. 85

3-13 The maximum angle of tracks from tau cluster axis for taus in simulated (ISAJET) $p\bar{p} \rightarrow t\bar{t} \rightarrow H^+H^-b\bar{b}$, $H^\pm \rightarrow \tau\nu$ events (m_{H^+}=50 GeV, m_t=70 GeV) . Also shown is the equivalent cone radius R. 86

3-14 a) P_T of leading tau tracks for taus in simulated (ISAJET) $p\bar{p} \rightarrow t\bar{t} \rightarrow H^+H^-b\bar{b}$, $H^\pm \rightarrow \tau\nu$ events (m_{H^+}=50 GeV, m_t=70 GeV) . Also shown is the same distribution for jets from a jet data sample. b) The P_T of tracks in minimum bias events 87

3-15 The number of tracks with $P_T > 1.0$ GeV in a 7.5^o- 17.5^o annulus about the tau cluster centroid for taus in simulated (ISAJET) $p\bar{p} \rightarrow t\bar{t} \rightarrow H^+H^-b\bar{b}$, $H^\pm \rightarrow \tau\nu$ events (m_{H^+}=50 GeV, m_t=70 GeV) 89

3-16 The fraction of the total cluster energy which is electromagnetic for taus in simulated (ISAJET) $p\bar{p} \rightarrow t\bar{t} \rightarrow H^+H^-b\bar{b}$, $H^\pm \rightarrow \tau\nu$ events (m_{H^+}=50 GeV, m_t=70 GeV) 90

3-17 The electromagnetic energy fraction vs energy/momentum for taus and electrons in an ideal experiment. 92

3-18 The electromagnetic energy fraction vs energy/momentum for taus and electrons in an real experiment from a toy Monte Carlo. 93

3-19 The electromagnetic energy fraction vs energy/momentum for a) taus in simulated (ISAJET) $p\bar{p} \rightarrow t\bar{t} \rightarrow H^+H^-b\bar{b}$, $H^\pm \rightarrow \tau\nu$ events (m_{H^+}=50 GeV, m_t=70 GeV) which have passed the tau cluster and track requirements. b) Unbiased electrons from $Z \rightarrow ee$ events. The cut used to separate taus and electrons EM/E < 1-1/(7E/P) is shown. 94

3-20 Number of tracks in 7.5° cone with $P_T > 1.0$ GeV (N_{track}) a) taus in simulated (ISAJET) $p\bar{p} \rightarrow t\bar{t} \rightarrow H^+H^-b\bar{b}$, $H^\pm \rightarrow \tau\nu$ events (m_{H^+}=50 GeV, m_t=70 GeV) . b) Jets in a jet data set. The E_T and η distributions of the jets are the same as the tau sample. The taus and jets are required to pass all tau algorithm cuts. 96

3-21 The E_T and N_{track} for $W \rightarrow \tau\nu$ candidate events from the $\not{E}_T$ data set 98

3-22 The E_T and N_{track} for a sample of unbiased QCD jets, from a jet data set, which pass the hadronic tau algorithm requirements 98

3-23 N_{track} for $W \rightarrow \tau\nu$ candidate events from the $\not{E}_T$ data set, and for a normalized QCD jet background sample taken from unbiased jets in a jet data set 99

3-24 A candidate $W \rightarrow \tau\nu$ event. The central tracking chamber is shown. The event contains a three prong $W \rightarrow \tau\nu$ and large $\not{E}_T$ opposite the candidate cluster. 101

3-25 A candidate $W \rightarrow \tau\nu$ event. A lego plot of the calorimeter is shown. The distinct "monojet" topology is apparent. 102

3-26 The E_T and η of highest E_T cluster which is not a tau candidate, for simulated (ISAJET) $p\bar{p} \rightarrow t\bar{t} \rightarrow H^+H^-b\bar{b}$, $H^\pm \rightarrow \tau\nu$ events (m_{H^+}=50 GeV, m_t=70 GeV) 104

4-1 The leading order and some next-to-leading order diagrams for $t\bar{t}$ production.(a) Leading order quark fusion.(b) Leading order gluon fusion (c) Next-to-leading order real emission processes.(d) Next-to-leading order loop diagrams 111

4-2 The $t\bar{t}$ production cross section as a function of m_t at 1.8 TeV to order $\alpha_S(\mu_R)^3$. 112

4-3 The dependence of the $t\bar{t}$ production cross section at 1.8 TeV with $m_t = 60$ GeV on the renormalization and factorization scale μ. 113

4-4 The percentage of the $t\bar{t}$ cross section at 1.8 TeV which fragments before the top decays as a function of m_t Solid line: Hadronization scale $\Lambda^{-1} = 1$ fm. Dotted line: $\Lambda^{-1} = 0.5$ fm. Dashed line: $\Lambda^{-1} = 1$ fm. 117

4-5 The Peterson fragmentation fraction $D(z)^h$ for c,b,t quarks . . . 118

4-6 Schematic of the total $t\bar{t}$ branching ratio in the case $Br(t \to H^+b) = Y$. The areas represent the fraction of the total $t\bar{t}$ branching ratio for H^+H^-, H^+W^-, H^-W^+, W^+W^- 123

5-1 The number of tracks with $P_T > 1.0$ GeV in 7.5^o cone. The distributions for the $\tau + \not{E}_T + \geq 1$ jet data sample and the normalized QCD background sample are shown. 130

5-2 The transverse mass of e + jets in a) $\not{E}_T$data events and b) simulated (VECBOS) $W \to e\nu$ + jets events 133

6-1 The excluded regions for $Br(t \to H^+b) = 1.0$, $Br(H^+ \to \tau\nu_\tau)$ =0.5, 0.75, 1.0 in the (m_{H^+}, m_t) plane at 95 % Confidence Limit from CDF data 136

6-2 The excluded regions for model I in terms of $\tan\beta$ for the (m_{H^+}, m_t) plane of the two Higgs doublet model at 90 % confidence limit . 137

6-3 The excluded regions for model II in terms of $\tan\beta$ for the (m_{H^+}, m_t) plane of the two Higgs doublet model at 95 % confidence limit 138

6-4 The excluded regions of the (m_t, m_{H^+}) plane in Model IV for $\tan\beta = 1.2$, 1.65, 2.5 and $\tan\beta > 5.0$ at 95 % confidence limit. The sensitivity is a maximum for $\tan\beta$ =2.5 and then decreases to a constant value for $\tan\beta > 5.0$ 139

Acknowledgments

I thank the entire CDF collaboration and the Fermilab staff whose dedicated efforts have made the CDF experiment possible. I was fortunate to have Professor Melissa Franklin as my advisor. She was always available for help and guidance, yet provided me with the freedom necessary to develop my own ideas. Dr. George Brandenburg has helped me in innumerable ways, both as Director of the High Energy Physics Laboratory and as a colleague.

The motivation for this thesis is the interesting possibility that the long sought after top quark may have eluded discovery because we were looking for it in the wrong way. This idea was first introduced to me over refreshments at the SLAC summer institute by Dr. Keith Ellis and I thank him for this and for explaining many theoretical issues in top quark production and decay. Proton antiproton decays are sufficiently complicated to make a search for these alternative decays of the top quark rather challenging and it would have been impossible without the body of knowledge built up by the work of the various analysis groups on CDF. This thesis used many analysis tools developed by these groups and it is impossible to thank each individual involved, however the work of Dr. Aaron Roodman was an essential starting point. The top quark and exotic physics groups provided a challenging forum for the discussion of this work and I thank the members of these groups for their criticisms. In the early stages of this thesis Dr. Jacobo Konigsberg helped focus many of the ideas and throughout the development of the analysis he has provided valuable criticism. Tom Baumann and I overlapped on a number of analysis issues and I benefitted from our discussions. I also thank Dr. Barry Wicklund for his advice and criticism that helped me write a PRL article on this work in a timely fashion.

The first few years of my graduate career were spent working with the UA1 group at Harvard. Unfortunately the complete evaporation of this group in 1989 prevented me from doing my thesis work on this experiment but nonethe-

less I learnt a great deal about particle physics during this period and it was an interesting introduction to the field. I thank Professor Carlo Rubbia for giving me this opportunity and Professor James Rohlf, Dr. Sham Sumorok, Dr. Gerry Bauer, Alan Schwartz and Steve Pavlon for help. In later years I benefited from the help and advice of Professor Gary Feldman and I thank him for both keeping the CDF group at Harvard stable during a difficult period and helping me get to the next step in my career. I also benefitted greatly from many informal conversations with Professors John Huth, Marjorie Shapiro, Sanjib Mishra, Kay Kinoshita and Hitoshi Yamamoto, which helped me with my own work and also in understanding different areas of particle physics.

The time I spent at Fermilab was pleasurable and rewarding. This was due to the many friends and colleagues who both helped me and provided good company when work was over. I was able to learn many of the intricacies of exactly how the CDF experiment worked, and more generally how a particle physics experiment works, at the 1990-91 CDF testbeam, rather than in the main collider experiment. This was partially because the smaller scale allowed me a more diverse involvement but mostly due to considerable help and advice that I received. In particular, I thank Dr. Steve Hahn for teaching me how the data acquisition system worked and Bob Mattingly for the many good times we spent working on every aspect of the testbeam together. Tom Baumann, Lou Keeble, Peter Maas , Steve Moulding and Professor Lee Pondrom were among the many people who also provided valuable help. Life on the prairie could sometimes be somewhat desolate but fortunately my time at Fermilab was eased by a host of friends. I thank Steve Vejcik, Chris & Amy Boswell, Dan Broemmelseik, Mark Lundin, Mani, Brij, Les Nakae, Judy and others at the users center, the CDF party crowd (particularly Dee Hahn for her administrative work), the CDF hoopsters and all the aforementioned advisors and colleagues.

The laboratory at Harvard has always been a convivial and pleasant place to work due to the excellent staff. I thank Mary Platt and Tony Pacheco for help

with all secreterial matters and much else. Dr. John Oliver, Jack O'kane and Sarah Harder for help with electronics. Jim McIllaney Frank Dalyrimple, Ed Lucia, Steve Sansoni, Ed Sadowski for mechanical help and particularly Rick Haggerty for showing me how to fix everything from a fridge to a '74 Chevy V8. My fellow graduate students at Harvard have both helped and provided necessary distractions. I thank Tom Dignan, Fotis Ptohos, Tom Baumann, Dave Brown, Rob Carey, Ed Kearns, Peter Hurst, Rowan Hamilton and Johnny Ng. Special thanks to Andy Feldman for a constant and enduring friendship that frequently helped me through the bad times. Also to Adrian Cooper, who was a perfect host during my escapes to sunny California.

Finally and most importantly I thank my parents for constant support and encouragement. They gave me the opportunities that they never had and it is impossible for me to fully express my gratitude.

I dedicate this thesis to my parents and to my sister, Dr. Melanie Jessop M.D.

Chapter 1

Introduction and Theory

This thesis describes an experiment to search for the decay $t \rightarrow H^+b \rightarrow \tau\nu b$ in $p\bar{p}$ collisions at $\sqrt{s}$=1.8 TeV. The experiment was performed on 4.1 pb^{-1} of data collected by the CDF detector during the 1988-89 run at the Fermilab Tevatron.

The top quark has so far eluded discovery. The conventional explanation for this is that it has very high mass. The production cross-section is therefore small, and the current limit is $m_t > 108$ GeV [1]. However, this limit assumes that the top decays within the minimal standard model to a weak charged vector boson and a bottom quark, $t \rightarrow W^+b$. The minimal standard model assumes a single neutral scalar Higgs boson. If the standard model is not minimal or new physics exists beyond the standard model, such as supersymmetry or technicolor, then the Higgs sector becomes more complicated and a charged scalar Higgs pair ($H^\pm$) is introduced in addition to the neutral scalars. For certain (m_t, m_{H^+}) combinations it is then possible that the top will decay almost exclusively to H^+b rather than W^+b [1]. Since the decay channels of the H^+ and W^+ are different it follows that the current top limits are invalid in this scenario. We will begin by motivating the belief that the top quark exists and

[1]Throughout this thesis we denote the charged Higgs by H^+ and the charged weak vector boson by W^+ but all statements should be understood to apply to the charge conjugate particles H^-, W^- and processes in which they are involved.

then describe the role of the Higgs sector and the constraints on its structure. This will lead naturally to the possibility of a more complicated Higgs structure with charged Higgs bosons. We will then describe the exact conditions under which the decay $t \rightarrow H^+b$ is dominant over $t \rightarrow W^+b$.

1.1 Evidence for the existence of the top quark

The SU(2) structure of the standard model has been consistently successful in the study of weak interactions. The left handed components of quarks and leptons are weak isospin doublets. The right handed components are singlets. If the third quark family fits into this structure then the left handed b quark is the lower component of an SU(2) isodoublet. This demands the existence of the top quark as the upper component. The right handed b and t quarks are isosinglets.

If the b quark is not part of an SU(2) doublet then it cannot decay by emission of a $W^{\pm}$. The only possible mechanism for its decay is then by some form of quark mixing which induces flavor changing neutral currents (FCNC). These give rise to large branching ratios of B decays to charged lepton pairs: $B(B \rightarrow l^+l^-X)/B(B \rightarrow l\nu_l) > 0.12$ [2]. The Feynman diagrams for these two processes are shown in figure 1-1. One can see that the ratio is independent of the mixing mechanism since the coupling constants of the FCNC would cancel. This prediction is three orders of magnitude greater than the most recent experimental bound from UA1: $B(B \rightarrow l^+l^-X)/B(B \rightarrow l\nu_l) < 5.0 \times 10^{-5}$ [3]. Additionally, if the b quark is not part of an SU(2) isodoublet the theoretically calculated partial decay width of the Z to b quarks is an order of magnitude less than the experimentally observed value [4].

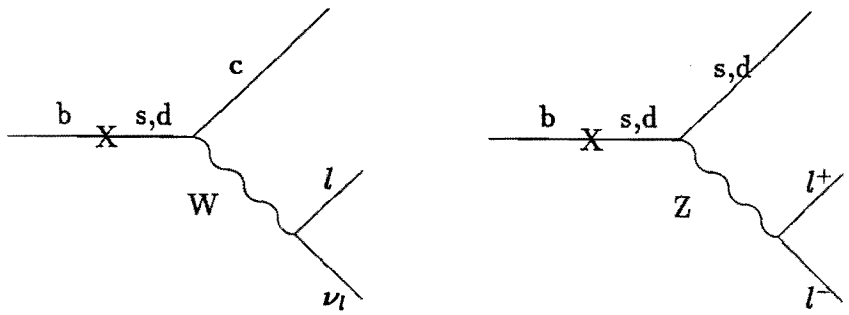

Figure 1-1: The Feynman diagrams for the processes $B(B \to l^+l^-X)$, $B(B \to l\nu_l)$, which involve flavor changing neutral currents.

We have shown that the b quark fits into the SU(2) structure of the standard model. We next ask whether it is the up or down component of the SU(2) doublet and whether it is the left or right handed components of the b that are part of the SU(2) doublet. The recent experimental results from electron-positron colliders allow us to determine the half-integer isospin assignments for the left and right handed b quark. At $\sqrt{s} = M_Z$ there are two measurements that are rather sensitive to these isospin assignments in the $e^+e^- \to b\bar{b}$ system, the forward-backward asymmetry, Λ_{FB}, and the width of the Z decaying to $b\bar{b}$, $\Gamma(Z \to b\bar{b})$.

$$\Gamma(Z \to b\bar{b}) = \frac{3G_F M_Z^3}{2\sqrt{2}\pi}(v_b^2 + a_b^2) \qquad \Lambda_{FB} = \frac{3}{4}\frac{2v_e a_e}{v_e^2 + a_e^2}\frac{2v_b a_b}{v_b^2 + a_b^2}$$

The v_b, a_b are given in terms of the left and right isospin components (I_3^L, I_3^R), the electric charge (e), and the weak mixing angle $(\sin^2\theta_W)$.

$$v_b = (I_3^L + I_3^R) - 2e_b \sin^2\theta_W \qquad a_b = (I_3^L - I_3^R) - 2e_b$$

The measurement of $\Gamma(Z \to b\bar{b})$) defines a circle in the (I_3^L, I_3^R) plane with radius R [5].

$$R^2 = \frac{\pi\sqrt{2}\Gamma(Z \to b\bar{b})}{G_F M_Z^3} = (I_3^L + \frac{1}{3}\sin^2\theta_w)^2 (I_3^R + \frac{1}{3}\sin^2\theta_w)^2$$

The measurement of Λ_{FB} defines a straight line in the (I_3^L, I_3^R) plane

$$|I_3^R + \frac{1}{3}\sin^2\theta_w| = \gamma|I_3^R + \frac{1}{3}\sin^2\theta_w|$$

with the slope γ given by

$$\gamma^2 = \left[1 - \frac{4\Lambda_{FB}}{3}\frac{v_e^2 + a_e^2}{2v_e a_e}\right] / \left[1 + \frac{4\Lambda_{FB}}{3}\frac{v_e^2 + a_e^2}{2v_e a_e}\right]$$

The observed values of the variables in the above equations are listed in table 1-1. Using these, we can plot the range of allowed values in the (I_3^L, I_3^R) plane (figure 1-2).

Observable	Reference	Result
Λ_{FB} at $\sqrt{s} = M_Z$ GeV	[6]	0.126 ± 0.022
Λ_{FB} at $\sqrt{s} = 35$ GeV	[7]	-0.228 ± 0.053
$\Gamma(Z \to b\bar{b})$ (MeV)	[8]	361 ± 19
M_Z(GeV)	[6]	91.175 ± 0.021
a_e^2	[6]	0.2492 ± 0.0012
v_e^2	[6]	0.0012 ± 0.0003
$\sin^2\theta_W$	[8]	0.2327 ± 0.007

Table 1.1: Averages of Z decay data observables with references

The circle becomes an annulus, due to the experimental error, and allows two possible half integer assignments (I_3^L, I_3^R) = (0.0,-0.5) or (-0.5,0.0). The region between the two straight lines, from Λ_{FB}, discriminates between the two possibilities and allows only (I_3^L, I_3^R) = (-0.5,0.0). This inference is further corroborated by data on Λ_{FB} at $\sqrt{s} = 35$ GeV. The forward-backward asymmetry at the Z resonance is due to the coherent superposition of the vectorial and axial Z currents. At the lower energy of $\sqrt{s} = 35$ GeV the asymmetry derives from the interference between the vectorial γ and axial Z exchange. This lower energy is accessible at PETRA/PEP. The forward backward asymmetry is given by

$$\Lambda_{FB} = \frac{3}{4}\frac{-2e_e e_b a_e a_b \mathrm{Re}\chi + 4v_e v_b a_e a_b |\chi|^2}{e_e^2 e_b^2 - 2e_e e_b v_e V_b \mathrm{Re}\chi + (v_e^2 + a_e^2)(v_b^2 + a_b^2|\chi|^2}$$

$$\chi = -\frac{1}{4\sin^2\theta_W\cos^2\theta_W}\frac{s}{s - M_Z^2 + iM_Z\Gamma_Z}$$

The above expression for Λ_{FB} defines a conic section in the (I_3^L, I_3^R) plane, but at $\sqrt{s} = 35$ GeV is reduced to a straight line.

$$I_3^R = I_3^L + \frac{\Lambda_{FB}}{9\mathrm{Re}\chi}$$

The excluded region is then defined by two parallel straight lines as shown in figure 1-2.

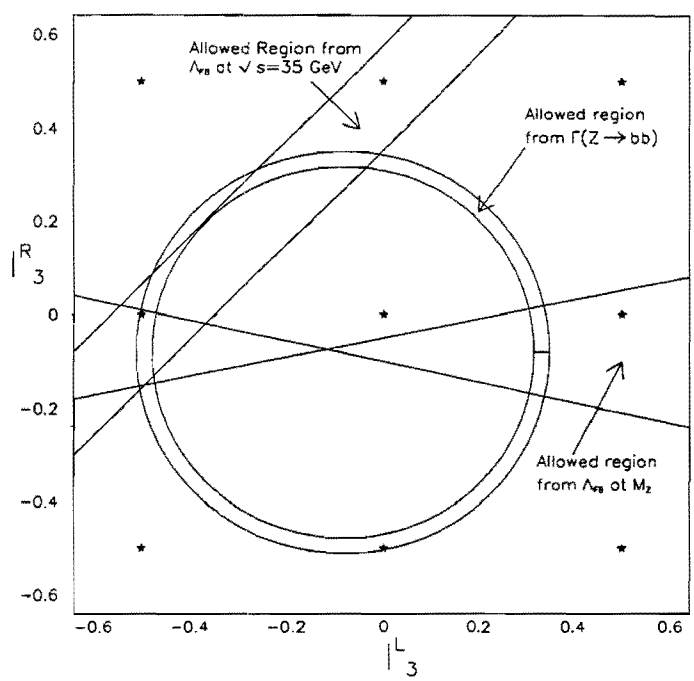

Figure 1-2: Allowed regions of the (I_3^L, I_3^R) plane, inferred from Z decay data. The circular region allows two possible half integer assignments, (I_3^L, I_3^R)=(0,-0.5) or (-0.5,0). The allowed region between the intersecting straight lines discriminates between the two possibilities and allows only (I_3^L, I_3^R)=(-0.5,0.0) . This is further corroborated by a measurement of Λ_{FB} at $\sqrt{s} = 35$ GeV which allows the region between the parallel lines.

The experimental evidence strongly indicates that the b quark is the lower component of an SU(2) doublet and implies the existence of the top quark as the upper component.

1.2 The Higgs boson

[2] In order to describe what the Higgs particle is, and what it does, it is appropriate to use the language of quantum field theory. We will briefly describe gauge symmetry and the central role it plays in current theories. This will lead naturally to an explanation of the Higgs Boson. The Lagrangian for a free Dirac particle (e.g. an electron) is

$$\pounds = i\bar{\psi}\gamma_\mu\partial^\mu\psi - m\bar{\psi}\psi$$

where ψ is a function of space and time (x). If the fields are shifted by a global phase transformation.

$$\psi \rightarrow \psi = e^{-iq\theta}\psi$$

the form of the Lagrangian is unchanged and therefore the physical processes it describes are unchanged. This invariance implies a conserved quantity (Noethers Theorem). In this case it is the electromagnetic charge, q. If we now consider a local phase transformation (i.e θ is a function of x) the Lagrangian is no longer invariant. The invariance can be restored by introducing a vector field A^μ which transforms as

$$A^\mu \rightarrow A^\mu + \partial^\mu\theta$$

This introduction necessitates the addition of an interaction term to the Lagrangian

$$-q\bar{\psi}\gamma_\mu\psi A^\mu$$

[2]This treatment paraphrases several standard texts [9]

The vector field is associated with the photon and we add the appropriate free field kinetic term to get the full Lagrangian.

$$\pounds = -\frac{1}{4}F_{\mu\nu}F^{\mu\nu} + i\bar{\psi}\gamma_\mu\partial^\mu\psi - m\bar{\psi}\psi + -q\bar{\psi}\gamma_\mu\psi A^\mu$$

This is the Lagrangian for electrons interacting with photons (QED). The local phase transformation is known as a gauge transformation and requiring its invariance in order to generate the interaction is known as the gauge principle. The significance of the gauge symmetry is that theories exhibiting this type of symmetry are renormalizable. The local gauge invariance can also be introduced by replacing the derivative in the free field Lagrangian with the covariant derivative.

$$\partial^\mu \longrightarrow D^\mu = \partial^\mu + iqA^\mu$$

Note that if the photon were massive then we would have to add a term

$$-\frac{1}{2}m^2 A_\mu A^\mu$$

which would break the gauge invariance.

The gauge principle applied with the appropriate gauge transformation on the SU(3) colour symmetry of quarks generates the QCD Lagrangian which is the theory of strong interactions. In this case the 8 massless bosons are gluons and again the gauge principle is able to generate the correct form of the interaction (couplings and the coupling strength).

If we now try to apply the gauge principle to the weak $SU(2)_L$ isospin symmetry we will generate 3 massless vector bosons $(A^{\mu+}, A^{\mu 0}, A^{\mu-})$. If we try to associate the $A^\pm$ with the weak charged bosons $W^\pm$ and the A^0 with the weak neutral boson Z there are two problems. First, the interactions generated are all pure V-A whereas the neutral currents are not pure V-A. Second the $W^\pm$,Z are massive. The correct interactions can be generated by expanding the symmetry group to $SU(2)_L \otimes U(1)$ where the $SU(2)_L$ is associated with weak isospin and the U(1) with weak hypercharge. The gauge principle applied to this symmetry group generates two charged massless vector bosons which are

associated with the $W^{\pm}$, and two neutral massless vector bosons which are associated with the Z and the photon. The couplings are now determined in terms of q and the weak mixing angle $\sin^2\theta_W$ which are parameters of the theory. The electromagnetic and weak interactions are unified in this model. However, the bosons generated are still massless. This problem can be solved by the mechanism of spontaneous symmetry breaking.

To illustrate the mechanism of spontaneous symmetry breaking we will consider a way of introducing mass to the photon in QED. The same mechanism can be used to generate mass for the vector bosons of the SU(2) $\otimes$ U(1) weak interaction theory above, but the U(1) case of QED is simpler and the underlying physical idea more transparent. We begin by writing down the equations of motion of QED which can be derived from the QED Lagrangian by Hamiltons principle.

$$\Box A^{\nu} - \partial^{\nu}\partial_{\mu}A^{\mu} = j^{\nu} \tag{1.1}$$

These are, of course, Maxwell's equations in covariant form and j^{ν} is the electromagnetic current. They are invariant under the gauge transformation $A^{\mu} \rightarrow A^{\mu} + \partial^{\mu}\theta$, and thus A^{μ} is the massless vector field of the photon. If we now arrange for the current to be of the form $j^{\nu} = -m^2A^{\nu}$, the gauge invariance is broken and equation 1.1 becomes

$$(\Box + m^2)A^{\nu} - \partial^{\nu}\partial_{\mu}A^{\mu} = 0$$

This is the equation for a free massive vector particle. This situation arises commonly in solid state physics. For example, if an electromagnetic field is applied to a superconductor, there are currents generated which themselves generate an electromagnetic field which opposes the original applied field, i.e $j^{\nu} = -m^2A^{\nu}$. This results in the screening out of the applied field. The A field thus has a finite range which is equivalent to having a mass, but the gauge invariance has also been broken. In the particle physics case we are considering we will now postulate the existence of a complex scalar field everywhere in space (i.e the physical vacuum) which will be analogous to the superconductor. The

scalar field, which has the same U(1) symmetry as QED is then postulated to interact with the A field so as to screen it out and provide a mass. In doing so however we must break the U(1) symmetry by a particular choice of phase of the scalar field. The subtlety is that the U(1) symmetry is not lost but rather hidden by a particular choice of phase (i.e gauge), and so the theory remains renormalizable.

We introduce the complex scalar field $\phi = \frac{h}{\sqrt{2}}e^{i\theta(x)} = \phi_1 + i\phi_2$. This field is globally U(1) invariant and the current term j^ν of equation 1.1 is the the probability current expression from standard quantum mechanics.

$$j^\nu = i((\phi^*(\partial^\mu\phi) - (\partial^\mu\phi^*)\phi) \tag{1.2}$$

To introduce the interaction of the ϕ field with the A field we use the gauge principle and make ϕ locally U(1) gauge invariant by introducing the covariant derivative $\partial^\mu \rightarrow \partial^\mu + iqA^\mu$ so that

$$j^\nu = -q^2h^2\left(A^\nu + \frac{\partial^\nu\theta}{q}\right)$$

Substituting this into equation 1.1

$$\Box A^\nu - \partial^\nu\partial_\mu A^\mu = -q^2h^2\left(A^\nu + \frac{\partial^\nu\theta}{q}\right) \tag{1.3}$$

This equation in invariant under the gauge transformations, $A^\mu \rightarrow A^\mu + \partial^\mu\theta$ and $\phi(x) \rightarrow \phi\exp^{-iq\phi(x)}$. If we now set the phase θ of the complex field to zero or equivalently choose the gauge $A^{\nu'} = A^\nu + \frac{\partial^\nu\theta}{q}$, and in both cases associate h with the constant vacuum expectation value of the Higgs field $f = h =< 0|\phi|0 >$, then equation 1.3 becomes

$$\Box A^\nu - \partial^\nu\partial_\mu A^\mu = -q^2f^2A^\nu \tag{1.4}$$

This is the equation of a free vector particle of mass m=qf. Equation 1.3 is locally gauge invariant but equation 1.4 is not. The fixing of the phase of the ϕ field has broken the symmetry and generated the mass of the vector field. Alternatively we can look at the degrees of freedom of equations 1.3 and 1.4.

Equation 1.3 has four degrees of freedom. A massless vector field has two degrees of freedom (i.e the two polarization vectors of a massless photon) , and there are two more from the complex ϕ field. Equation 1.4 also has four degrees of freedom, three from the massive vector field and one from the ϕ field. A degree of freedom has been lost from the ϕ field to give the A field mass. The U(1) local gauge symmetry is not lost but hidden by the choice of a particular gauge which is equivalent to fixing the phase of the ϕ field.

The ϕ field is an example of a Higgs field. The field has the local gauge symmetry of the massless vector Lagrangian to which it is introduced. It corresponds to the ground state of the Higgs potential $V(\phi)$ which is shown in figure 1-3

$$V(\phi) = -\frac{1}{2}\mu^2|\phi|^2 + \frac{\mu^2}{2f^2}|\phi|^4 \tag{1.5}$$

This ground state is postulated to be the physical vacuum, with constant vacuum expectation value f, so that vector bosons propagating through this vacuum generate "vacuum screening currents" which in turn give the bosons mass. This potential is displayed in figure 1-3. The local U(1) gauge invariance corresponds to rotations around the minima. This rotation is one of the degrees of freedom, while radial perturbations correspond to the other mode. Physically, the rotational freedom corresponds to massless Goldstone bosons. The radial perturbations are massive Higgs bosons since there is a change of energy. The mass of the Higgs bosons can be deduced. The minima of $V(\phi)$ is $\phi = \frac{f}{\sqrt{2}}e^{i\theta()}$ and radial perturbations can be considered by substituting $\phi = \frac{1}{\sqrt{2}}(f + \rho(x))$ into the expression for $V(\phi)$.

$$V(\phi) = -\frac{\mu^2}{4}(f+\rho)^2 + \frac{\mu^2}{4f^2}(f+\rho)^4$$

and evaluating the ρ^2 coefficient implies that the $m_{H^+} = \mu$. The Higgs mechanism thus generates a massive vector boson with the mass expressed in terms of the coupling constant and the vacuum expectation value $m = qf$, and a scalar boson with undetermined mass μ. The interactions of the Higgs field and the vector boson field are also specified in terms of q and f.

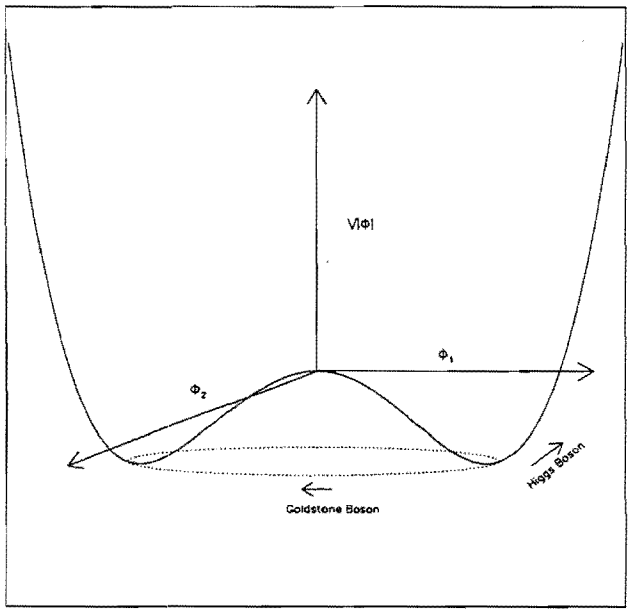

Figure 1-3: The Higgs potential. The minima is the physical vacuum. Rotational perturbations around the minima correspond to massless Goldstone bosons. Radial perturbations about the minima correspond to massive Higgs bosons.

We will now apply the mechanism of spontaneous symmetry breaking, which was explained above for a U(1) symmetry, to the $SU(2)_L \otimes U(1)$ symmetry of weak interactions. The mechanism is exactly the same except that the appropriate Higgs field is more complicated because of the expanded symmetry. The massless $SU(2)_L \otimes U(1)$ Lagrangian is

$$\pounds = -\frac{1}{4}W^{\mu\nu}W_{\mu\nu} - \frac{1}{4}B^{\mu\nu}B_{\mu\nu} + \bar{\psi}i\gamma_\mu D^\mu\psi$$

where D^μ is the covariant derivative introduced by the requirement of gauge invariance

$$D^\mu = \partial^\mu + igW^\mu.T + \frac{i}{2}g^{'}B^\mu Y \tag{1.6}$$

where T,Y are the generators for the $SU(2)_L$ and U(1) groups and g,g$'$ are the coupling constants of the $W = (W^+, W^\circ, W^-)$ and B fields respectively. The charged W fields $W^\pm$ are the charged weak bosons and the W° and B fields are linear combinations of the weak neutral boson field Z and the photon A related by

$$\begin{pmatrix} W^\circ \\ B \end{pmatrix} = \begin{pmatrix} \cos\theta_W & \sin\theta_W \\ -\sin\theta_W & \cos\theta_W \end{pmatrix} \begin{pmatrix} Z \\ A \end{pmatrix}$$

The electric charge, hypercharge and weak isospin are related by

$$q = T_3 + \frac{1}{2}Y$$

The coupling constants are given by

$$g_{w^\pm} = \frac{q}{\sin\theta_W} \qquad g_Z = \frac{q}{\sin\theta_W \cos\theta_W}$$

In order to introduce mass to the W,Z fields while keeping the A field massless we need to break the symmetry $SU(2)_L \otimes U(1)$ to the U(1) symmetry associated with the massless photon. The simplest way of doing this is to introduce a Higgs field with four degrees of freedom. That is, we introduce a complex scalar $SU(2)_L$ doublet with Y=1.

$$\begin{pmatrix} \phi_1^+ + i\phi_2^+ \\ \phi_1^0 + i\phi_2^0 \end{pmatrix} = e^{(\frac{i}{2}\vec{\tau}.\vec{\alpha})} \begin{pmatrix} 0 \\ \frac{1}{\sqrt{2}}(f + \rho(x)) \end{pmatrix}$$

The $\vec{\tau} = (\sigma_1, \sigma_2, \sigma_3)$ are the three Pauli matrices that are part of a global SU(2) rotation and $\vec{\alpha} = (\alpha_1, \alpha_2, \alpha_3)$ are three physical massless fields (Goldstone Bosons) . ρ is the massive field (Higgs Boson) associated with perturbations about the minima of the Higgs potential given by equation 1.5. The three boson masses can be generated by fixing the values of the three fields to zero thereby breaking the symmetry. The masses can be derived by using the covariant derivative in equation 1.6 on the free field Lagrangian. Alternatively we can derive the vacuum screening currents that generate these masses by using the covariant derivative on the expressions for probability current in

equation 1.2. In addition this prescription will give the prescribed form for the interactions. This then implies

$$M_W = \frac{gf}{2} \qquad M_Z = \frac{M_{W+}}{\cos\theta_W} \qquad g = \frac{q}{\sin\theta_W} \tag{1.7}$$

To test these relationships we form the quantity ρ which is the ratio of the neutral to charged current strength.

$$\rho = \frac{\left(\frac{g_Z^2}{M_Z^2}\right)}{\left(\frac{g_{W+}^2}{M_{W+}^2}\right)}$$

If we define $\sin^2\theta_W$ appropriately

$$\sin^2\theta_W = 1 - \frac{M_{W+}^2}{M_Z^2}$$

then $\rho = 1$. We may then combine the constraint $\rho = 1.0$ with a measurement of the three three parameters M_Z, g_{W+}, g_Z to predict M_{W+} and compare it to the measured M_{W+}. Rather than use M_Z, g_{W+}, g_Z we actually measure three other parameters G_F, α, M_Z which are directly related to M_Z, g_{W+}, g_Z but are more accurately measured.

1. The Fermi coupling constant can be measured in low energy muon experiments ($s^2 \ll M_{W+}$)

$$G_F = \frac{\sqrt{2}g^2}{8M_{W+}^2} = 1.16639 \pm 0.00002 \text{ GeV}^{-2}$$

2. The mass of the Z boson has been accurately measured at LEP

$$M_Z = 91.173 \pm 0.020 \text{ GeV}$$

3. The fine structure constant

$$\alpha(s^2 = 0) = \frac{q^2}{4\pi} = \frac{1}{137.0359895 \pm 0.0000081}$$

These are then combined to predict the W^+ mass [10]

$$m_{W+} = 80.2 \pm 0.3 \text{ GeV (predicted)}$$

This can then be compared with the direct measurement of the W^+ mass by the CDF collaboration [11]

$$m_{W^+} = 79.91 \pm 0.39 \text{ GeV (measured)}$$

This precise test gives strong support to the standard model and the mechanism of spontaneous symmetry breaking for generating the gauge boson masses. Additionally it confirms that $\rho = 1$, which will be used as a powerful constraint in building models beyond the minimal standard model. However, there remains a problem with the fermion mass terms. A mass term for fermions of the form

$$m\psi\bar{\psi} = m(\psi_L\bar{\psi}_L + \psi_R\bar{\psi}_R)$$

is not $SU(2)_L \otimes U(1)$ covariant since it contains both a left and right handed component. In this case the theory is non-renormalizable. A prescription for making the mass terms $SU(2)_L \otimes U(1)$ covariant is to introduce Yukawa couplings of the fermions to the Higgs fields of the form

$$g_f(\bar{\psi}_L\phi\psi_R + \bar{\psi}_R\phi\psi_L)$$

When the symmetry is broken by the phase choice

$$\phi = \begin{pmatrix} 0 \\ \frac{f}{\sqrt{2}} \end{pmatrix}$$

the above expression becomes

$$\frac{g_f f}{\sqrt{2}}(\bar{\psi}_L\psi_R + \bar{\psi}_R\psi_L)$$

so the fermion mass $M_f = \frac{g_f f}{\sqrt{2}}$. Also couplings to the Higgs fields are introduced with strength $\frac{m_f}{f}$.

The strength of this mechanism is that, using the same Higgs fields, it can generate the mass of both the bosons and fermion and keep the theory renormalizable. The weakness is that one has to introduce a new coupling for every fermion so that the mechanism provides no fundamental explanation of the mass of the fermions as it does in the case of the bosons.

1.3 Constraints on the Higgs bosons

The accurate predictions made for the gauge bosons which have been well tested at LEP and other experiments lead us to believe that some scalar field must cause symmetry breaking. However, there is no prediction of the mass of the field or of its structure. It is natural to use the simplest possible field, namely a complex doublet - i.e the minimal standard model. However it is completely possible within the standard model that a more complicated structure may exist. The constraints on the Higgs fields are

1. It must be a scalar field since a non-zero vacuum expectation value of a vector or Dirac field would not be Lorentz invariant.

2. It must be an SU(2) representation in order to fit into the SU(2) structure of the standard model.

3. It must have at least four degrees of freedom so that it can give mass to the bosons.

4. Only neutral components of the Higgs field should have non-zero vacuum expectation. Otherwise the electromagnetic U(1) gauge invariance is broken and the photon is no longer massless.

5. The field must not destroy the $\rho = 1$ constraint since we have shown this to be an experimental fact.

6. Experimentally no flavor changing neutral currents have ever been observed so the theory should not contain them.

The first four constraints lead to a general structure

$$N_1.SU(2)_2 + N_2.SU(2)_3 + N_3.SU(2)_4 ...$$

$N_1.SU(2)_2$ denotes N_1 SU(2) doublets. With this structure the formula for ρ is [12]

$$\rho = \frac{\sum_{T,Y}[4T(T+1) - Y^2]|V^2_{T,Y}|C_{T,Y}}{\sum_{T,Y} 2Y^2|V_{T,Y}|^2}$$

where $V_{T,Y}$ is the vacuum expectation of each neutral Higgs field ,$C_{T,Y}$ is 1,0.5 for complex and real fields respectively, and T,Y are the isospin and hypercharge assignments. The constraint that $\rho = 1$ for arbitrary $V_{T,Y}$ implies

$$(2T + 1)^2 - 3Y^2 = 1$$

Assuming that only one field gets a non-zero vacuum expectation value, and that T can be a half integer and Y an integer, the possibilities are

$$\begin{array}{lll} T = \frac{1}{2} & Y = \pm 1 & \text{doublets} \\ T = 3 & Y = \pm 4 & \text{sextuplets} \end{array}$$

A T=3 representation of SU(2) is a 7 component multiplet with charges as high as ± 5 ($Q = T_3 + \frac{1}{2}Y$). This is generally discounted as being too complicated. This constraint then leaves the possibility of several Higgs doublets.

In the minimal standard model with only one Higgs doublet, flavor changing neutral currents (FCNC) are naturally avoided. In models with more that one doublet, FCNC's are absent if all fermions of a given electric charge couple to no more than one doublet [13] . The simplest extension of the minimal standard model Higgs that can be made to satisfy this constraint is therefore a model with two Higgs doublets known appropriately as the "two Higgs doublet model"(THD). The remaining constraints on such a model are purely experimental searches for the Higgs bosons that result.

1.4 Naturalness and the Higgs Boson

We have just described how the constraints on the Higgs boson allow it to have a more complicated structure than the single neutral scalar of the minimal standard model, though do not compel it to do so . However, there are additional reasons why the structure may be more complicated due to the problems of naturalness. In the minimal standard model the one loop correction to the Higgs mass is quadratically divergent [14] with the consequence that the Higgs boson is not naturally light. This problem originally motivated theories such

as technicolor [15] and supersymmetry [16]. In supersymmetry the divergence is canceled by the one loop diagrams involving the supersymmetric partners of the particles contributing to the divergent loops, while technicolor solves this problem by making the Higgs bosons composite particles. In supersymmetry there must be at least two Higgs doublets in order to avoid anomalies which make the theory non-renormalizable [17]. Additionally, in order to avoid flavor changing neutral currents the two doublets must couple to the fermions in a particular way (described in section 1.5). Models with more than one doublet contain a charged Higgs and we now describe the simplest extension of the Higgs sector, the two Higgs doublet model. However we note that supersymmetry requires $m_{H^+} > m_{W^+}$, which as we will show in section 1.9, is beyond the experimental sensitivity of the experiment described in this thesis.

1.5 The two Higgs doublet model

This consists of two complex Higgs doublets

$$\phi = \begin{pmatrix} \phi_1^0 \\ \phi_1^- \end{pmatrix} \qquad \phi_2 = \begin{pmatrix} \phi_2^+ \\ \phi_2^0 \end{pmatrix}$$

The neutral members of the doublet acquire the vacuum expectation

$$\begin{pmatrix} f_1 \\ 0 \end{pmatrix} \qquad \begin{pmatrix} 0 \\ f_2 \end{pmatrix}$$

and the expression for M_W is the same as equation 1.7 but with

$$f = \sqrt{f_1^2 + f_2^2} = 246 \text{ GeV}$$

There are eight degrees of freedom in the Higgs field. Three are used to give mass to the W,Z bosons and so there are five massive Higgs bosons. There are two charged Higgs bosons $H^{\pm}$, a pseudoscalar A^0 and two scalars H^o,h^o. The masses are independent and unconstrained at the tree level [3] as is the parameter

$$\tan\beta = \frac{f_2}{f_1}$$

The physical charged Higgs fields are given by

$$H^{\pm} = \pm\frac{1}{\sqrt{f}}(f_2\phi_1^{\pm} - f_1\phi_2^{\pm})$$

and the Lagrangian for the interaction with fermions is of the form [19]

$$\mathcal{L} = (2\sqrt{2}G_F)^{\frac{1}{2}}H^+(V_{ij}m_{ui}A_u\bar{u_L}D_R + V_{ij}m_{di}A_d\bar{u_R}D_L + m_lA_l\bar{N_L}L_R))$$

where

V_{ij} = KM matrix

U = up type quarks (u,c,t)

[3] At the one loop level Toussaint [18] has shown that radiative corrections to the W,Z masses imply that the mass of the A should not be too dissimilar to the mass of the $H^{\pm}$.

D = down type quarks (d,s,b)

N = neutrinos (ν_e, ν_μ, ν_τ)

l = leptons (e, μ, τ)

The Kobayashi-Maskawa (KM) matrix is a matrix that gives the relative charged current couplings between the u,c,t and d,s,b quarks. The empirically determined values are

$$V_{ij} = \begin{pmatrix} V_{ud} & V_{us} & V_{ub} \\ V_{cd} & V_{cs} & V_{cb} \\ V_{td} & V_{ts} & V_{tb} \end{pmatrix}$$

$$= \begin{pmatrix} 0.9747 \pm 0.0011 & 0.221 \pm 0.002 & < 0.011 \\ 0.20 \pm 0.03 & 0.979 \pm 0.006 & 0.050 \pm 0.007 \\ < 0.17 & < 0.13 & 0.9987 \pm 0.0004 \end{pmatrix}$$

There are three couplings A_u, A_d, A_l which are determined by the arrangement of quark and lepton couplings to the Higgs doublets. As stated previously, the only constraint is to require that all fermions of a given electric charge couple to only one doublet. This leads to four general possibilities which give different assignments for A_u, A_d, A_l (table 1.5).

Model	Couplings	A_u	A_d	A_l
I	$\phi_2 \rightarrow$ u,c,t $\phi_2 \rightarrow$d,s,b $\phi_2 \rightarrow e, \mu, \tau$	$\cot\beta$	$-\cot\beta$	$-\cot\beta$
II	$\phi_2 \rightarrow$u,c,t $\phi_1 \rightarrow$d,s,b $\phi_1 \rightarrow e, \mu, \tau$	$\cot\beta$	$\tan\beta$	$\tan\beta$
III	$\phi_2 \rightarrow$u,c,t $\phi_1 \rightarrow$d,s,b $\phi_2 \rightarrow e, \mu, \tau$	$\cot\beta$	$\tan\beta$	$-\tan\beta$
IV	$\phi_2 \rightarrow$u,c,t $\phi_2 \rightarrow$d,s,b $\phi_1 \rightarrow e, \mu, \tau$	$\cot\beta$	$-\cot\beta$	$\tan\beta$

Table 1.2: The possible couplings of the Higgs doublets to fermions in the two Higgs doublet model.

The charged Higgs couples to the same fermion currents as the W, but with a coupling strength proportional to the mass of the fermions. Figure 1-4 shows the Feynman diagrams, and coupling constants, for both the charged Higgs and W^+ couplings to quarks. The coupling constant for the charged Higgs to the lepton currents is the same except that m_u is replaced by m_l, m_d is replaced by m_ν=0, and A_u is replaced by A_l.

$$\frac{ig}{2\sqrt{2}}(\gamma_\mu(1-\gamma^5)V_{ud} \qquad \frac{ig}{2\sqrt{2}m_{W^+}}[(m_dA_d + m_uA_u) - (m_dA_d - m_uA_u)\gamma_5]$$

Figure 1-4: A comparison of the charged Higgs and W^+ boson couplings for quarks. U denotes the "up" type quarks u,c,t and d denotes the "down" type quarks d,s,b. The couplings of the charged Higgs to the lepton currents is similar except that m_u is replaced by m_l, m_d is replaced by m_ν=0, and A_u is replaced by A_l.

The coupling of the charged Higgs to fermions is significant for processes involving very heavy fermions, in particular the top quark. Examples of this are $B - \bar{B}$ mixing, in which the top quark appears in the propagator of the box diagram in figure 1-5 , and in the decay of the top quark which is also illustrated in figure 1-5.

and then integrating over the available phase space of the final state. The matrix elements for the $t \to H^+b$ and $t \to W^+b$ decay are similar for heavy top quarks (i.e of the order of the W^+ mass) and so it is the phase space that is the determining factor. A two body final state will be a much faster decay than a three body final state because of the extra phase space factor. A two body final state will arise in the top decay if the H^+ or W^+ is real, i.e if $m_{H^+} + m_b < m_t$ or $m_{W^+} + m_b < m_t$, while a three body final state arises if the H^+ or W^+ is virtual, i.e if $m_{H^+} + m_b > m_t$ or $m_{W^+} + m_b > m_t$. In particular, if $m_{H^+} + m_b < m_t < m_{W^+} + m_b$, then the $t \to H^+b$ decay will be a two body decay and be much faster (i.e have a much larger width) than the three body $t \to W^+b$ decay. Consequently the $t \to H^+b$ decay will dominate. The expressions for the widths of the $t \to H^+b$, $t \to W^+b$ decays are given below. If $m_{H^+} + m_b < m_t$, the width of the top to real Higgs decay is [20]

$$\begin{aligned}\Gamma(t \to H^+b) &= \frac{G_F m_t^3}{8\pi\sqrt{2}}\left[\left(A_u^2 + \left(\frac{m_b}{m_t}\right)^2 A_d^2\right)\left(1 + \left(\frac{m_b}{m_t}\right)^2 - \left(\frac{m_b}{m_{H^+}}\right)^2\right) + 4\left(\frac{m_b}{m_t}\right)^2\right] \\ &\times \lambda\left(1, \left(\frac{m_b}{m_t}\right)^2, \left(\frac{m_{H^+}}{m_t}\right)^2\right)\end{aligned} \tag{1.8}$$

where

$$\lambda(a, b, c) = (a^2 + b^2 + c^2 - 2ab - 2bc - 2ca)$$

If $m_{W^+} + m_b < m_t$ the top decays to a real W^+ and the width is

$$\begin{aligned}\Gamma(t \to W^+b) &= \frac{G_F m_t^3}{8\pi\sqrt{2}}\left[\left(1 + \left(\frac{m_b}{m_t}\right)^2\right)^2 + \left(\frac{m_{W^+}}{m_t}\right)^2\left(1 + \left(\frac{m_b}{m_t}\right)^2\right) + 2\left(\frac{m_{W^+}}{m_t}\right)^4\right] \\ &\times \lambda\left(1, \left(\frac{m_b}{m_t}\right)^2, \left(\frac{m_{H^+}}{m_t}\right)^2\right)\end{aligned} \tag{1.9}$$

If $m_{W^+} + m_b > m_t$ the top decays to a virtual W^+ and the width

$$\Gamma(t \to b\tau\nu) = \frac{g^2 m_{W^+}^2}{48\pi^2}\int \frac{dm_X^2 \Gamma(t \to bX^+)}{(m_{X^+}^2 - m_{W^+}^2)^2 + (\Gamma m_{W^+})^2}$$

where X^+ denotes an off-shell W^+ and $\Gamma(t \to bX^+)$ is given by equation 1.9 with $m_{W^+} \to m_{X^+}$. Analogous formulas with color factors apply to $t \to bc\bar{s}$, and the total width is

$$\Gamma(t \to W^+b) = \Gamma(t \to bc\bar{s}) + \Gamma(t \to \tau\nu)$$

Using these formula one can show, for example, that W^+ decays are heavily suppressed Model II if

$$m_{H^+} + m_b < m_t < m_{W^+} + m_b \qquad \tan\beta > 1.0 - 2.0$$

As $m_{H^+} \rightarrow m_t$ the suppression is less since the phase space for $t \rightarrow H^+b$ is reduced. Also as $m_t \rightarrow m_{W^+}$ the suppression is decreased because the W^+ becomes "less" virtual. We will describe in more detail exactly which models and for which parameter value this suppression occurs after describing the experimental constraints on these parameters. At this point we will reiterate that it is possible that the assumption of previous top quark searches, $Br(t \rightarrow W^+b) = 1.0$, is invalid if a charged Higgs exists. Since the resultant final state signals are different the conventional top quark searches do not exclude certain areas of the $m_t, m_{H^+}, \tan\beta$ space.

1.7 Experimental limits on $m_t, m_{H^+}, \tan\beta$

Experimental constraints on the mass of the charged Higgs and $\tan\beta$ have come from a search for $Z \rightarrow H^+H^-$ at LEP and from low energy $e^+e^- \rightarrow b\bar{b}$ experiments at CLEO. Constraints on the top mass independent of the top decay mode have been reported by the $p\bar{p}$ experiments UA1,UA2,CDF. Also UA1 and UA2 have conducted direct searches for the top quark decaying to a charged Higgs and are able to exclude certain regions of $m_t, m_{H^+}, \tan\beta$ for model II.

1.7.1 LEP constraints

$$\Gamma(Z \rightarrow H^+H^-) = \frac{G_F^2 M_Z^3}{6\sqrt{2}\pi}\left(\frac{1}{2} - \sin^2\theta_W\right)\left(1 - \left(\frac{4m_{H^+}^2}{M_Z^2}\right)^{\frac{3}{2}}\right)$$

If the Higgs mass is m_{H^+}=35.0 GeV the branching ratio of Z to H^+H^- is 0.026. In the 200,000 Z decays recorded by each of the LEP collaborations, during the 1989-91 runs, one therefore expects $\sim$ 500 $Z \rightarrow H^+H^-$ events produced.

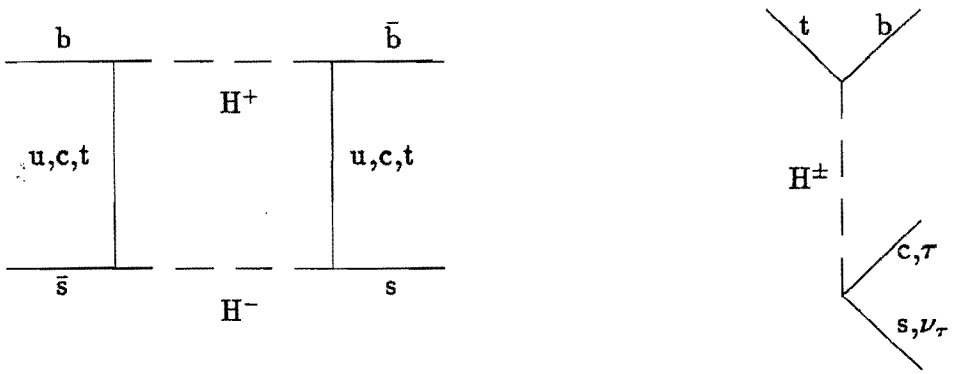

$B - \bar{B}$ mixing

Heavy quark decay

Figure 1-5: The Feynman diagrams for $B - \bar{B}$ mixing, and for top quark decay involving the charged Higgs. The dominant decay modes of the charged Higgs are $c\bar{s}, \tau\nu_\tau$.

In this thesis we will concentrate on the top quark decay mediated by a charged Higgs. Since the Higgs couples to mass it follows that it will decay to the heaviest kinematically available lepton ($H^+ \to \tau\nu_\tau$) or quark ($H^+ \to c\bar{s}$) current. The relative branching fraction ($H^+ \to c\bar{s} : H^+ \to \tau\nu_\tau$ is a function of $\tan\beta$ and therefore unconstrained. The branching ratio is given by [19]

$$\begin{aligned} Br(H^+ \to \tau\nu_\tau) &= \frac{\Gamma(H^+ \to \tau\nu_\tau)}{\Gamma(H^+ \to c\bar{s}) + \Gamma(H^+ \to \tau\nu_\tau)} \\ &= \frac{m_\tau^2 A_l^2}{3|V_{cs}|^2(m_c^2 A_u^2 + m_s^2 A_d^2) + m_\tau^2 A_l^2} \end{aligned}$$

where

$$Br(H^+ \to \tau\nu_\tau) + Br(H^+ \to c\bar{s}) = 1.0$$

The dependence of the branching ratio on $\tan\beta$ depends on the arrangement of Higgs-fermion couplings. Figure 1-6 shows this dependence for the four models.

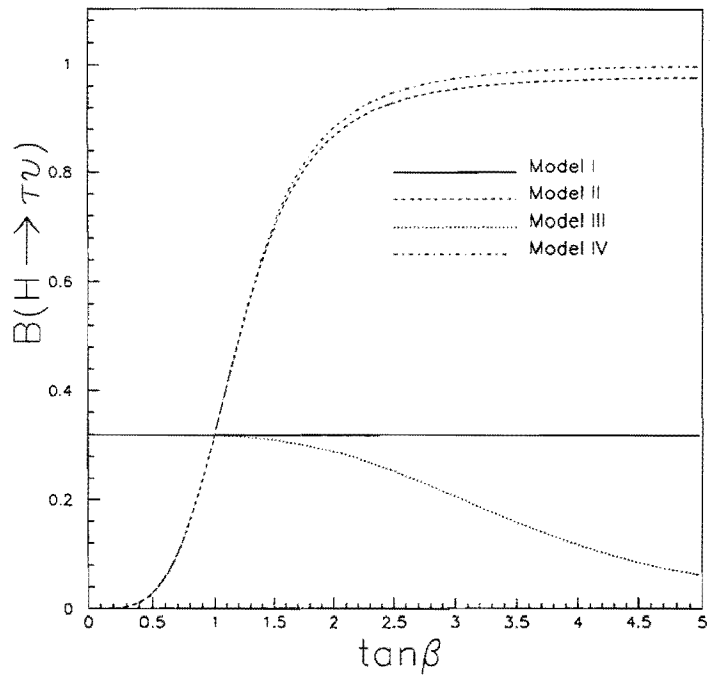

Figure 1-6: The branching ratio of $H^+ \to \tau\nu_\tau$ for the two Higgs doublet model

If the top quark decay is mediated by a charged Higgs then the final state will be either jets ($c\bar{s}$) or $\tau\nu_\tau$.

1.6 The top quark decaying to a charged Higgs

In the previous section we considered the coupling strength of the top to the charged Higgs and suggested that this decay maybe significant for large top masses because the charged Higgs couples to mass. We now need to compute the width of the $t \to H^+b$ decay and compare it to the width of the $t \to W^+b$ decay, for different m_{H^+}, m_t, since it is the relative widths that actually determine the cases for which the $t \to H^+b$ decay could dominate over the $t \to W^+b$ decay. The width is computed by calculating the matrix element

Using similar analysis techniques [21] the four LEP collaborations (ALEPH, DELPHI, L3 and OPAL) have searched for

$$Z \rightarrow H^+H^- \rightarrow \tau\nu\tau\nu, \tau\nu cs, cscs$$

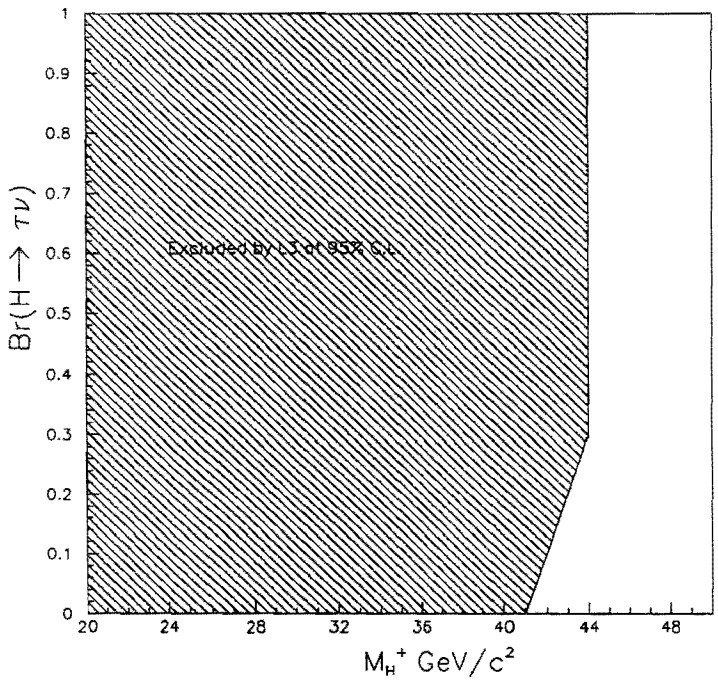

Figure 1-7: The excluded regions of the $m_{H^+}, Br(H^+ \rightarrow \tau\nu_\tau)$ plane from L3 data at 95 % confidence limit

No events were observed. Limits can then be set in the $m_{H^+}, Br(H^+ \rightarrow \tau\nu_\tau)$ plane (figure 1-7). The most recent results indicate that $m_{H^+} > 45$ GeV independent of the branching ratio and thus independent of which model is used.

1.7.2 Constraints from low energy data (mixing and CP violation)

$B_d^0 - \bar{B}_d^0$ mixing, $K - \bar{K}$ mixing and the CP violation parameter ϵ are all sensitive to the charged Higgs through the box diagrams in figure 1-5. However, we note that theoretical calculations for these processes are fraught with

uncertainty, and so the resultant constraints should be regarded skeptically. The experimental data from these phenomena have been analyzed in terms of the two Higgs doublet model by Barger,Hewett and Philips [19] to yield a set of constraints on $m_{H^+}, m_t, \tan\beta$. The most significant contribution is from $B_d^0 - \bar{B}_d^0$ mixing. The constraints are independent of the the model and exclude $\tan\beta < 0.2$ for $m_t > 60\text{GeV}$ and $m_{H^+} < 100\text{GeV}$.

The charged Higgs can give sizeable contributions to $B_d^0 - \bar{B}_d^0$ mixing and can account for the observed value of χ_d [22] without requiring the top quark to be heavy [23]. χ_d is the mixing parameter and is related to the $B_d^0 - \bar{B}_d^0$ mass difference ΔM and the B meson width Γ.

$$\chi_d = \Delta M/\Gamma$$

The contribution of the box diagrams containing the charged Higgs to ΔM_B is given by

$$\Delta M_B^H = \frac{G_F^2}{6\pi^2} m_{W^+}^2 m_B^2 f_B^2 B_B |V_{tb} V_{td}^*|^2 \eta . g\left(\cot\beta, \frac{m_{H^+}}{m_{W^+}}, \frac{m_t}{m_{W^+}}, \frac{m_b}{m_{W^+}}\right)$$

where

f_B is the B meson decay constant

B_B is the B meson bag factor

η is a QCD correction factor

$g\left(\cot\beta, \frac{m_{H^+}}{m_{W^+}}, \frac{m_t}{m_{W^+}}, \frac{m_b}{m_{W^+}}\right)$ is given in reference [19]

The factor $f_B B_B^{1/2}$ is due to the short range hadronic contribution to the matrix element and recent lattice computations estimate $100 < f_B B_B^{1/2} < 180$ MeV [24]. The calculated value may then be compared with the measured value

$$\chi_d = 0.73 \pm 0.18$$

$K - \bar{K}$ mixing is exactly the same as $B_d^0 - \bar{B}_d^0$ mixing except that the bottom quark is replaced with a strange quark in the box diagram so that the contribution due to the charged Higgs is

$$\Delta M_K^H = \frac{|V_{ts}V_{td}^*|^2}{|V_{tb}V_{td}^*|^2}\frac{f_K^2 m_K}{f_B^2 m_B}\Delta M_B^H$$

Since the standard model calculation has considerable theoretical uncertainty constraints are set by requiring that the

$$\Delta M_K^H < \Delta M_K^{experiment} = \pm(3.5 \pm 0.014).10^{-13}\text{GeV}$$

The same box diagrams contribute to the ϵ parameter in CP violation in $K - \bar{K}$ system. The calculation is sensitive to the bag factor B_K which is not well known. The expression for ϵ in given in reference [25] and this can be compared to measured value [26]

$$\epsilon = (2.2259 \pm 0.018).10^3$$

1.7.3 Penguin decays of bottom quark

The $b \to s\gamma$ may be mediated by the so called penguin diagram (figure 1-8).

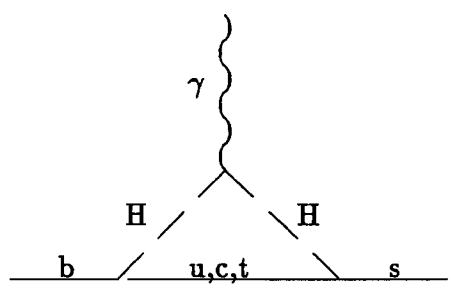

Figure 1-8: The Feynman "penguin" diagram for the process $b \to s\gamma$

The width of this decay for both standard model and charged Higgs contributions is given below. The contribution is different for model I and model II [27].

$$\Gamma_{b\to s\gamma} = \frac{\alpha G_F^2 m_b^5}{128\pi^4}\left|\sum_{i=u,c,t} V_{is}V_{ib}^* G_W(\frac{m_i}{m_{W^+}}) + aG_H^{(1)} + \cot^2\beta G_H^{(2)}(\frac{m_i}{m_{H^+}})\right|^2$$

where

$a = -\cot^2\beta$ for model I

$a = 1$ for model II

G_W is the standard model contribution. $G_H^{(1)}, G_H^{(2)}$ are the charged Higgs contributions. and explicit forms for them are given in reference [19].

QCD radiative corrections are significant [28]. In reference [27] the above expression has been calculated including the radiative corrections. The radiative corrections use a value of the QCD scale, Λ, so as to obtain consistency with the measured value of $\alpha_s(M_z^2)$ at LEP [10]. The results in a standard model contribution of

$$Br(b \to s\gamma) = (2.56 - 3.94).10^{-4} \qquad 90 < m_t < 200 \text{ GeV}$$

In model I there is only substantial enhancement for low values of $\tan\beta$. In model II there is an enhancement for all values of $\tan\beta$. The best published limit is from CLEO [29]

$$Br(b \to s\gamma) < 0.84.10^{-3}$$

In model I this implies $\tan\beta > 0.5$ for $m_t > 60$GeV and $m_{H^+} < 100$GeV. Similarly in model II $\tan\beta > 1.0$ for $m_t > 60$GeV and $m_{H^+} < 100$GeV.

1.7.4 Constraints on m_t

The best decay independent limit on the top (i.e irrespective of whether it decays to a charged Higgs or a W^+) is given by the total width of the W^+ decay (Note that the current best limit assuming the top decays exclusively to the W^+ is $m_t > 108$ GeV [1]). The total width of the W^+ is sensitive to all of the W^+ decay modes irrespective of whether they are observed or not. In particular if the top mass is less that the W^+ mass then $W^+ \to tb$ will contribute to the total width. This contribution will be the same irrespective of how the top subsequently decays.

$$\Gamma_W^{total} = \Gamma_{W\to e\nu} + \Gamma_{W\to\mu\nu} + \Gamma_{W\to\tau\nu} + \Gamma_{W^+\to ud} + \Gamma_{W^+\to cs} + \Gamma_{W^+\to tb}$$

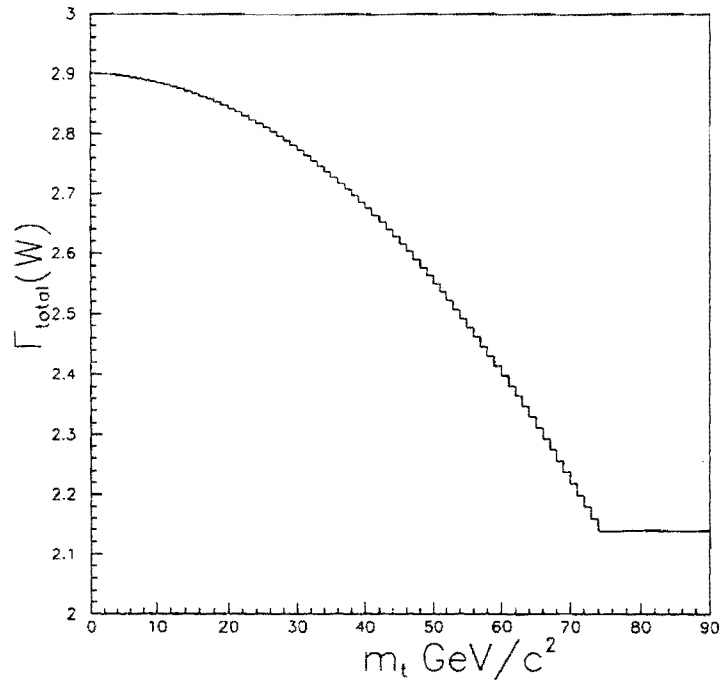

Figure 1-9: The dependence of the total width of the W^+ boson on the mass of the top quark.

The width of the W^+ decreases from 2.8 to 2.1 GeV as m_t increases from 0 to m_{W^+} (figure 1-9) because the contribution from $W^+ \rightarrow tb$ decreases The total width has been measured by CDF,UA1,UA2 [30]. If the results are combined then

$$m_t > 55 \text{ GeV}$$

1.7.5 Limits from $p\bar{p}$ experiments

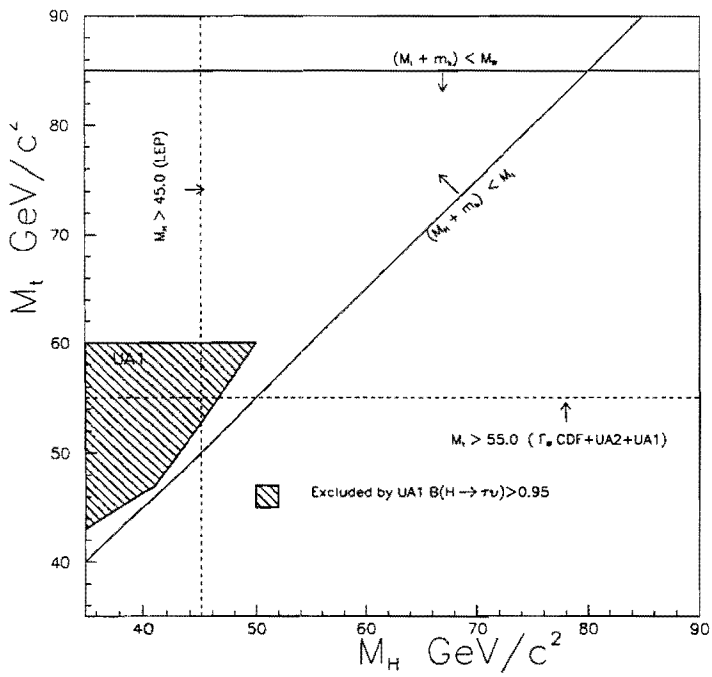

Figure 1-10: The excluded regions of m_t, m_{H^+} for $Br(H^+ \rightarrow \tau\nu_\tau) > 0.95$ from UA1 experiment, at 95 % confidence limit. Also shown are the limits on m_{H^+} and m_t which are independent of $Br(H^+ \rightarrow \tau\nu_\tau)$ from LEP data. The region in which W^+ boson decays are suppressed $m_t < m_{W^+} + m_b$, $m_{H^+} < m_t - m_b$ is also shown

UA1 has reported results on a search for $p\bar{p} \rightarrow W^+ \rightarrow tb \rightarrow \mu\nu b\bar{b}$ [31]. They search for a muon plus two jets or dimuon plus jet signature. The analysis is similar to the UA1 standard top search [32] except that the required P_T of the muon is lowered. They observe no evidence of this decay and are able to exclude regions of the m_t, m_{H^+} and $m_{H^+}, \tan\beta$ planes for Model II (figure 1-10).

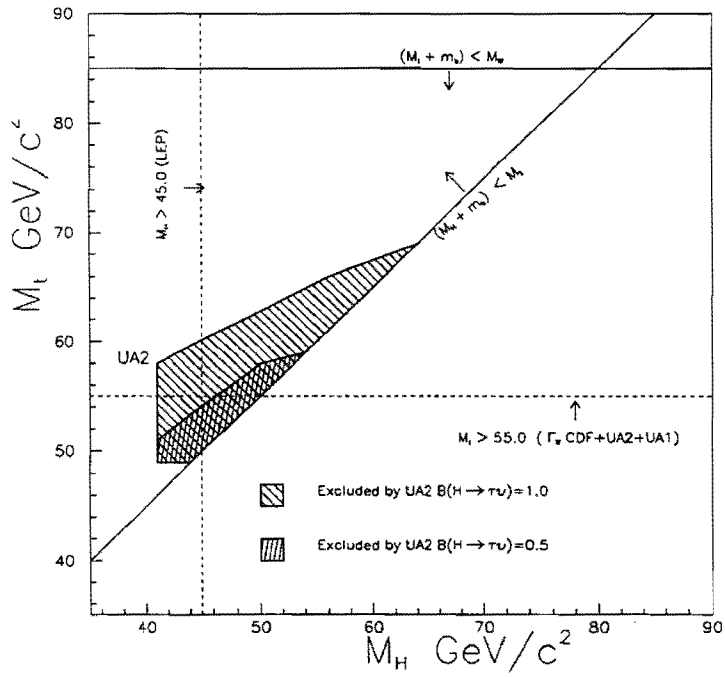

Figure 1-11: The excluded regions of the m_t, m_{H^+} plane for $Br(H^+ \rightarrow \tau\nu_\tau) > 0.5, 1.0$ from UA2 experiment, at 95 % confidence limit. Also shown are the limits on m_{H^+} and m_t which are independent of $Br(H^+ \rightarrow \tau\nu_\tau)$. The region in which W^+ boson decays are suppressed $m_t < m_{W^+} + m_b$, $m_{H^+} < m_t - m_b$ is also shown

UA2 has also reported results on a search for $p\bar{p} \rightarrow W^+ \rightarrow tb \rightarrow \tau\nu b\bar{b}$ [33] They look for a hadronic tau plus jet plus $\not{E}_T$ signature. . Again no signal is observed and the authors set limits for model II for $Br(H^+ \rightarrow \tau\nu_\tau)$ =0.5,1.0 (figure 1-11).

1.8 Theoretical Constraints on $m_t, m_{H^+}, \tan\beta$

Some semi-quantitative constraints can be placed on $m_{H^+}, \tan\beta$ by requiring that the H^+ width not be too wide and the $t\bar{b}H^+$ coupling remain perturbative [19]. The width and the $t\bar{b}H^+$ coupling both increase rapidly with m_t and

so the theory may become non-perturbative for some values of the parameters. However, this is not a physical limitation but rather a restriction on the theoretically calculable region. The definition of the boundary of the perturbative region varies but the one adopted in reference [19] is to require that Γ/m is not too large for both the top and the charged Higgs. If $m_{H^+} > m_t + m_b$ then

$$\frac{\Gamma_{H^+}}{m_{H^+}} \approx \frac{3G_F m_t^2}{4\sqrt{2}\pi \tan^2\beta} \tag{1.10}$$

If we require $\Gamma_{H^+}/m_{H^+} < 1/2$ then equation 1.10 implies

$$\tan\beta \gtrsim \frac{m_t}{500\text{GeV}} \tag{1.11}$$

If $m_t > m_{H^+} + m_b$ then

$$\frac{\Gamma_t}{m_t} \approx \frac{3G_F m_t^2}{8\sqrt{2}\pi \tan^2\beta} \tag{1.12}$$

The requirement $\Gamma_t/m_t < 1/2$ implies a similar bound to equation 1.11. Additionally, the requirement that the $t\bar{b}H^+$ coupling be smaller that the QCD coupling $g_s = 4\pi\alpha_s(m_{W^+}^2) \approx 1.5$ requires

$$\tan\beta \gtrsim \frac{m_t}{600\text{GeV}} \tag{1.13}$$

The above constraints are valid for models I-IV. For the range of m_{H^+}, m_t under consideration imply $\tan\beta \gtrsim 0.1$. Also in models II and III there are corresponding upper bounds obtained from equations 1.11 and 1.13 by replacing $m_t \rightarrow m_b$ and $\tan\beta \rightarrow \cot\beta$. This implies $\tan\beta \lesssim 100 - 200$. An analysis of the one loop heavy fermion corrections to the $Z \rightarrow H^+H^-$ vertex [34] results in similar bounds to equations 1.11 and 1.13.

1.9 CDF search region

It is only feasible to identify a $t \rightarrow H^+b$ decay if the Higgs decays to a tau. This is because a $H^+ \rightarrow$ jets signature is dominated by the large QCD background in a $p\bar{p}$ environment. We will therefore only consider cases with a significant tau branching ratio: $Br(H^+ \rightarrow \tau\nu_\tau) > 0.3$. This is true for each of the models as follows (figure 1-6).

Model I - all values of $\tan\beta$

Model II - $\tan\beta > 1$

Model III - $\tan\beta < 1$

Model IV - $\tan\beta > 1$

Next we need to consider the choice of parameters which suppress the standard model decays. The branching ratio of the top to Higgs is given by

$$\mathrm{Br}(t \to H^+b) = \frac{\Gamma(t \to H^+b)}{\Gamma(t \to H^+b) + \Gamma(t \to W^+b)}$$

Using the expressions for the widths (equations 1.8, 1.9, 1.6) we can estimate $\mathrm{Br}(t \to H^+b)$ for each of the models.

Model I

$$\Gamma(t \to H^+b) \propto \left[\cot^2\beta(1 + \left(\frac{m_b}{mt}\right)^2\right] + \text{constant}$$

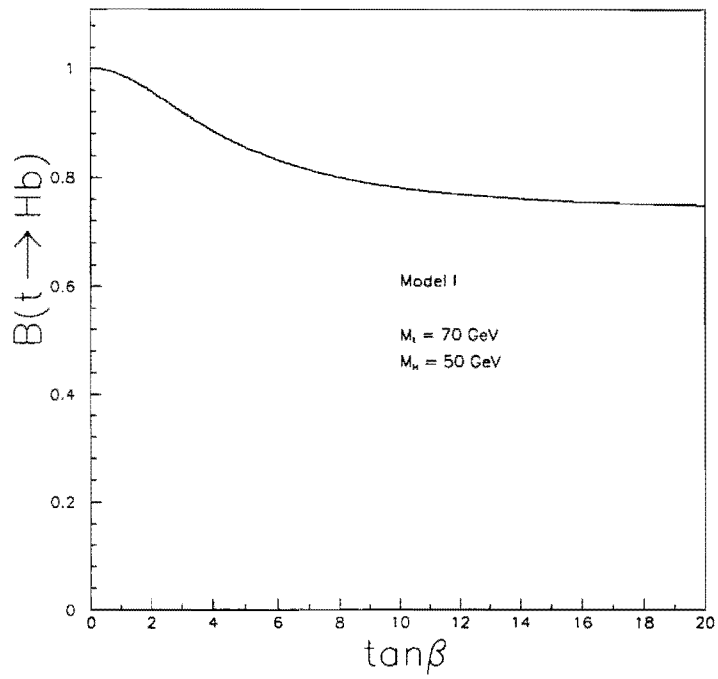

Figure 1-12: The $Br(t \to H^+b)$ for $m_t = 70.0$ GeV , $m_{H^+} = 50$ GeV for model I of the two Higgs doublet model.

Figure 1-12 shows that $Br(t \to H^+b)$ tends to a constant for $\tan\beta > 5.0$. The highest $Br(t \to H^+b)$ occurs for low $\tan\beta$. Figure 1-13 shows the values of the branching ratio: $Br(t \to H^+b)$, for $\tan\beta$ =0.5,5.0.

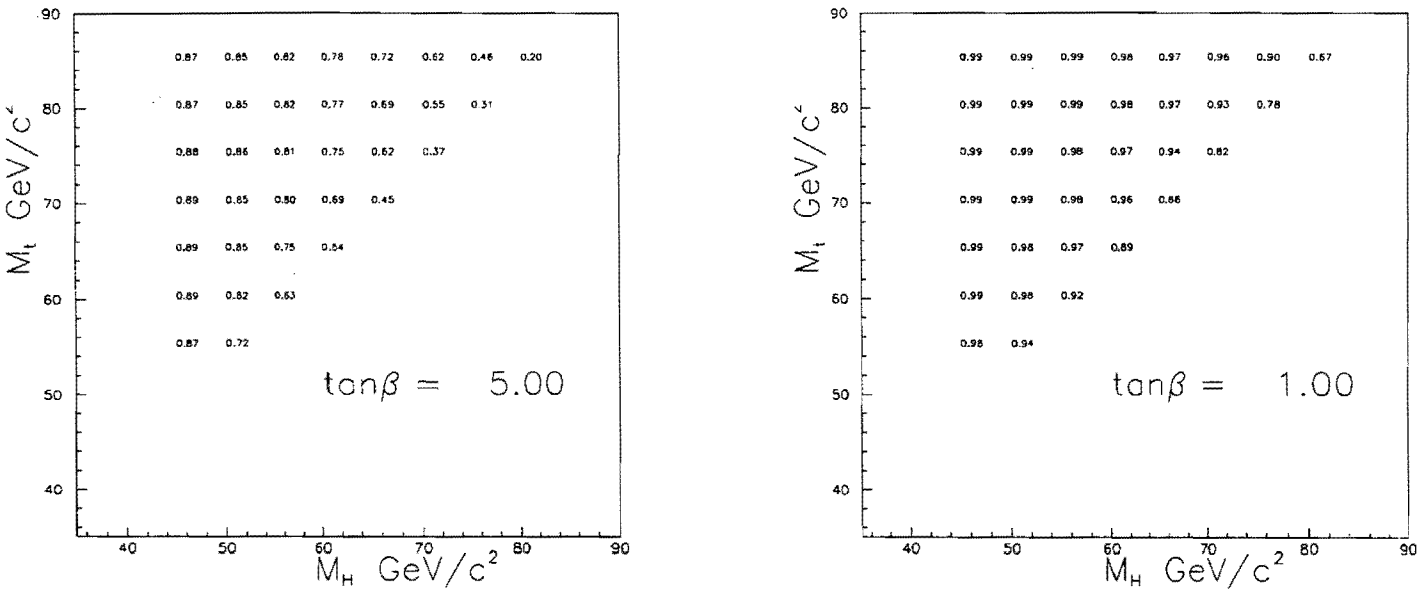

Figure 1-13: The $Br(t \rightarrow H^+b)$ for m_t, m_{H^+} in Model I of the two Higgs doublet model.

Model II

$$\Gamma(t \to H^+b) \propto \left[\cot^2\beta + \tan^2\beta . \left(\frac{m_b}{mt}\right)^2\right]$$

This has a minimum when

$$\tan\beta_{min} = \sqrt{\frac{m_t}{m_b}}$$

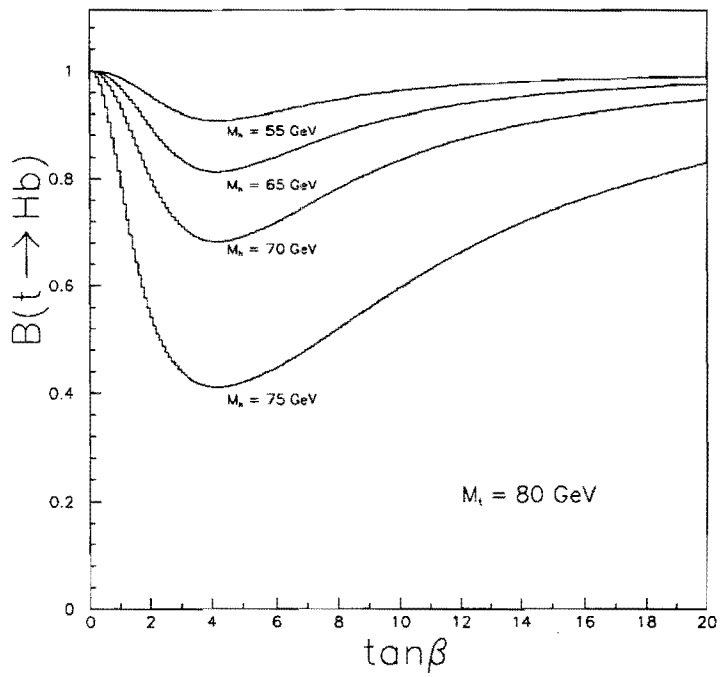

Figure 1-14: The branching ratio, $Br(t \to H^+b)$, for $m_t = 80.0$ GeV and different m_{H^+} showing the minimum at $\tan\beta_{min}$.

Figure 1-14 shows $Br(t \to H^+b)$ for a particular case of $m_t = 80$GeV vs $\tan\beta$ and figure 1-15 shows the values of the minimum branching ratio: $Br(t \to H^+b)$, for m_t, m_{H^+}.

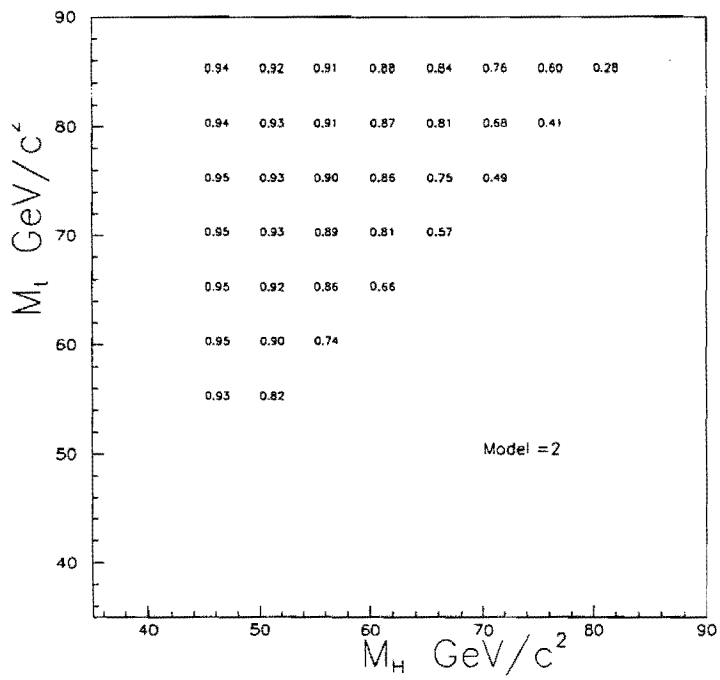

Figure 1-15: The minimum $Br(t \rightarrow H^+b)$ for m_t, m_{H^+} at $\tan\beta_{min}$.

Models III and IV have exactly the same $Br(t \rightarrow H^+b)$ as models II and I respectively. We can combine these observations on $Br(t \rightarrow H^+b)$ and $Br(H^+ \rightarrow \tau\nu_\tau)$ to see which models we are sensitive to. In each of the models a substantial $Br(t \rightarrow H^+b)$ is possible. In a search requiring a tau signature we will have greatest sensitivity if $Br(H^+ \rightarrow \tau\nu_\tau)$ is large when $Br(t \rightarrow H^+b)$ is large.

1. **Model I** Largest sensitivity for $\tan\beta < 1.0$ since $Br(H^+ \rightarrow \tau\nu_\tau)$ is constant and $Br(t \rightarrow H^+b)$ is largest for small $\tan\beta$.

2. **Model II** $Br(t \rightarrow H^+b)$ is large for $\tan\beta < 2.0$ and $\tan\beta > 4.0$ (because of the minima in figure 1-15). $Br(H^+ \rightarrow \tau\nu_\tau)$ is zero for small $\tan\beta$ and large for large $\tan\beta$ so we will be most sensitive in the region $\tan\beta > 2.0$.

3. **Model III** $Br(t \rightarrow H^+b)$ is large for $\tan\beta < 2.0$ and $\tan\beta > 4.0$ (because of the minima in figure 1-15). $Br(H^+ \rightarrow \tau\nu_\tau)$ is zero for large $\tan\beta$ and

constant for small $\tan\beta$ so we will be weakly sensitive for $\tan\beta < 1.0$.

4. **Model IV** $Br(t \to H^+b)$ is largest for small $\tan\beta$ and tends to significant constant for higher $\tan\beta$. $Br(H^+ \to \tau\nu_\tau)$ is zero for small $\tan\beta$ and large for higher $\tan\beta$. We expect to be sensitive at $\tan\beta > 1.0$ similar to model II.

In summary we will be sensitive to models II and IV for $\tan\beta > 2.0$ and model I for $\tan\beta < 1.0$. However, low energy data tends to exclude the second possibility. Therefore the most interesting cases are model II and IV. Model II also has the same Higgs structure as the minimal supersymmetric model. However this model requires $m_{H^+} > m_{W^+}$. This is a region where the standard decays of the top are not greatly suppressed. There are many other models which have a charged Higgs structure similar to the possibilities of the THD. We will interpret our results in terms of $Br(t \to H^+b), Br(H^+ \to \tau\nu_\tau)$ (i.e in a model independent way) and in terms of $\tan\beta$ for the THD.

Chapter 2

The Collider Detector at Fermilab

The Fermilab Tevatron collider provides the highest energy collisions ever observed at a collider experiment. It collides equal energy beams of protons and antiprotons at a center of mass energy of 1.8 TeV. The Collider Detector at Fermilab(CDF) [35] is designed to study the most interesting of these interactions. To maximize the utility of the detector, and hence the potential to discover new physics, it is designed in the most general purpose way.

The detector consists of a variety of subsystems designed to complement each other and provide flexibility. It is approximately cylindrically symmetric with the axis defined by the proton-antiproton beams. The subsystems themselves are arranged schematically as a set of concentric cylinders centered about the nominal interaction point. The detector is shown in figure 2-1. It is segmented into two parts. There is the central region which can be moved in and out of the collision hall, and the end caps (known as the forward/backward regions) which are permanently mounted. Figure 2-2 shows the defined coordinate system. The origin $x = y = z = 0$ is at the center of the detector. The positive z direction is that of the protons and the positive y direction is up. ϕ is the azimuthal angle about the z axis (beam axis) with ϕ =0 being the positive x axis. The polar angle θ is defined with θ=0 as the positive z axis.

Frequently the polar co-ordinate is described in terms of the pseudorapidity, η, defined as

$$\eta = \ln(\cot\frac{\theta}{2})$$

η is equivalent to the rapidity, y, for a massless particle where rapidity is defined as

$$y = \frac{1}{2}\ln\left(\frac{E + P_z}{E - P_z}\right)$$

If $E \gg m$ then $\eta \approx y$. Particle production in $p\bar{p}$ collisions is best described in terms of y and P_T. This is because, if the system is Lorentz boosted along the z axis with a velocity u, then P_T is unchanged and y is a simple additive quantity

$$y' = y + y_{boost}$$

where

$$y_{boost} = \frac{1}{2}\log\left(\frac{1 + u}{1 - u}\right)$$

This simplicity of the transformation is important because the scattered quark system is often boosted in the z direction. This is because, although the proton and antiproton have equal beam energies, the constituent quarks do not necessarily carry equal fractions of the proton and antiproton momentum. For this reason, we will often use η in describing both the detector geometry and the particle kinematics.

The nominal vertex at $x = y = z = 0$ is often referred to as the detector vertex. The event vertex is the actual interaction point. In general, the event vertex differs from the detector vertex because of the finite length of the proton and anti-proton bunches. It is distributed in the z direction about z=0 and with a width of approximately 30 cm.

In this thesis, almost all of the detector subsystems are used. The calorimeters are used to implement a missing transverse energy trigger and also to identify energy clusters from jets, taus and electrons. The finite resolution of the calorimeters convolutes into a finite missing transverse energy resolution which is significant since the cut on missing transverse energy is the dominant

inefficiency in the analysis. The tracking is used to associate the tracks from the taus and electrons with the calorimeter energy clusters. The tracking detectors are used to find and associate tracks with the energy clusters and with the event vertex. The reconstruction of the event vertex is important since this again affects the calculation of missing transverse energy. The vertex is also used to require that all the tracks associated with an energy cluster also come from the primary interaction point. The final signal variable that we use is the number of tracks associated with a tau calorimeter cluster. This is facilitated by the extremely high track reconstruction efficiency that is possible with the central tracking chamber.

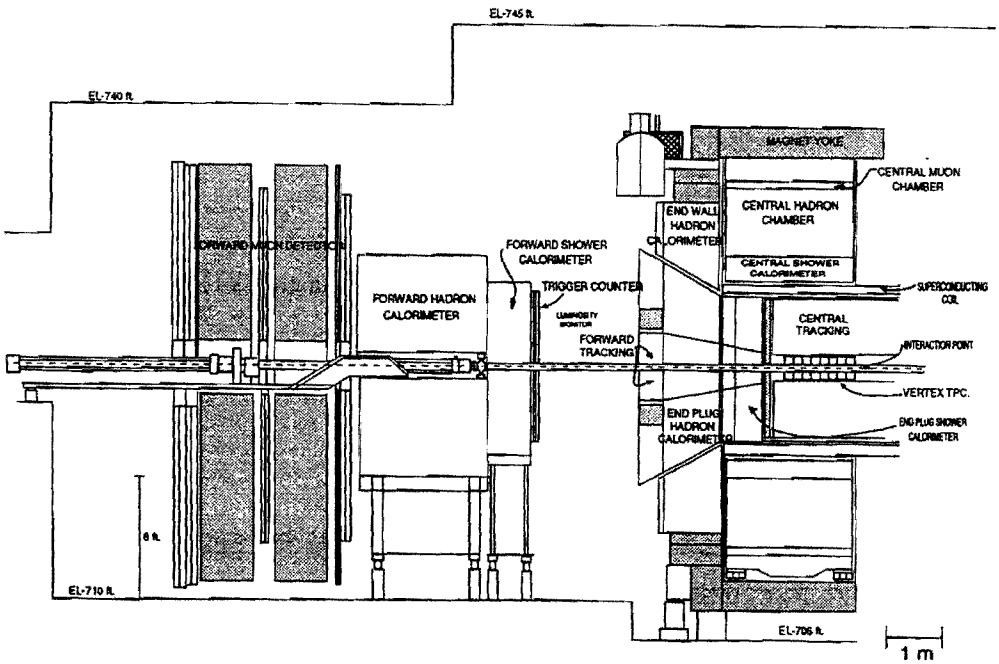

Figure 2-1: The Collider Detector at Fermilab (CDF) showing the movable central detector and fixed forward/background detector. Only half the detector is shown. The other half is the mirror image of that shown.

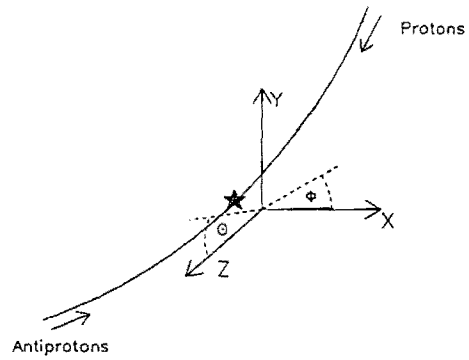

Figure 2-2: The definition of a co-ordinate system for the CDF detector.

2.1 Tracking detectors

Figure 2-1 shows the two central tracking detectors, the Vertex Time Projection Chamber (VTPC) and the Central Tracking Chamber (CTC) which both sit inside a uniform magnetic field of 1.41 Tesla, generated by a superconducting solenoid. The field is parallel to the beam axis so that the particles are bent in the r-ϕ plane. The functions of the tracking detectors are to measure accurately the P_T of the tracks and to reconstruct the event vertex. The event vertex is needed to calculate the E_T (in the calorimeter since $E_T = E.\sin\theta$). Additionally it provides a measure of how well contained the event is in the detector. It can also identify multiple interactions (i.e more than one vertex). The VTPC is the innermost tracking detector and its primary function is to reconstruct the vertex. A time projection chamber is used because it has good position

resolution in three dimensions. It also has the capability to deal with many tracks. There are typically 30 or more tracks with $P_T > 0.4$ GeV in a $p\bar{p}$ interaction at $\sqrt{s}$=1.8 GeV. Outside of the VTPC is the CTC which is a much larger drift chamber designed to give excellent position resolution in the r-ϕ plane and thus to accurately measure the P_T of the tracks. We now describe in detail these two detectors subsystems.

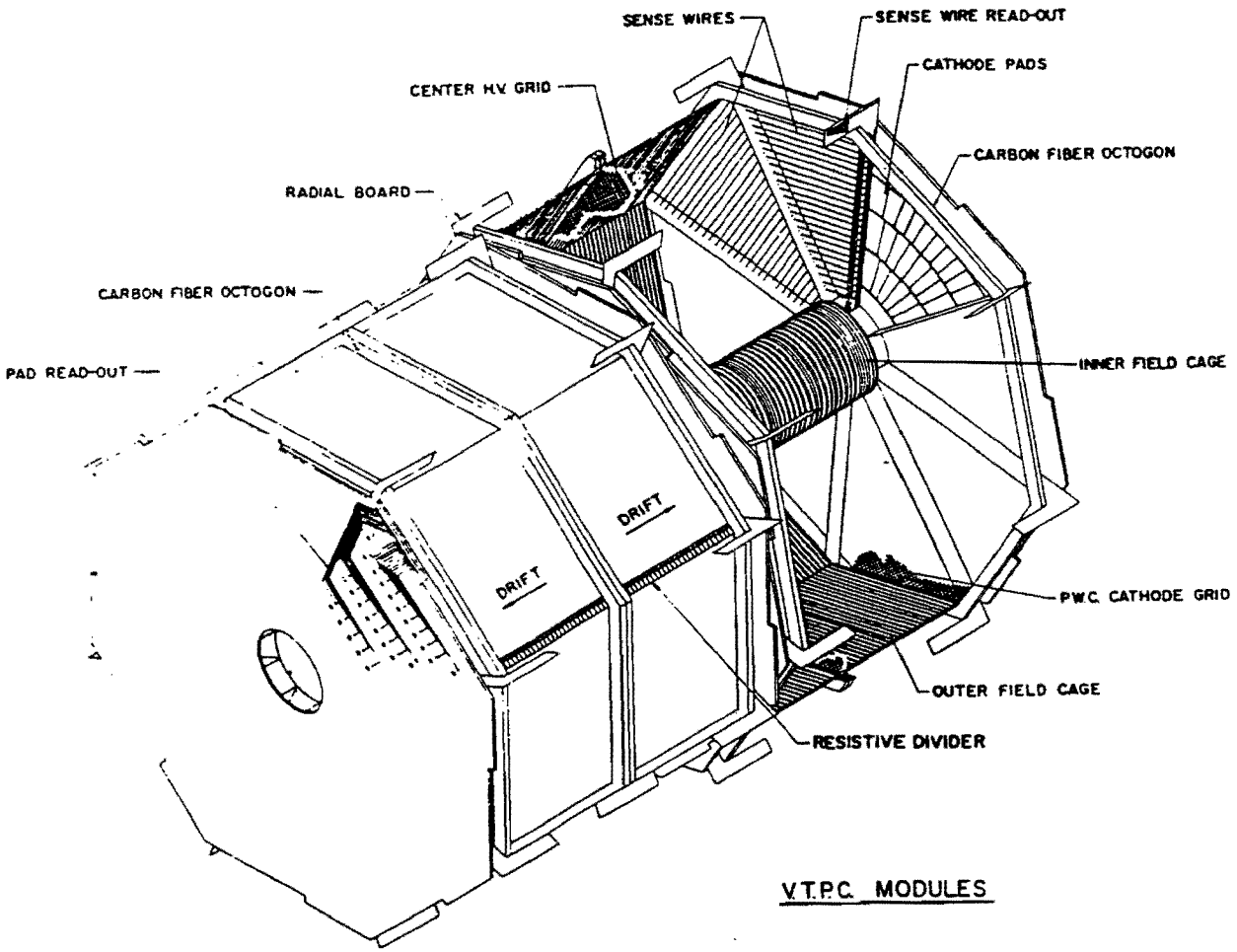

Figure 2-3: The vertex time projection chamber.

2.1.1 The vertex time projection chamber

The Vertex Time Projection Chamber (VTPC) [36] lies immediately around a thin beam pipe (500 μm). The beam pipe is made from berylium, a low mass material, so as to minimize the probability of a particle interacting with it. Similarly the VTPC is constructed of low mass materials. A time projection chamber is a drift chamber in which the electric drift field is parallel to the magnetic field. As an electron drifts it tends to wind about the electric drift field lines. This minimizes the diffusion of the electron in the gas, enhancing the position resolution. Figure 2-3 shows the construction of the VTPC. It consists of eight octants each containing two drift chambers which cover the region -3.5 $< \eta <$3.5. The VTPC is 2.8 m long with an outer radius of 20 cm. The drift field in each module is formed by a central cathode grid and two cathode grids at either end. Outside the two cathode grids of each octant lie 24 sense wires strung along chords of circles centered on the beam axis, and 24 cathode pads segmented in phi. The cathode grids, sense wires, and pads form a proportional chamber where the electrons avalanche and thus cause an amplification of the signal. The sense wires are instrumented with time to digital converters (TDC). The TDC's measure the time taken for the electrons to drift from the ionization point to the sense wires, and hence give a z coordinate for the track path. The pads are connected to flash analogue to digital converters (FADC) to give pulse height information that can be used to measure the track ϕ coordinate. The maximum drift distance, voltage and gas conditions determine the drift time. These have been chosen so that the drift time is less than the 3.5 μs interval between two beam crossings when the collider is in six bunch mode. The gas is a 50:50 mixture of argon and ethane, which is typical for drift/proportional chambers. Argon is chosen because it gives good avalanche multiplication at low fields, has high specific ionization, is inert, and is cheap. However, in pure argon, excited atoms are formed during the avalanche process which can only de-excite through emission of a photon. The minimum energy of the emitted photon is well above the energy of the ionization of the metal of the cathode,

and so photo-electrons are emitted. These can then cause a new avalanche which quickly leads to continuous discharge. Ethane is added because it has a large number of metastable excited states which can absorb the photon and then dissipate the energy either by harmless elastic collisions or disassociation into radicles. Additionally, because the ethane is so effective at absorbing the energy of the gas, the effective temperature of the drifting electron in the drift region is decreased. This causes a decrease in diffusion perpendicular to the drift direction which enhances spatial resolution. Figure 2-4 shows the hit distribution for a typical event. The vertex is identified by the following procedure:

- Identify associated sets of hits in each octant and make linear fits. Each candidate track formed and used in the vertex finding must pass the following criteria
  - Number of hits ≥ 6
  - Occupancy of track ≥ 70 %
  - $\chi^2 \leq 1000$
- Calculate the Z intercepts of each track and order in decreasing Z. Move a window of 1.5 cm along Z axis until the point where the maximum number of intercepts is found.
- Calculate the Z mean of the intercepts in the 1.5 cm window
- Iterate this procedure to find all candidate vertices.
- Accept a vertex as a good vertex if there are more than 180 hits associated with it.
- If there are two good vertices identify the primary vertex as the one with the most number of associated hits.

The spatial resolution is typically 200-500 μm per hit which results in a z vertex resolution of 2 mm. The ability of the VTPC to deal with a high track

multiplicity is demonstrated figure 2-4. The probability of multiple interactions for a luminosity of $1.0 \times 10^{30}\, cm^{-2}\, sec^{-1}$ is approximately 8 %. However, the second interaction is almost always a minimum bias interaction and so this interferes very little with the overall event topology.

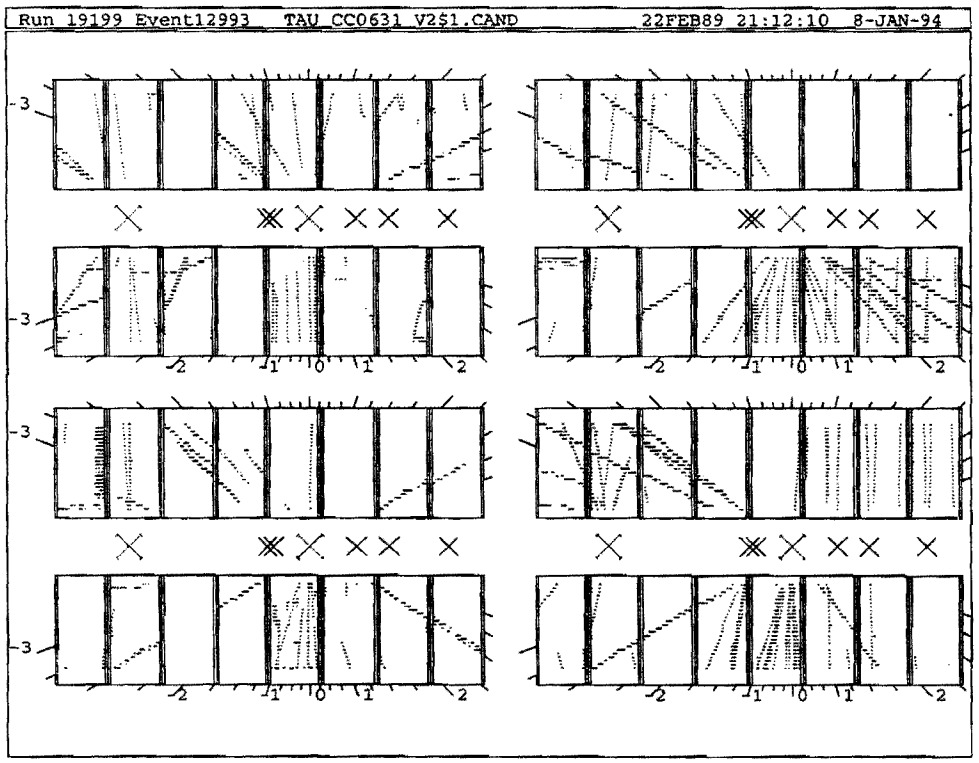

Figure 2-4: A typical event in the vertex time projection chamber. The reconstructed track segments for the eight octants are shown.

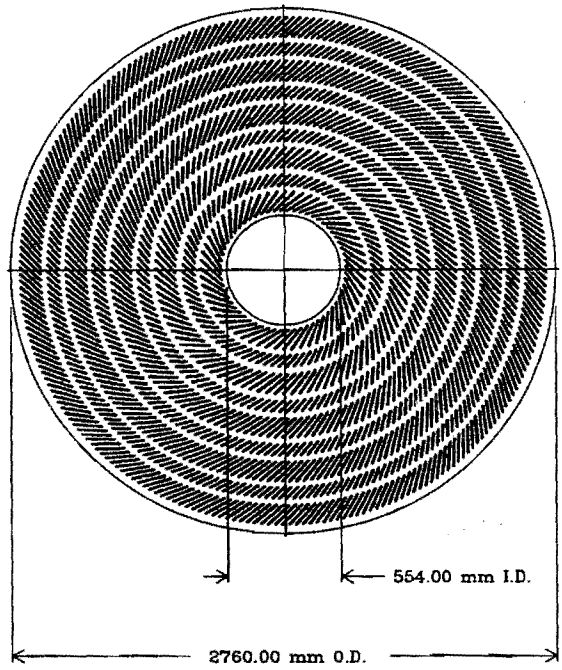

Figure 2-5: The superlayer structure of the central tracking chamber.

2.1.2 The central tracking chamber

The central tracking chamber (CTC) [37] is a 3.2m long cylindrical drift chamber which accurately measures co-ordinates of charged particle trajectories in the r-ϕ plane and less accurately in the r-z plane. The inner radius of the CTC is 0.55 m and the outer radius is 2.76 m. The CTC surrounds the VTPC and sits inside a uniform 1.4T solenoidal magnetic field. The magnetic field bends the trajectories in the r-ϕ plane and thus provides an accurate measurement of the track P_T. Additionally the CTC is designed to give excellent two track resolution which is important because of the high track multiplicity of a typical event. This feature is especially significant in this thesis since it enables the identification of a hadronic tau lepton decays by means of a track multiplicity variable. The drift cells are arranged in concentric cylindrical layers which are grouped into nine superlayers as shown in figure 2-5. Five of the

superlayers each contain 12 sense wire layers which are strung parallel to the beam axis and this provides the r-ϕ co-ordinate. The other four superlayers are interleaved with the axial layers and have wires which are canted at 3° with respect to the beam axis to provide a stereo measurement in the r-z plane. The drift cells are tilted with respect to the radial direction to compensate for the lorentz angle (β) and make the drift direction azimuthal. This simplifies the time to distance relationship. Additionally it allows the cells to overlap which helps resolve the left right ambiguity since the ghost track is rotated by an angle $\delta = \tan^{-1}(2\tan\beta)$. The chambers use an argon/ethane/alcohol mixture (ethanol is added to reduce aging effects due to polymerization of ethane). They are run at an electric field strength that is sufficient to ensure that the drift velocity v is independent of E. To measure a hit co-ordinate in a drift chamber it is necessary to know the time at which the ionization occurred t_0, and the drift velocity v. Then if t is the time at which the avalanche reaches the sense wire, the position δX is given by

$$\delta X = v(t - t_0)$$

The t_0 are determined by demanding that the tracks be continuous as they cross the plane of sense wires in a particular cell. The drift velocity is determined by requiring that the tracks be continuous as they cross the boundary between two r-ϕ cells. The tilt of the cells ensures overlap and facilitates this calibration. Drift velocity and t_0 are determined online during each run. The r-ϕ, r-z hit coordinates can be determined to within 200 μm and 6 mm respectively. The track P_T is measured with a resolution of $\delta P_T/P_T^2 < 0.002$ for $-1.0 < \eta < 1.0$. The two track resolution is 3.5 mm. Tracks with $P_T < 400$ MeV curl up within the detector. Tracks with $P_T > 1.0$ GeV and $-1.0 < \eta < 1.0$, and which are reasonably well separated, are reconstructed with nearly 100 % efficiency.

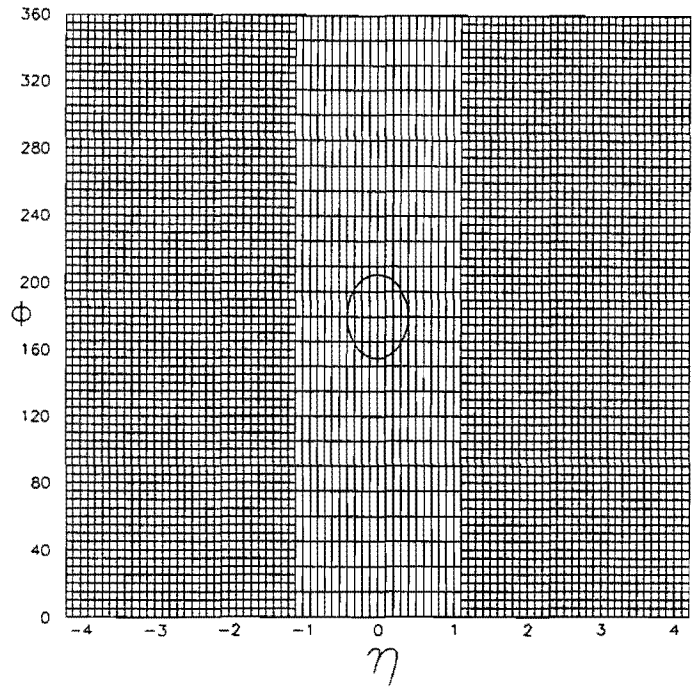

Figure 2-6: The $\eta - \phi$ segmentation of the CDF calorimeter. Also shown is the size of a cone cluster with a 0.4 radius. This is the cone clustering radius used in the analysis.

2.2 Calorimeters

The calorimeters, which measure the energy and position of leptons and jets, cover almost all of the 4 π solid angle. They are segmented into towers of 0.1 units of pseudorapidity as projected from the detector vertex. All of the calorimeters are of the sampling type using lead/scintillator or lead/gas for the electromagnetic calorimeters and iron/scintillator or iron/gas for the hadronic calorimeters. There are three regions, central ($|\eta| < 1.1$), plug ($1.1 < |\eta| < 2.2$) and forward ($2.2 < |\eta| < 4.2$). The towers are segmented azimuthally by 15° in the central and by 5° in the plug and forward as shown in figure 2-6.

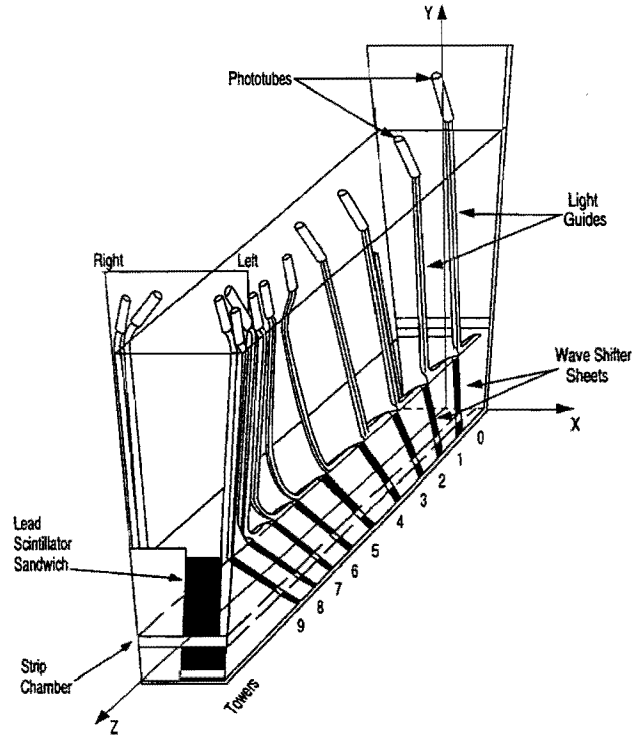

Figure 2-7: A CEM module.

2.2.1 The central calorimeters

The central calorimeters are constructed in 15° wedges and assembled into arches which surround the CTC to give full azimuthal coverage. Figure 2-7 shows a central electromagnetic calorimeter (CEM) [38] module. It consists of 30 layers of 1/8 inch aluminium clad lead sheets with 31 layers of 5mm thick polystyrene scintillator. Each tower is 18 radiation lengths which is sufficient to contain most electron showers. The light from the scintillators is transmitted to the photomultiplier tubes at the rear of each wedge by a wave shifter bar followed by an acrylic light guide. Each CEM tower was calibrated using 50 GeV electrons from a testbeam. The calibration was then maintained to within 2.5 % by Cs^{137} signals over several years. The overall energy scale is set by

studying E/p for electrons. The measured energy resolution is

$$\left(\frac{\sigma}{\mathrm{E}}\right)^2 = \left(\frac{13.5\%}{\sqrt{\mathrm{E}\sin\theta}}\right)^2 + 0.02^2$$

A gas proportional chamber is installed at the shower maximum to accurately measure the shape and position of electromagnetic showers. This chamber consists of 64 wires along the z direction which provide the r-ϕ co-ordinate, and 1128 strips in the r-ϕ azimuthal direction which provide the z co-ordinate. The position resolutions is 2mm for 50 GeV electrons.

The central hadronic calorimeter (CHA) [39] sits outside the CEM and has identical segmentation. The CHA ($|\eta| < 0.8$) consists of 32 layers of 1.0 cm scintillator and 2.5cm of steel. The wall hadron calorimeter (WHA) (0.8 $< |\eta| < 1.1$) is constructed of 15 layers of 1 cm thick scintillator and 5 cm steel. All of the CHA modules and two of the WHA modules were calibrated at the testbeam with pion beams ranging from 10 GeV to 150 GeV and cross-checked and maintained with Cs^{137} sources.

2.2.2 Plug calorimeters

The plug electromagnetic calorimeter (PEM) and the plug hadronic calorimeter (PHA) cover the region ($1.1 < |\eta| < 2.4$). The PEM is divided into four quadrants, each of which consists of 34 layers of proportional tubes interleaved with 2.5 mm sheets of lead. Each layer has a pad readout formed by etching the projective tower geometry from copper plated G10 panels. Longtitudally the pads are ganged together in each tower to form three depth segments. Ten layers of the PEM near shower max have finely segmented cathode strips as well as pads in order to provide more accurate position and shape information. Each of the 2304 towers were calibrated with 100 GeV electrons in a testbeam. The resolution was measured to be

$$\frac{\sigma}{\mathrm{E}} = \frac{28\%}{\sqrt{\mathrm{E}}} \pm 2\%$$

The PHA is divided into twelve 30° stacks of 20 layers of proportional tubes interleaved with 5cm sheets of steel. The pads are also etched with the projective tower geometry and are ganged together longtitudally to form one depth segment. The PHA is calibrated in a pion testbeam using the the central tower of every 30° stack. The resolution for single pions is measured to be

$$\frac{\sigma}{E} = \frac{86\%}{\sqrt{E}} \pm 4\%$$

2.2.3 The forward calorimeters

The forward electromagnetic calorimeter(FEM) [40] and forward hadronic (FHA) cover the region $(2.4 < |\eta| < 4.2)$. The FEM consists of four quadrants of 30 layers of proportional tubes interleaved with 48 mm lead sheets. The pad readout in each layer is etched with the projective geometry and the towers are ganged into two depth segments. The FEM is calibrated with 20-200 GeV testbeam electrons. The measured resolution for single electrons is

$$\frac{\sigma}{E} = \frac{25\%}{\sqrt{E}} \pm 0.5\%$$

The response is linear up to 100 GeV and has a 10 % non-linearity at 200 GeV. The FHA is also divided into four quadrants of 27 layers of proportional tubes and 5 cm steel plates. The pads are ganged to form a projective tower with one depth segment. The FHA has full azimuthal coverage only up to $|\eta| < 3.6$ since it is built around the low beta quadrupoles of the accelerator. The resolution for single pions is measured to be

$$\frac{\sigma}{E} = \frac{140\%}{\sqrt{E}}$$

2.3 The muon detectors

The central muon detector [41] consists of drift tubes mounted directly on the CHA. It covers the region $0.03 < |\eta| < 0.63$ and has full azimuthal coverage. There are four layers of tubes. The sense wires, which are parallel to the beam

axis, are aligned radially but with the wires from the second and fourth layer offset by 2 mm in order to resolve the left right ambiguity. The z coordinate is determined by charge division along the wire. The ϕ co-ordinate is determined from the drift times. The tracks can be matched with the CTC tracks. Since there were only 6 absorbtion lengths of material in front of the muon detector the probability of pion punch through is quite high (40 % for 50 GeV pions). The spatial resolution was 1.2 mm in z and 0.25 mm in ϕ. The forward muon spectrometers cover the regions from $2.0 < |\eta| < 3.6$. Each spectrometer consists of a magnetized steel toroid with three layers of drift chambers and two layers of scintillation counters. The reconstructed tracks are matched to the VTPC.

2.4 Trigger

At a typical tevatron luminosity of $10^{30}\,cm^{-2}\,sec^{-1}$ the collision rate at $\sqrt{s} =$ 1.8 TeV is approximately 47 KHz. The rate at which the CDF is capable of writing data to tape is 1 Hz. This requires a multilevel triggering system to record only the most interesting events . The CDF has a four level (0-3) triggering system [42] in which each level reduces the event rate sufficiently to allow a more detailed examination of the interesting events by the next level.

2.4.1 Level 0 trigger

The Level 0 trigger uses information from the beam beam counters (BBC). The BBC are a set of scintillators placed around the beam pipe in front of the forward detectors, about 6 metres from the detector vertex. They cover the region $3.24 < |\eta| < 5.89$. The level 0 trigger required that at least 3 of the counters on each side of the detector be fired and that the timing of these hits be consistent with the bunch crossing. Almost all inelastic collisions will satisfy this requirement and the decision time is small compared to the $3.5\mu s$ between crossings. The event rate at a typical luminosity of $10^{30}\,cm^{-2}\,sec^{-1}$ is

approx 50 KHz.

2.4.2 Level 1 trigger

The level 1 trigger uses calorimeter information. The front end calorimeter electronics contains two outputs. There is a fast analogue output used by the trigger in order to make fast decisions. There is also an output which is digitized by the data acquisition system (DAQ) and allows full charge integration. The analogue signals are summed to form trigger towers which are $.2 \times 15^o$ in $\eta \times \phi$ throughout the calorimeter. There are separate sums for the electromagnetic and hadronic calorimeters. The signals are normalized to be 1V for every 100 GeV. They are then each tested to see if they are above a programmed threshold and the towers that pass are summed over the entire detector and compared to a second programmable threshold. The trigger used in this analysis required 1 GeV single tower threshold and $\sum E_T \geq 18$ GeV. The Level 1 decisions takes 7 μs which means that 1 bunch crossing is missed and leads to a 17.5 % dead time. The typical event rate at a $10^{30}\, cm^{-2}\, sec^{-1}$ luminosity is 5 KHz.

2.4.3 Level 2 trigger

The level 2 trigger is implemented by fixed ECL circuitry. It searches for calorimeter clusters and matches these clusters to tracking and muon information. At this level specific physics signatures involving jets, electrons, muons etc. can be required. The sequence begins with cluster finding which uses a simple adjacency algorithm. Towers which pass a seed or cluster threshold are then identified and an ordered list of seed towers is made. The clustering begins by finding all towers adjacent to the seed which pass the cluster threshold. Towers which are adjacent to these towers and pass the cluster threshold are then added to the cluster and the process continues until there are no more adjacent towers. The E_T, E_x, E_y, $E_T\,\eta$, and $E_T\,\eta^2$ are calculated for the cluster. The ϕ of the cluster is compared with the track list from the fast tracker which

has compiled the P_T, ϕ for CTC tracks, in order to match tracks to clusters. If there are more seeds the clustering process continues until a complete list of clusters is formed.

In the 1989 run there were several different types of clusters. General purpose clusters with a seed and cluster threshold of 3.0 GeV, 1.0 GeV respectively were formed along with electron clusters with 4.0 GeV, 3.6 GeV thresholds. Also a pseudo-cluster was formed by summing all towers with $E_T > 1.0$ GeV in the detector to form the $\sum E_T$ and $\not{E}_T$. Trigger decisions are then made on quantities using a variety of algorithms. The entire process takes 30-40 μs and reduces the event rate from 5 KHz to 5 Hz. In this thesis a $\not{E}_T$ trigger was used and this will be discussed in section 3.3.

2.4.4 Level 3 trigger

The final and most sophisticated trigger decisions are made at level 3 by a set of micro-processors which run fortran algorithms to select events. The microprocessors are ACP nodes which are a set of Motorola 68020 processors using the VME protocol. At this level the DAQ calorimeter readout is available and so the offline calorimetry code is run with the most up to date constants. The event rate is reduced from 5 Hz to 1 Hz.

2.5 Front end electronics and detector readout

There are nearly 100,000 channels in the CDF which are readout by the front end electronics. The design requirements of the system were that it have a large dynamic range of 100,000:1, be stable and accurate to 1 %, have very little noise pickup, and be fast and reliable. To minimize the noise, all analogue signals except for the trigger fast outs are digitized on the detector before being sent to the counting rooms which are above the detector. The calorimeters

use a before and after sampling in which two storage capacitors sample the amplified signal before and after beam crossing. The difference between the two measures the signal size and removes the effects of charge build up between two events. This is implemented by the RABBIT [43] electronics system which handles the front end amplification, sampling, digitization, multiplexing, pedestal subtraction and calibration. RABBIT is an acronym for Redundant Analogue Bus Based Information Transfer system and the RABBIT crates are readout by MX scanners which are in the counting rooms. The redundancy is due to the fact that the electronics is mounted on the detector and is inaccessible most of the time and so to ensure reliability back-up circuits are needed. The signals from the tracking systems are shaped at the detector and sent to FASTBUS TDC's in the counting room which are read out by SSP scanners. The signals from both calorimeter and tracking systems are digitized and read out when the Level 2 trigger is passed. Each scanner can buffer 4 events.

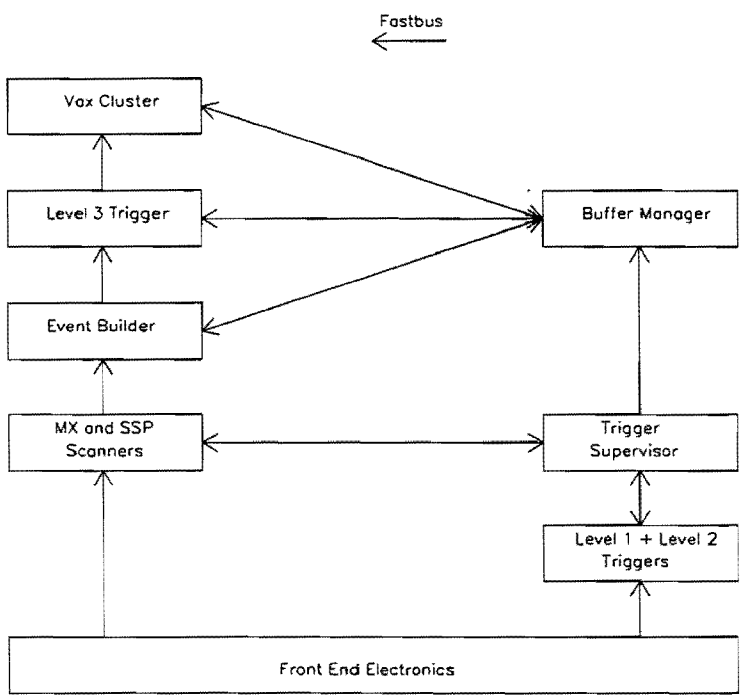

Figure 2-8: A schematic of the CDF FASTBUS based DAQ system.

The data acquisition system, based on the FASTBUS [44] protocol , is shown schematically in figure 2-8. The FASTBUS system was chosen because of its ability to deal with large parallel data transfer at high speed. The Buffer Manager, a microvax computer, controls the flow of data through the DAQ system. The Event builder, a dedicated processor, collects the event information from the various scanners and formats the data for use by the Level 3 trigger. From the Level 3 trigger the event is passed to host VAX computers and written to tape.

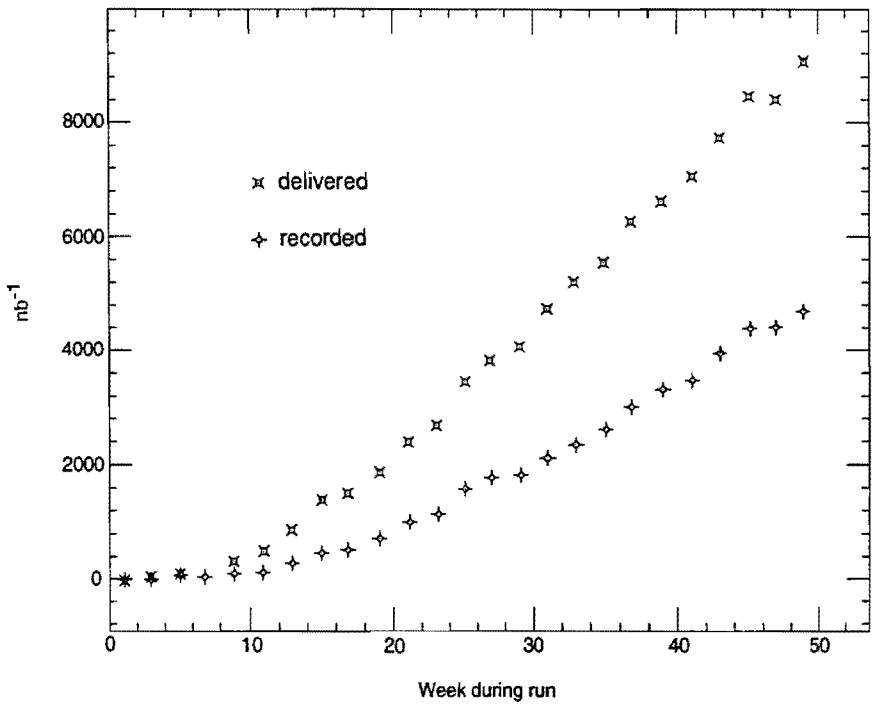

Figure 2-9: The integrated luminosity delivered compared to the integrated luminosity collected.

2.6 1988-1989 run

The data used in this thesis was collected over a 10 month period from August 1988 to May 1989. During this period the peak luminosity was over

$2 \times 10^{30}\, cm^{-2}\, sec^{-1}$ and the total integrated luminosity was $4.1 pb^{-1}$. 4×10^{6} events were recorded on 5500 magnetic tapes. Figure 2-9 shows the integrated luminosity delivered by the accelerator as compared to the integrated luminosity collected by the detector as a function of time.

Chapter 3

Event Reconstruction and Selection

In this chapter we first describe the conversion of raw data to energy and tracks. This is followed by a discussion of the experimental top to Charged Higgs signature since this motivates the particular physics objects we wish to reconstruct. This signature involves $\not{E}_T$, hadronic taus and jets. We use a hardware $\not{E}_T$ trigger to collect the data used for this search. This constitutes the most serious inefficiency in the selection requirements and so we discuss in some detail the trigger definition and the estimation of its efficiency. At the offline level the critical element of the analysis is the definition of a hadronic tau algorithm. This is a difficult problem at a $p\bar{p}$ experiment because jets can fluctuate to fake any hadronic tau signature that we define. We show that it is possible to define a hadronic tau signature that gives significant but finite rejection of jets. The QCD multijet cross section is several orders of magnitude higher than the predicted top cross section. This means that we must exploit the particular event topology characteristics of the top to Charged Higgs events to reject as much of the QCD cross section as possible before applying the hadronic tau algorithm. We show that with the correct event topology cuts and hadronic tau algorithm we are sensitive to top to Higgs events. We are also able to demonstrate the existence of a $W \rightarrow \tau\nu$ signature using our hadronic

tau algorithm and use this as a consistency check of our techniques.

3.1 Event reconstruction

In this thesis we used full production data sets. Production refers to the process of converting the raw data to energy and momentum quantities and also to physics objects such as jets and electrons. Variations in the electronic gain and pedestals are corrected online so that conversion of the calorimeter ADC counts to energy requires multiplication by a scale factor. The TDC counts in the tracking chambers are converted to drift times in the production process, which then allows the reconstruction of tracks. The VTPC tracks can then be used to reconstruct the event vertex.

3.1.1 Vertex reconstruction

The event vertex is reconstructed using VTPC tracks extrapolated to the beam axis. There is a small probability of multiple interactions. This is dependent on the luminosity and for a typical luminosity of $1.0 \times 10^{30}\ cm^{-2}\ sec^{-1}$ approximately 8 % of events contain a multiple interaction. This does not present a problem because in almost all cases the second interaction is a minimum bias event and does not affect the event variables we use in the analysis. The only impact is in the choice of primary vertex. We designate the primary vertex as the one with the most hits associated with it (i.e the sum of the hits on each track associated with the vertex) . The event vertex has an approximate Gaussian distribution with σ=30 cm due to the finite size of the proton and antiproton bunches . The event vertex is needed to reconstruct the transverse energy in the calorimeter and derived quantities such as $\not{E}_T$. Also we wish to require that tracks come from the primary vertex.

3.1.2 Energy reconstruction

The ADC data are converted to energies by multiplying by a detector dependent factor. This scale factor is deduced from testbeam data and from run dependent conditions such as gas gain which is affected by temperature and pressure. Bad channels are removed. Events with readout errors are flagged. Small pedestal drift corrections are applied to some channels. Some towers have anode planes which were turned off due to broken wires and the energy in these towers is corrected. After these tasks are accomplished we have an $\eta - \phi$ array of tower energies. Several types of noise are then removed before further processing.

In the central calorimeters the phototubes can give a spurious energy measurement. This may be due to high voltage breakdown in the phototube, or Cerenkov light from particles showering in the light guide. However, since each tower is read out by two phototubes, we can require energy in both to eliminate this problem.

The main ring passes over the top of the CDF detector. When particles in the main ring interact with the beam pipe a shower of particles through the detector can result. This can cause false calorimeter triggers. During data taking triggers were inhibited when main ring bunches passed over the detector but a few events still remained and necessitate offline filtering. The algorithm to do this is based on the observation that these events will have a large amount of out of time energy deposited. An event is rejected if more than 8 GeV of energy is deposited in CHA or WHA towers whose TDC hit time was more than 20 ns outside of the nominal beam crossing time. Less than 1 % of events are removed since the trigger inhibition is very effective.

Cable noise in the PHA and FHA is caused by pickup from the ground loops in the ribbon cables that connect the towers to the front end electronics. This is removed offline by recognizing that each cable carries signals from 12 adjacent towers. A uniform signal in 12 adjacent towers with no corresponding anode signal is indicative of pickup.

In the gas calorimeters the low energy neutrons produced by hadronic showers can cause knock on of protons from the ethane gas or plastic walls of the calorimeter. The protons are highly ionizing and loose all their energy in the gas in a very short distance. This effect is identified by an algorithm which looks for a large energy deposit in a very localized region. In addition localized large energy deposits can be caused by high voltage leakage from the ends of the PEM proportional tubes.

The array of tower energies can now be used to construct an array of transverse energies using the relation

$$E_T^i = E^i.\sin\theta^i$$

where E^i is the energy is the tower and θ^i is the angle between the event vertex and center of the tower. From this we can reconstruct the global energy quantities such as $\sum E_T$ and $\not{E}_T$

3.1.3 Track reconstruction

There first task in converting the raw TDC data to drift times is to correct the times for a number of systematic effects. To convert these times to tracks then involves pattern recognition of the hits associated with a track, followed by fitting the hits to a curve in order to measure the momentum.

The drift times must first be corrected for channel and time dependent fluctuations. There are variations due to the different cable lengths which are estimated using pulser calibrations. There are channel dependent variations due the difference between calibration and chamber pulses which are corrected using a large sample of tracks from minimum bias data. Additionally there are time dependent pedestal variations in delays in the electronic circuits which are again corrected using minimum bias data for each run. The drift velocity varies with position because of field distortions near the sense wires. Minimum bias data is used to measure the correction. After these corrections have been applied the tracks can now be reconstructed by the following procedure

An r-ϕ seed track segment is required in a cell in the outermost superlayer. This is defined by at least 5 hits from each wire plane with decreasing drift times (the hit closest to the wire gives the shortest drift time). Adjacent cells are searched until all the sense wires are tested and the segment is formed from these hits. A circle is then defined by these hits according to the expected trajectory of the track assuming it passes through the beam position.

- Hits are then searched for along this circle and the circle is refit using these hits. If the fit is too bad the hit is dropped else it is marked so that it not included in another seed track.
- Steps 1 and 2 are then repeated until there are no more r-ϕ seed tracks.
- The r-ϕ circle is projected onto the stereo layers and hits from these layers are used to construct the best z co-ordinate and thus the best three dimensional helical track fit.
- The above steps are repeated until there are no more track candidates.

At the end of this procedure we have an array of tracks associated with the primary vertex, and with accurate position and momentum measurements. Using the array of energies, the vertex, and the array of tracks we can now construct physics objects with which to search for the top to Higgs decay. We will now describe the experimental characteristics of this decay and the objects we construct.

3.2 Top to Higgs signature

At $\sqrt{(s)} = 1.8$ TeV the dominant production mechanism for top quarks is $t\bar{t}$ production [49]. We will first consider the case Br($t \rightarrow H^+b$)=1.0 and Br($H^+ \rightarrow \tau\nu_\tau$)=1.0 so that the final state is

$$\tau^+\nu_\tau\tau^-\bar{\nu_\tau}b\bar{b}$$

The b's will produce jets. The neutrinos are undetectable and therefore cause an imbalance of energy in the detector. The taus can decay to electrons,muons or hadrons. We will require a final state that involves a hadronic tau decay since we will be sensitive to a large fraction of the branching ratio ($B(\tau \rightarrow$ hadrons)=64 %). The final state signature is at least one hadronic taus plus at least one jet jet plus an energy imbalance. In designing the event selection criteria the first consideration is the trigger requirements. The trigger must be designed to give good efficiency for the signal while rejecting as much of the background as possible. The largest background to this signal is a multijet event in which one of the jets is mismeasured so that there is an energy imbalance and another fluctuates to look like a hadronic tau. Although this is a low probability event the jet cross-section at $\sqrt{s} = 1.8$ TeV is approximately 10^6 pb for events with a jet of $E_T > 15$ GeV, while the $t\bar{t}$ cross-section for m_t=70 GeV is of the order 10^2 pb. As we will show later, it is typically possible to construct an algorithm using the production quantities (rather than trigger quantities) that will reject 90 % of jets while accepting 50 % of taus. This type of algorithm uses full tracking quantities that are not available at the trigger level. It follows that an inclusive hadronic tau trigger would be dominated by background, and similarly for any trigger involving b jets. However, we can achieve large background rejection and good signal efficiency by considering the energy imbalance. This we will define by using the missing transverse energy ($\not{E}_T$).

3.2.1 Other possible signatures

As an aside, we note that we might consider alternative signatures involving an electron and/or a muon in the same fashion as the standard model top search. This possibility arises because the tau can decay to an electron or a muon. However, in the case of the standard model top, the lepton derives from a $W^{\pm}$ decay and so has a high P_T. In the charged Higgs case the lepton has much lower P_T. This is because there are two neutrinos in the leptonic tau

decay and tau itself derives from the charged Higgs (we are considering the case ($m_{H^+} < m_{W^+}$). In the 1988-89 run the lepton trigger thresholds were set too high to make these signatures possible with an inclusive lepton data set. Also we note that we would be much less sensitive to the total $t\bar{t}$ branching ratio. In the case of an $e\mu$ signature we would be sensitive to only 9 % of the branching ratio. Requiring at least one hadronic tau is sensitive to 87 % of the to $t\bar{t}$ branching ratio.

3.3 Missing transverse energy trigger

3.3.1 Description of the trigger

Missing transverse energy is defined by

$$\not{E}_T = \sqrt{\left(\sum_{\text{towers}} E_T \cdot \sin\phi_{\text{tower}}\right)^2 + \left(\sum_{\text{towers}} E_T \cdot \cos\phi_{\text{tower}}\right)^2}$$

with

$$E_T = E \times \sin(\theta)$$

Missing transverse energy is used rather than energy imbalance because there is energy loss along the beam pipe. The $\not{E}_T$ that we will use in the trigger is different than the production (DAQ) $\not{E}_T$ and this will later affect our trigger efficiency calculation. The trigger towers are different from the DAQ towers. They are segmented into units $|\Delta\eta| = .2$ rather than the DAQ towers $|\Delta\eta| = .1$. The E_T of the trigger towers is computed using the detector vertex rather than the event vertex used by the DAQ towers. The trigger towers are read out differently from the DAQ for reasons of speed. This means that there can be a difference between the trigger energy and DAQ energy due to fluctuations. Finally, the thresholds for inclusion of the towers into the trigger E_T sum and the offline DAQ sum are different. The combination of these differences means that the offline $\not{E}_T$ can be substantially different from the trigger $\not{E}_T$ and gives rise to a slow trigger turn on. The $\not{E}_T$ trigger is defined by the following requirements

- $\not{E}_T > 25$ GeV (with a 1 GeV tower threshold).

- The leading cluster be in the pseudorapidity range, $|\eta|$ ¡ 2.4 and must have at least 8 GeV of EM energy (E_{T1}^{em}). The trigger cluster is defined by a simple adjacency algorithm with a seed threshold of 3.0 GeV and 1.0 GeV shoulder threshold.

The electromagnetic energy requirement is added because the trigger was originally designed to select $W \rightarrow e\nu$ events. Since taus often contain a large fraction of electromagnetic energy from the π^0's in the hadronic decay this is not an overly restrictive requirement but does introduce a small inefficiency.

Figure 3-1 shows the $\not{E}_T$ for a $p\bar{p} \rightarrow t\bar{t} \rightarrow H^+H^-b\bar{b}$ Monte Carlo and for a sample of QCD jets taken from a jet trigger data stream. The generator Monte Carlo used is ISAJET (described in detail in section 4.2). The events are then passed through a detector simulation. The distributions of kinematic variables from the Monte Carlo changes with the mass of the top and the mass of the Higgs. We will use a top mass of 70 GeV and a Higgs mass of 50 GeV for illustrative purposes throughout this chapter. This choice is in the middle of the search region defined in chapter 1. In the actual computation of efficiencies we will use a different Monte Carlo data set for each m_{H^+}, m_t combination within our search region. The jet data set comes from a trigger requiring at least one calorimeter cluster with $E_T > 20$ GeV anywhere in the detector (JET20 trigger). We choose this data set because the jets in the top to Higgs events are typically in this range. The figure also shows the $\not{E}_T > 25$ GeV cut in the trigger. The trigger was originally designed to observe $W \rightarrow e\nu$. The choice of a 25 GeV cut was motivated by the need to have high acceptance for $W \rightarrow e\nu$ events, which typically have a much higher $\not{E}_T$ than the top to Higgs events, and also by the need to reduce jet background. The trigger is not optimal for the top to Higgs events since the $\not{E}_T$ cut is too high but we still have a reasonable efficiency with this trigger. We next describe the estimation of the trigger efficiency.

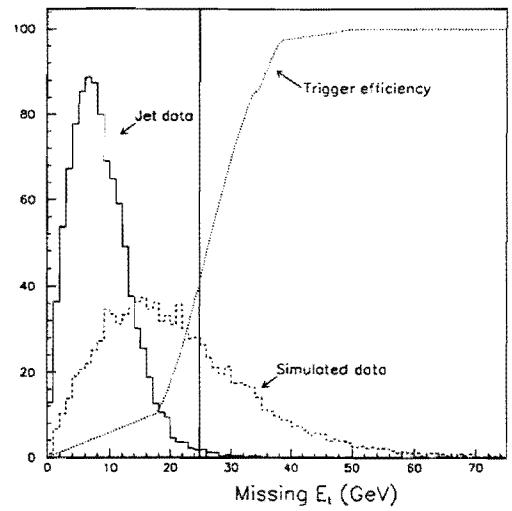

Figure 3-1: The $\not{E}_T$ for simulated (ISAJET) $p\bar{p} \rightarrow t\bar{t} \rightarrow H^+H^-b\bar{b}$, $H^\pm \rightarrow \tau\nu$ events (m_{H^+}=50 GeV, m_t=70 GeV) and for jets from a jet trigger data set. The jet data set is formed by requiring a jet cluster with $E_T > 20$ GeV. The normalization of the two distributions is arbitrary. Also shown is the $\not{E}_T$ trigger efficiency.

3.3.2 Estimation of trigger efficiency

In order to calculate the efficiency of this trigger we will use two techniques. We will first use data from an independent trigger and then compare this to an estimation from a Monte Carlo trigger simulation. In all of the Monte Carlo data sets used for estimating signal and background the leading cluster is almost always in the central or plug calorimeters (98%-99%) and so the trigger efficiency needed is a function of two variables $\not{E}_T$ and E_{T1}^{em}

$$\epsilon = f(\not{E}_T).g(E_{T1}^{em})$$

$f(\not{E}_T)$ is the trigger efficiency as a function of $\not{E}_T$ independent of E_{T1}^{em} and vice-versa for $g(E_{T1}^{em})$. To measure the trigger efficiency we use data from another trigger which is independent of the trigger requirement we are trying to measure. We therefore require a data set that has been defined without making

any $\not{E}_T$ requirement yet has substantial $\not{E}_T$. Examples of this are an inclusive electron data set in which there are $W \rightarrow e\nu$ candidate events, and a jet data set in which there are a small number of high $\not{E}_T$ events due to jet mismeasurement or resolution fluctuation. We will use both data sets to compute the efficiency of the $\not{E}_T$ trigger requirement, since the top to charged Higgs events contain both electromagnetic and hadronic energy. The inclusive electron data set trigger requires that there be a central electron trigger cluster with $E_T > 12$ GeV and a track associated with the cluster with $P_T > 6$ GeV. Additionally we require a good isolated central electron with $E_T > 20$ GeV using the electron quality cuts described in appendix A. The data set then contains a significant number of $W \rightarrow e\nu$ events which have substantial $\not{E}_T$. In all the data sets there is a data bank in which the trigger quantities have been stored. In this data set, for a particular value of reconstructed offline $\not{E}_T$, we ask whether the trigger $\not{E}_T$ is greater than 25 GeV. Since we have only a finite number of statistics we must bin the data according to offline $\not{E}_T$. The appropriate bin width is chosen by considering that the $\not{E}_T$ resolution is given in terms of the total scalar $\sum E_T$ by

$$\sigma_{\not{E}_T} = 0.47\sqrt{\sum E_T}$$

This estimation comes from figure 3-9 and the $\not{E}_T$ resolution is discussed in section 3.4.2. Using the measured scalar $\sum E_T$ we find that the typical resolution is 4 GeV and so we use this as the bin width. Figure 3-2 shows typical efficiency computed with the inclusive electron data set. Also shown is the efficiency computed with data from a trigger that required a trigger cluster of at least 60 GeV in the calorimeter. There are very few events with high missing transverse energy and hence there are large errors for these bins. Similar curves are obtained for jet triggers with 20 and 40 GeV, but there are even fewer high $\not{E}_T$ events and so we gain very little by using these in our calculation.

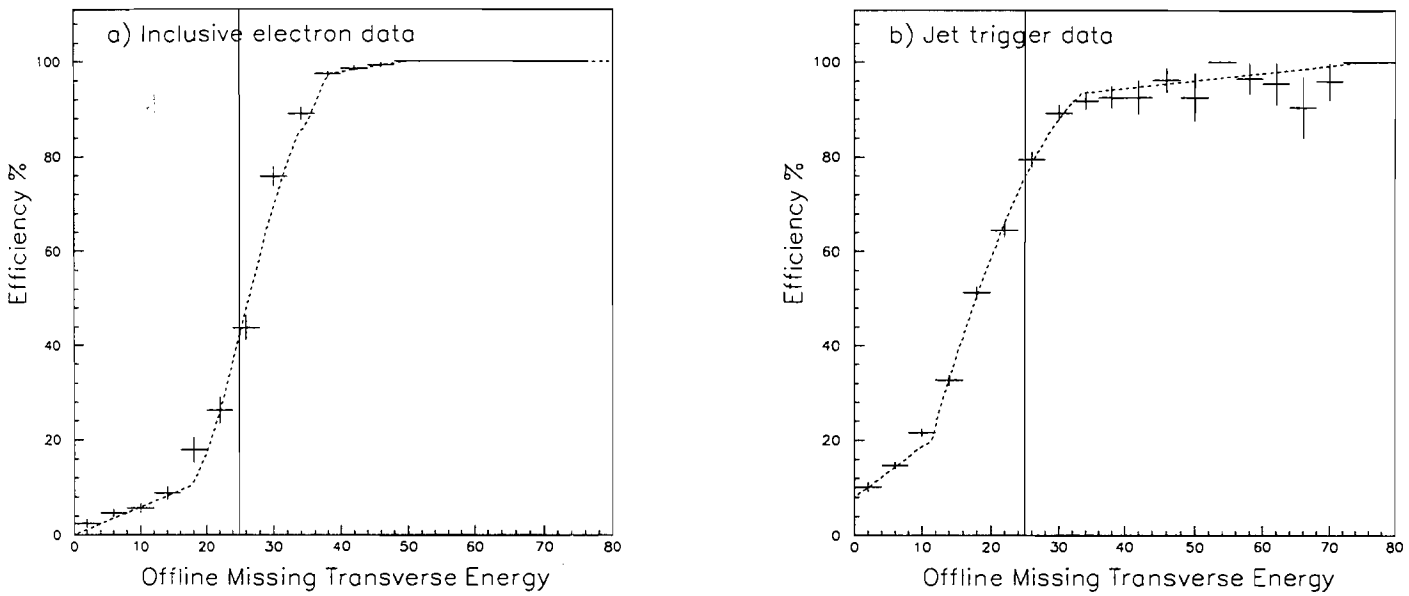

Figure 3-2: The $\not\!\!E_T$ trigger efficiency from data. The two plots are from a) an inclusive electron data set which required a 12 GeV electromagnetic trigger cluster b) a jet data set which required a 60 GeV trigger cluster.

The agreement between the jet data and the electron data is quite good in the relevant region ($\not\!\!E_T > 25$ GeV) but the jet data shows an earlier turn on that the electron data. This is because the EM trigger energy is only 93 % of the offline EM trigger energy while the hadronic trigger and offline energy is equal [57]. We do not attempt to explain the efficiency curves for low $\not\!\!E_T$ since we make a cut of $\not\!\!E_T > 25$ GeV. The efficiency points are fit to parameterized curves which we will subsequently convolute into our Monte Carlo calculations as explained later. The $\not\!\!E_T$ requirement is approximately 50 % efficient at the threshold cut of 25 GeV and achieves > 95 % efficiency above 40 GeV. If these efficiency curves are compared to the typical $\not\!\!E_T$ distribution for top to Higgs events in figure 3-1 then it can be seen that the slow turn on will have a significant impact on the acceptance calculation.

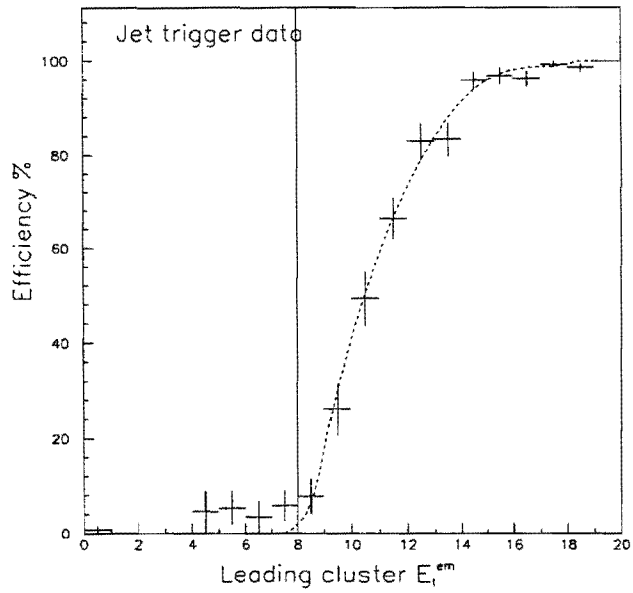

Figure 3-3: The trigger efficiency for the electromagnetic cluster requirement of the $\not{E}_T$ trigger ($E_{T1}^{em} > 8$ GeV, $|\eta| < 2.4$) computed from a jet data data set which required a trigger cluster with $E_T > 60$ GeV. Only non-trigger clusters were used to avoid bias.

In addition to the $\not{E}_T$ requirement the $\not{E}_T$ trigger also requires an electromagnetic cluster of at least 8 GeV in the pseudorapidity range $|\eta| < 2.4$. We now estimate the efficiency of this requirement , $g(E_{T1}^{em})$. In our top to Higgs Monte Carlo this requirement is most often satisfied by a π^0 from the taus or jets in the event, rather than by an electron. We therefore use the jet data set which required a cluster of $E_T > 60$ GeV to compute the efficiency since the electromagnetic energy in the clusters in these events is most often from a π^0. We then compare the trigger electromagnetic energy in the next to leading trigger cluster with the associated reconstructed offline cluster. We use the next to leading cluster rather than the leading cluster, which is the trigger cluster, to avoid any bias. We use only clusters in the pseudorapidity range $|\eta| < 2.4$. Figure 3-3 shows the efficiency estimated. At 8 GeV the trigger requirement is very inefficient, but quickly rises to 50 % at 10.5 GeV and achieves better

than 95 % at greater than 13 GeV.

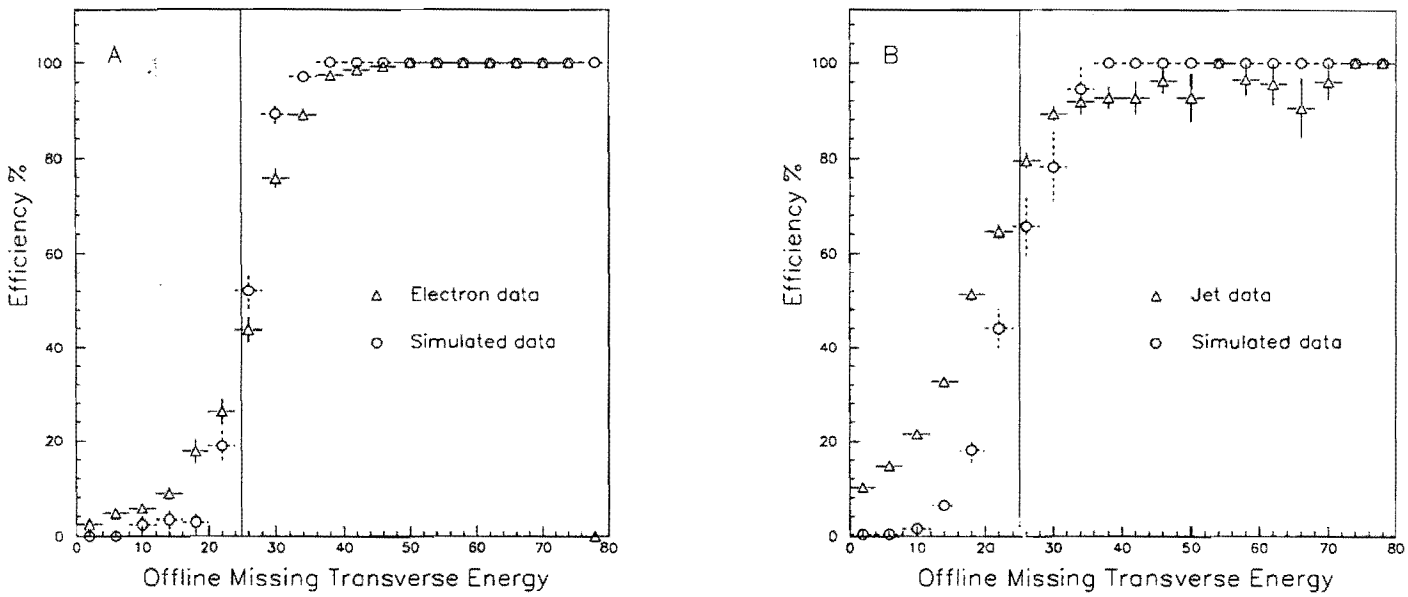

Figure 3-4: The $\not{E}_T$ trigger efficiency calculated with simulated data and compared to electron and jet data. The simulation is ISAJET followed by a detector and trigger simulation. The electron data required a trigger cluster with electromagnetic energy $E_T > 12$ GeV. The jet data set required a trigger cluster with $E_T > 60$ GeV

To gain further confidence in our efficiency calculation we compare the efficiency curves from data to simulated data sets. We use the ISAJET generator Monte Carlo in conjunction with a detector simulation [54] and a level 1 and level 2 trigger simulation [53]. In figure 3-4 we compare simulated $W \rightarrow e\nu$ data with the electron data set described above, and also simulated jet data with the jet data set for the $\not{E}_T$ efficiency. The $W \rightarrow e\nu$ simulation gives a very good agreement, while the jet simulation is reasonable in the region of interest ($\not{E}_T > 25$ GeV). In figure 3-2 also use the simulated jet data to compare to the E_{T1}^{em} efficiency curve.

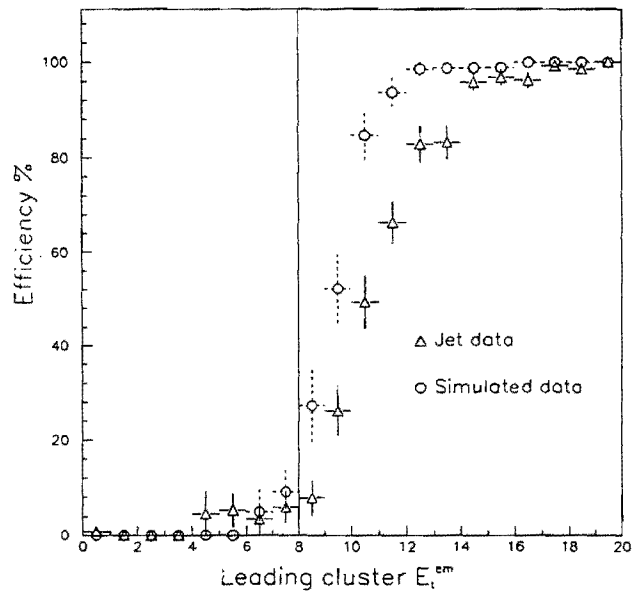

Figure 3-5: The E_{T1}^{em} trigger efficiency from simulation data compared to jet data. The simulated data is ISAJET followed by a detector and trigger simulation. The jet data required a trigger cluster with $E_T > 60$ GeV.

We have computed the trigger efficiency curves in three different ways, with $W \rightarrow e\nu$ data, with jet data and with simulated data. The motivation for using both electron and jet data was that top to charged Higgs events would in general contain both electromagnetic and hadronic energy. The efficiencies are slightly different for both the $W \rightarrow e\nu$ and jet cases due to the differing relationship between the reconstructed offline energy and the trigger energy for electromagnetic and hadronic energy. The simulation gave reasonable, but not perfect agreement with these two cases. The most conservative way to calculate the trigger efficiency for top to Higgs events from these studies is to separately use the efficiency curves from each of the three calculations as below. The efficiency is taken as the average of the three calculations and the systematic error as the maximum deviation of any one of the calculations from the average.

- 1. Convoluting $\epsilon = f(\not{E}_T).g(E_{T1}^{em})$ into the Monte Carlo data where f is computed from electron data and g for jet data (ϵ_1)
- 2. Convoluting $\epsilon = f(\not{E}_T).g(E_{T1}^{em})$ into the Monte Carlo data where f is computed from jet data and g from jet data (ϵ_2)
- 3. Using trigger simulation (ϵ_3)

Then the efficiency(ϵ) and error on the efficiency (σ_ϵ) are defined as below

$$\epsilon = \frac{\epsilon_1+\epsilon_2+\epsilon_3}{3}$$

$$\sigma_\epsilon = max(\epsilon_1 - \epsilon, \epsilon_2 - \epsilon, \epsilon_3 - \epsilon)$$

The trigger efficiency varies with m_{H^+}, m_t, because the $\not{E}_T$ derives from the neutrino in the Higgs decay. As the Higgs mass changes so will the average P_T of the neutrino. The trigger efficiency varies from 18-25 % over the range of Higgs masses we are investigating. In the typical case of, m_{H^+} = 50 GeV, m_t =70 GeV, the efficiency is 23 % and the systematic error is 2 %. The trigger is the largest inefficiency of the various cuts used in this analysis. We note that the trigger was not explicitly designed for the selection of top to Higgs events. The electromagnetic cluster requirement constitutes about 10-15 % of this inefficiency. This was originally added to reduce noise when trying to trigger on $W \rightarrow e\nu$ events, and should be removed if one were trying to create an optimum top to Higgs trigger. Additionally, the $\not{E}_T$ trigger threshold of 25 GeV is too high as can be seen from figure 3-1 and so one would also like to lower this threshold. However, as the threshold is lowered the background from QCD events also increases and so one should couple the lowering of the $\not{E}_T$ threshold with some form of loose tau requirement (eg. a narrow jet).

There is also a level 3 $\not{E}_T$ trigger but the quantities used by this trigger are the reconstructed offline quantities and all the cuts applied are superseded by cuts used in the definition of the data stream which will now be described.

3.4 Data stream selection

After offline reconstruction the $\not\!\!E_T$ trigger data was filtered. In this filter we endeavour to reduce the QCD multijet background while maintaining high acceptance for top to Higgs events. To do this we exploit the different event topologies of the two classes of events. Explicitly we reinforce the $\not\!\!E_T$ trigger requirement with an offline $\not\!\!E_T$ cut and require that the $\not\!\!E_T$ is significant. We also remove events with a dijet topology. We first describe the definition of a jet at the CDF before defining these selection requirements in detail.

3.4.1 Jet clustering algorithm

The jet clustering algorithm [54] starts with the $\eta - \phi$ array of transverse energies and uses a fixed cone clustering algorithm. A jet centroid is found and all towers within a fixed cone are summed. This algorithm is chosen because it most closely corresponds to the theoretical definition of jets and is free of the clustering problems associated with unusual event topologies. There are three steps

- Two lists are formed from the $\eta - \phi$ array of transverse energies. The seed list includes all towers with $E_T > 3$ GeV and the candidate list contains all towers with $E_T > 1$ GeV. Preclusters are formed. These are unbroken strings of adjacent towers with continuously decreasing E_T as you move away from the seed. Plug and forward towers are summed in ϕ so that the segmentation is the same as the central.

- A cone of $R=\sqrt{\Delta\eta^2 + \Delta\phi^2}=0.7$ is formed about E_T weighted centroid of the precluster. Candidate towers inside the cluster are added to this cluster. The centroid is recomputed and the process is repeated until the cone is stable.

- There are some cases where towers belong to two clusters. If one cluster includes another, the smaller is dropped. If the clusters are overlapping

then an overlap fraction is defined as the E_T shared by the clusters divided by the overlap between the clusters. If this fraction is greater than 0.75 the smaller cluster is merged by the larger one. If the fraction is less than 0.75 then each overlapping tower is associated with the cluster whose centroid is closer. The centroids are recalculated and the process is repeated until the cluster list is stable.

3.4.2 The data stream - event topology cuts

We use a $\not{E}_T$ data stream that was one of several defined data streams in the 1988-89 run. This is further augmented by some additional more stringent cuts. The cuts are summarized, with the efficiencies for top to HIggs events, in table 3.1. The are 250,000 events which pass the $\not{E}_T$ trigger and these cuts reduce the data set to 29,000 events.

The $\not{E}_T$ data stream

The defined $\not{E}_T$ data stream filter requires

- $\not{E}_T > 15$ GeV
- Dijet veto
- The highest E_T Jet cluster be $E_T > 15$ GeV, $|\eta| < 2.4$, $E_T(EM)/E_T(HAD) > 5\%$.

The offline $\not{E}_T$ is calculated with the event vertex. The dijet veto is applied by requiring that there be no cluster with $E_T > 10$ GeV azimuthally opposite the leading cluster $|\Delta\phi| > 150^0$. Figure 3-6 shows this azimuthal angle for simulated top to Higgs events and for a jet sample taken from a jet trigger data set. Table 3.1 shows that the dijet veto is the most severe cut. The data set is re-

duced to 129,000 events.

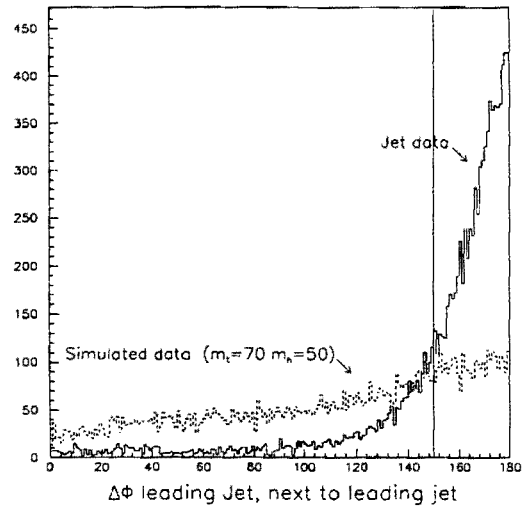

Figure 3-6: The azimulthal angle between the leading jet and next-to- leading jet for simulated (ISAJET) $p\bar{p} \rightarrow t\bar{t} \rightarrow H^+H^-b\bar{b}$, $H^\pm \rightarrow \tau\nu$ events (m_{H^+}=50 GeV, m_t=70 GeV) and for jet events from a data set which required a trigger cluster of $E_T > 20$ GeV. The normalization is arbitrary.

Additional event topology cuts

We make the following additional cuts

- $\not{E}_T > 25$ GeV
- $Z_{vertex} < 60$ cm
- $\not{E}_T/\sqrt{\sum E_T} > 2.5$

The more stringent $\not{E}_T$ cut is to complement the trigger cut of $\not{E}_T > 25$ GeV. Figure 3-7 shows the $\not{E}_T$ for the 129000 events and also for the simulated top to Higgs data.

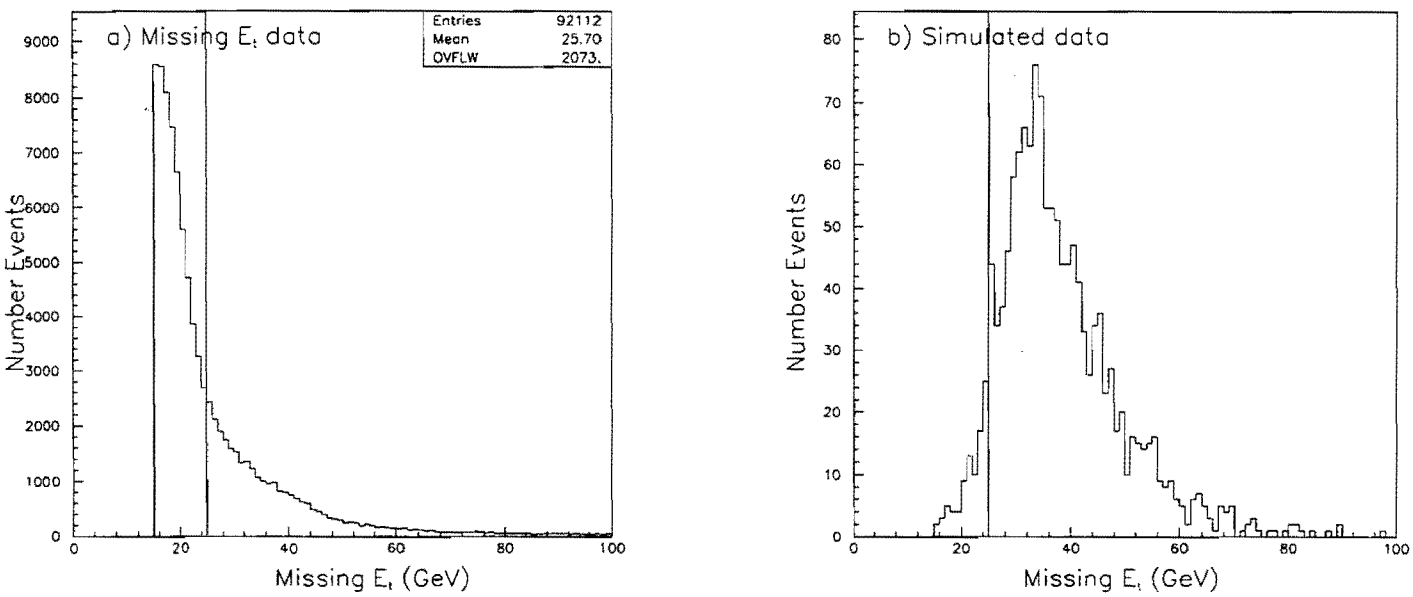

Figure 3-7: The $\not\!\!E_T$ for a) the $\not\!\!E_T$ data set after the trigger and $\not\!\!E_T$ filter and b) simulated (ISAJET) $p\bar{p} \rightarrow t\bar{t} \rightarrow H^+H^-b\bar{b}$, $H^\pm \rightarrow \tau\nu$ events (m_{H^+}=50 GeV, m_t=70 GeV) after the same cuts.

The Z_{vertex} cut is to remove a small class of events that have a large $\not\!\!E_T$ due to a highly displaced vertex in the z direction. The effect of the displacement is that jets pass through cracks in the detector, whereas if the vertex were at the center of the detector the jets would traverse at least part of the calorimeter due to the different angle of approach. These events are removed by requiring that $Z_{vertex} < 60.0$ cm. The vertex distributions for the $\not\!\!E_T$ data sample, and for simulated top to Higgs events are shown in figure 3-8. The mean in the data is offset slightly by a few centimeters due to incorrect tuning of the interaction point while taking data. Table 3.1 shows that the vertex cut and the $\not\!\!E_T$ cut cause only a small inefficiency and the $\not\!\!E_T$ data sample is reduced to 32000 events.

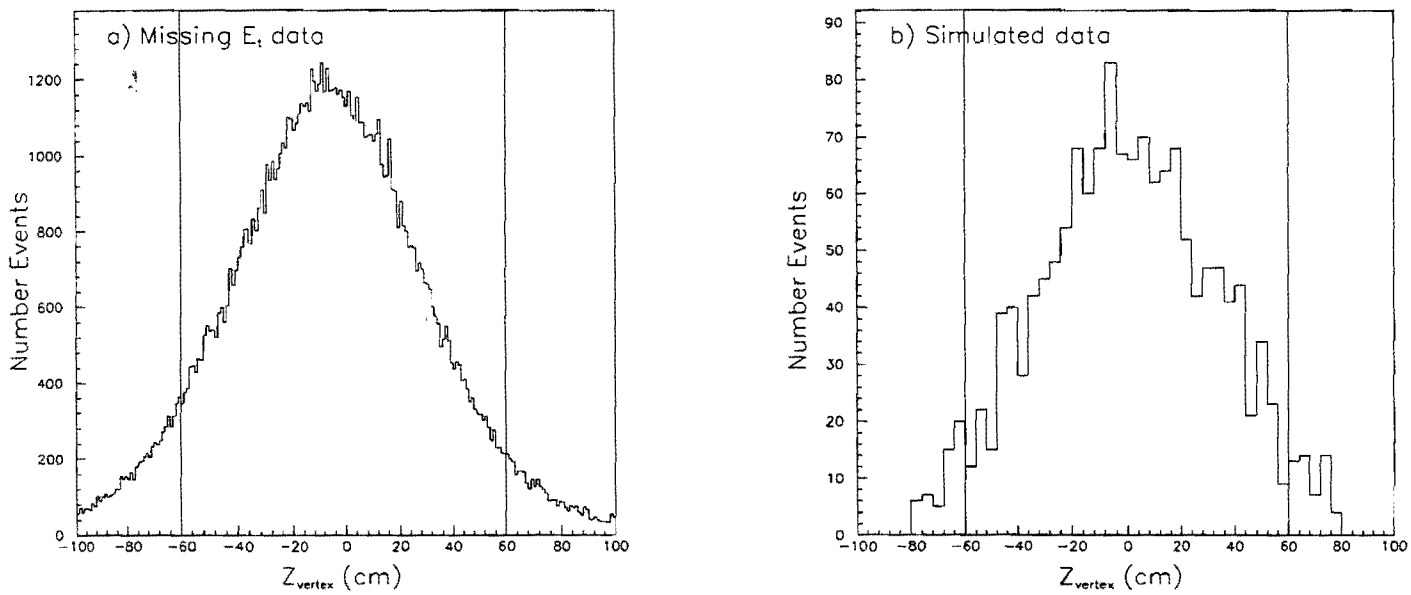

Figure 3-8: The Z_{vertex} for a) $\not{E}_T$ data set events after the trigger and $\not{E}_T$ filter cuts have been passed and b) for simulated (ISAJET) $p\bar{p} \rightarrow t\bar{t} \rightarrow H^+H^-b\bar{b}$, $H^\pm \rightarrow \tau\nu$ events (m_{H^+}=50 GeV, m_t=70 GeV) after the same cuts.

The significance cut ($\not{E}_T/\sqrt{\sum E_T} > 2.5$) is to further reduce the QCD background. In many QCD events that remain in the data set the $\not{E}_T$ is due to resolution fluctuations. The sampling fluctuations in the calorimeters cause the measured energy of a jet to differ from its true energy. This can result in spurious $\not{E}_T$ due to the imbalance of energy. Figure 3-9 shows a plot of the $\sigma_{\not{E}_x}/\sqrt{\sum E_T}$ versus $\sum E_T$ for minimum bias events in which one expects no true $\not{E}_T$. This illustrates that the probability of a fluctuation causing $\not{E}_T$ is proportional to $\sqrt{\sum E_T}$. To reduce the probability of the $\not{E}_T$ being due to fluctuations we require that the significance be greater than 2.5. This is 4 standard deviations away from the typical minimum bias significance. Figure 3-10 shows the significance distributions for both the data set and the simulated $t\bar{t}$ events. In the data set 29000 events remain after this cut.

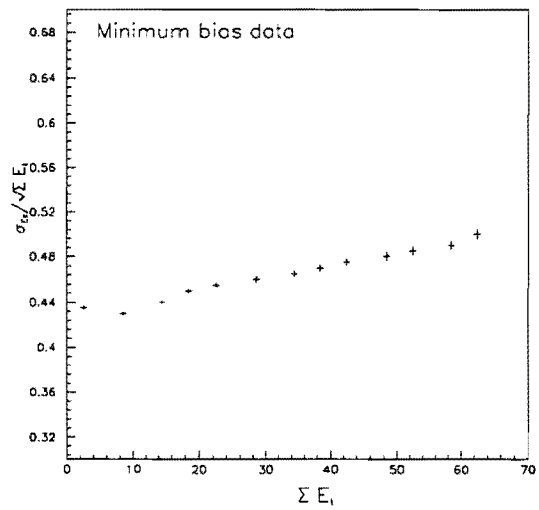

Figure 3-9: The dependence of $\sigma_{\not{E}_x}/(\sum E_T)^{1/2}$ on $\sum E_T$ in minimum bias events in which we expect no $\not{E}_T$. A straight line fit indicates that the slope is 0.47.

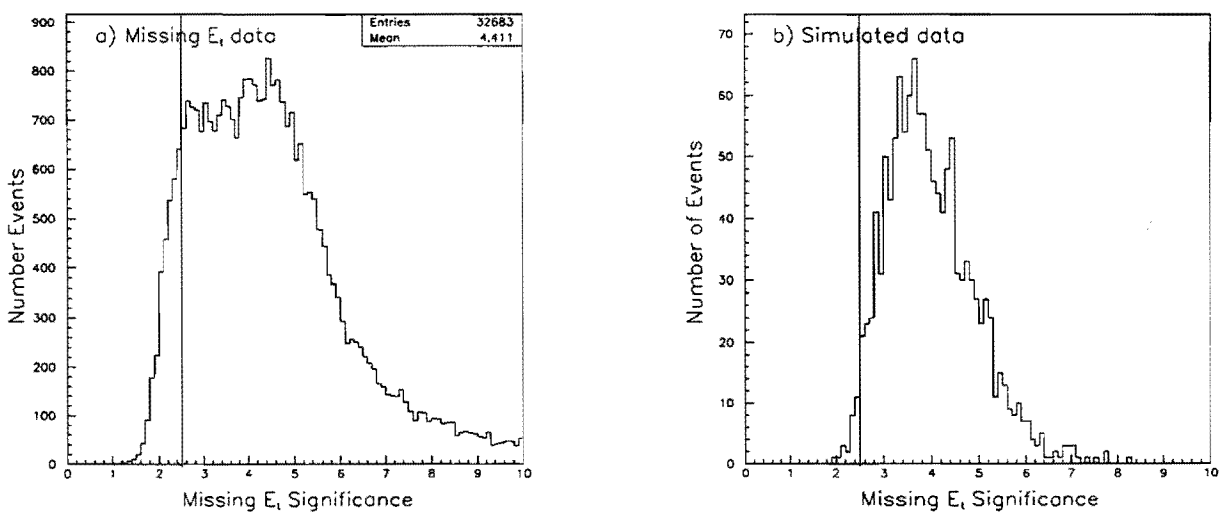

Figure 3-10: The missing transverse energy significance for a) the $\not{E}_T$ data set events, after the trigger, $\not{E}_T$ filter, Z_{vertex} and $\not{E}_T$ cuts, and b) simulated (ISAJET) $p\bar{p} \rightarrow t\bar{t} \rightarrow H^+H^-b\bar{b}$, $H^\pm \rightarrow \tau\nu$ events (m_{H^+}=50 GeV, m_t=70 GeV) after the same cuts

Description	Cut	Efficiency for $t \to H^+b$ events (m_{H^+} = 50 GeV, m_t = 70 GeV)
Trigger	$\not{E}_T > 25$ GeV Leading Cluster: EM > 8 GeV, $\|\eta\| < 2.4$	0.23
Defined $\not{E}_T$ Filter	$\not{E}_T > 15$ GeV	1.00
	Leading cluster: $E_T > 15$ GeV, $\|\eta\| < 2.4$ $E_T(EM)/E_T(HAD) > 5\%$	0.99
	Dijet veto: No cluster $E_T > 10$ GeV with $\Delta\phi > 150^o$ from leading cluster	0.68
Additional cuts	$\not{E}_T > 25$ GeV	0.93
	$Z_{vertex} < 60$ cm	0.94
	$\not{E}_T/\sqrt{\sum E_T} > 2.5$	0.98
Total		0.13

Table 3.1: A summary of the data stream selection cuts and the efficiencies for simulated (ISAJET) $p\bar{p} \to t\bar{t} \to H^+H^-b\bar{b}$, $H^\pm \to \tau\nu$ events (m_{H^+}=50 GeV, m_t=70 GeV) . The efficiencies are calculated sequentially. The total is the product.

3.5 Defining a hadronic tau algorithm

Decay Mode	CELLO Branching Ratio	World Average Branching Ratio
$\tau \rightarrow e\nu_\tau\nu_e$	$18.4 \pm .9\%$	$17.7 \pm .4\%$
$\tau \rightarrow \mu\nu_\tau\nu_\mu$	$17.7 \pm .9\%$	$17.8 \pm .4\%$
$\tau \rightarrow \pi\nu_\tau$	$11.1 \pm 1.0\%$	$11.0 \pm .5\%$
$\tau \rightarrow K\nu_\tau$	$.7 \pm .2\%$	$.68 \pm .19\%$
$\tau \rightarrow K^*\nu_\tau$	$1.4 \pm .3\%$	$1.6 \pm .2\%$
$\tau \rightarrow \rho\nu_\tau$	$22.2 \pm 1.7\%$	$22.7 \pm .8\%$
$\tau \rightarrow \pi\pi^0\pi^0\nu_\tau$	$10.0 \pm 1.9\%$	$7.5 \pm .9\%$
$\tau \rightarrow \pi\pi^0\pi^0\pi^0\nu_\tau$	$3.2 \pm 1.4\%$	$< 1.4\%$ (theory)
$\tau \rightarrow \pi\pi\pi\nu_\tau$	$8.7 \pm .8\%$	$7.1 \pm .6\%$
$\tau \rightarrow \pi\pi\pi\pi^0\nu_\tau$	$5.6 \pm .8\%$	$6.7 \pm .7\%$
$\tau \rightarrow$ other	$1.0 \pm .3\%$	$< .8\%$ (theory)

Table 3.2: Tau decay branching ratios

We will search for tau's that decay hadronically. The basic requirement of a hadronic tau algorithm is that it has a high efficiency for finding hadronic tau's. However, we must consider that jets can fragment to look like hadronic taus so that the algorithm must give a good rejection of jets. Also since a tau decay can have a low momentum track (π^+) pointing at a cluster with a large component of electromagnetic energy (π^0), this can be confused with an electron that has bremstrallunged. We therefore need to make sure that the algorithm also gives very good rejection of electrons. Finally we must consider the event environment of the tau. For example, a tau from a $W \rightarrow \tau\nu$ event will have a higher P_T and be more isolated that a tau from a $p\bar{p} \rightarrow t\bar{t} \rightarrow H^+H^-b\bar{b}, H^\pm \rightarrow \tau\nu$ event. The P_T is lower because we are considering the case $m_{H^+} < m_{W^+}$. The tau is more isolated because the only other final state particle in the $W \rightarrow \tau\nu$ event is a neutrino as opposed to a $t\bar{t}$ event in which we have other tau's and jets. These considerations affect the choice of P_T/E_T thresholds

and isolation variables. We begin the formulation of the algorithm by listing the distinctive properties of a hadronic tau decay.

- With the exception of the $\tau \rightarrow K\nu_\tau, \tau \rightarrow K^*\nu_\tau$ modes, which are only 2 % of the branching ratio, all the hadronic decay modes contain both neutral (π^0) and charged ($\pi^\pm$) energy and so will form a calorimeter cluster with both electromagnetic and hadronic energy.
- The number of charged tracks in the decay will be one or three.
- The tau has a low mass (1.78 GeV) compared to the typical boost that it receives in a $t\bar{t}$ event, which is approximately 20 GeV. The tau decay products will have a small momentum component transverse to the direction of the boost, compared to the momentum component parallel to the boost. Consequently the cluster will be narrow.
- The tau will often be isolated.

Our algorithm will be a calorimeter cluster with associated tracks and some form of isolation requirement. In addition we will define a cut to veto electrons. The algorithm, which we now describe in detail, is summarized in table 3.4 with efficiencies for taus from simulated (ISAJET) $p\bar{p} \rightarrow t\bar{t} \rightarrow H^+H^-b\bar{b}$, $H^\pm \rightarrow \tau\nu$ events (m_{H^+}=50 GeV, m_t=70 GeV) .

3.5.1 Hadronic tau cluster requirements

We require a cluster with

- Cone radius R=0.4
- $0.1 < |\eta| < 1.0$
- $E_T > 15$ GeV

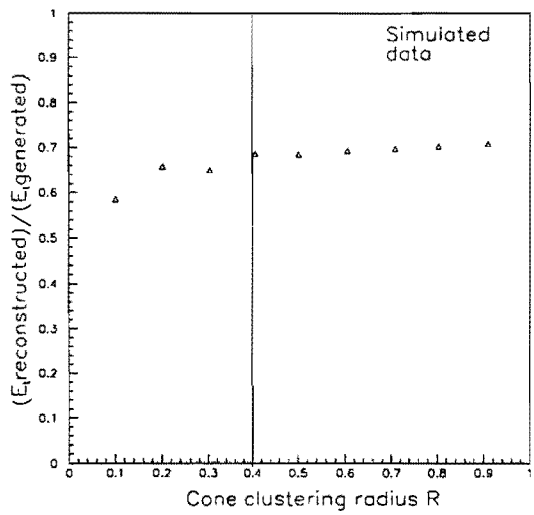

Figure 3-11: The reconstructed/generated energy for taus as a function of cone cluster radius. The taus are from simulated (ISAJET) $p\bar{p} \rightarrow t\bar{t} \rightarrow H^+H^-b\bar{b}$, $H^\pm \rightarrow \tau\nu$ events (m_{H^+}=50 GeV, m_t=70 GeV) .

The CDF jet clustering algorithm (described in section 3.4.1) has been used extensively at CDF and is well understood. We use this as the starting point in our tau algorithm. We set the cone radius to be 0.4. Figure 3-11 shows the fraction of energy reconstructed for taus versus the cone radius. It can be seen that we will accept most of the energy for a cone radius greater than R=0.2. However, we choose R=0.4 since this is also appropriate for jets in the event. This allows us to use previous work on systematic effects associated with the choice of this cone size. Choosing the cluster size to be 0.4 rather than 0.2 does not significantly affect the efficiency or background rejection power of the hadronic tau algorithm.

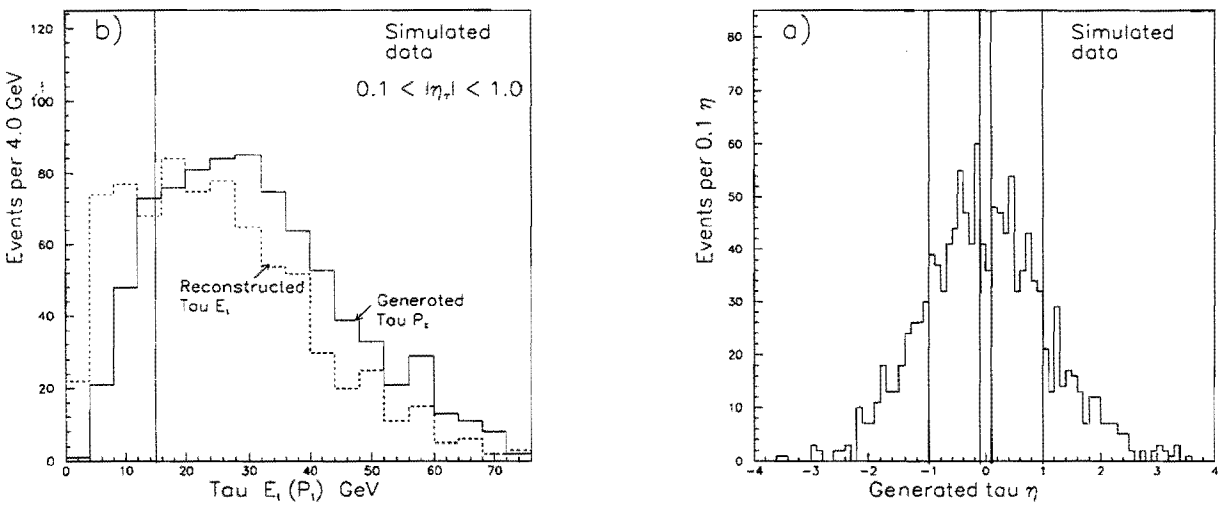

Figure 3-12: a) The generated η of taus in simulated (ISAJET) $p\bar{p} \rightarrow t\bar{t} \rightarrow H^+H^-b\bar{b}$, $H^\pm \rightarrow \tau\nu$ events (m_{H^+}=50 GeV, m_t=70 GeV) . b) The generated P_T and reconstructed E_T of taus with $0.1 < |\eta| < 1.0$. All events are required to pass the trigger and data stream requirements. Also shown are the selection cuts $0.1 < |\eta| < 1.0$, $E_T > 15$ GeV.

We require the cluster to be in the central region $0.1 < |\eta| < 1.0$. This is because we wish to associate tracks with the cluster. Tracks are reconstructed with high efficiency when they pass through all layers of the central tracking chamber. This defines the region $|\eta| < 1.0$. We exclude clusters in the region $0.1 < |\eta|$ because there is a crack in the detector at η =0.0. Figure 3-12 shows the η distribution of taus from simulated top to Higgs events. The taus are predominantly central because the $t\bar{t}$ system is produced predominantly in the central region. The acceptance of this cut, if we require at least one hadronic tau from simulated (ISAJET) $p\bar{p} \rightarrow t\bar{t} \rightarrow H^+H^-b\bar{b}$, $H^\pm \rightarrow \tau\nu$ events (m_{H^+}=50 GeV, m_t=70 GeV) is 66 %. We consider clusters with $E_T > 15$ GeV. Below this value the QCD background increases dramatically. Figure 3-12 shows the generated P_T and reconstructed E_T of taus in the region $0.1 < |\eta| < 1.0$ after trigger and data stream requirements. The reconstructed E_T is less than generated P_T because of the neutrino in the tau decay. The acceptance of this requirement for hadronic taus from simulated (ISAJET) $p\bar{p} \rightarrow t\bar{t} \rightarrow H^+H^-b\bar{b}$, $H^\pm \rightarrow \tau\nu$ events (m_{H^+}=50 GeV, m_t=70 GeV) is 65 %.

3.5.2 Hadronic tau track requirements

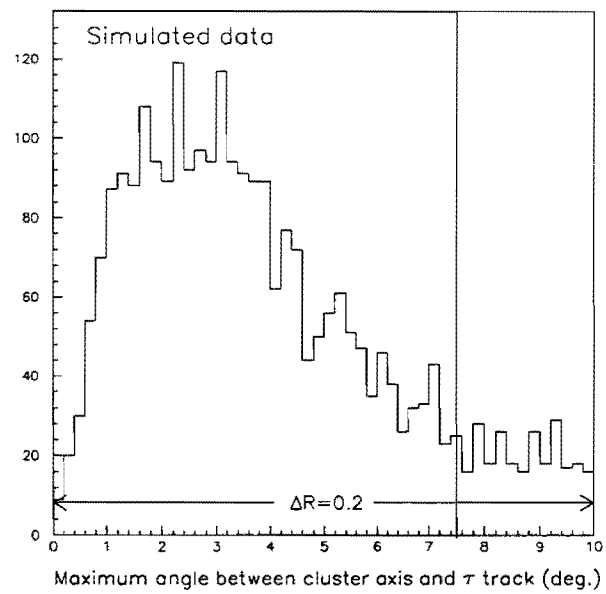

Figure 3-13: The maximum angle of tracks from tau cluster axis for taus in simulated (ISAJET) $p\bar{p} \rightarrow t\bar{t} \rightarrow H^+H^-b\bar{b}$, $H^\pm \rightarrow \tau\nu$ events (m_{H^+}=50 GeV, m_t=70 GeV) . Also shown is the equivalent cone radius R.

We require that the tau cluster have

- A least one track with $P_T > 2.5$ GeV in a cone of 7.5^o about the cluster axis.
- No tracks with $P_T > 1$ GeV in an annulus of 7.5^o-17.5^o about the cluster axis.

The cluster axis is defined as a vector that points from the event vertex to the E_T weighted centroid of the cluster. We then form cones about this axis in which we search for good tracks. The tracks are required to satisfy standard quality requirements [56] and to be associated with the primary vertex. Figure 3-13 shows the maximum angle from the axis of all tracks with $P_T > 1.0$ GeV resulting from the tau decay (recall that there can be 1 or 3 charged tracks). We search for tracks in a 7.5^o cone about the cluster axis.

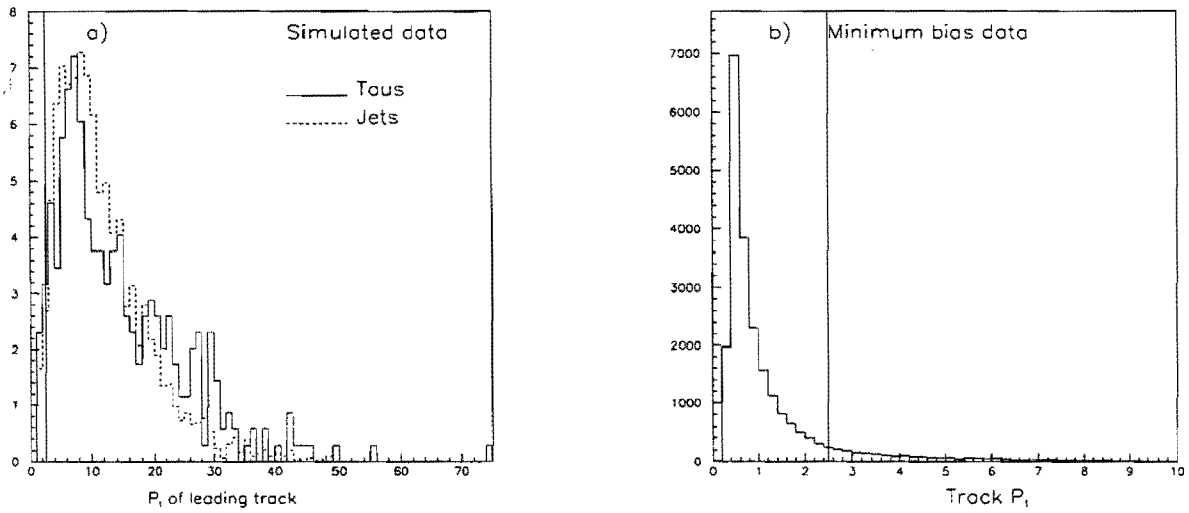

Figure 3-14: a) P_T of leading tau tracks for taus in simulated (ISAJET) $p\bar{p} \rightarrow t\bar{t} \rightarrow H^+H^-b\bar{b}$, $H^\pm \rightarrow \tau\nu$ events (m_{H^+}=50 GeV, m_t=70 GeV) . Also shown is the same distribution for jets from a jet data sample. b) The P_T of tracks in minimum bias events

To set the track threshold we first consider the P_T of the leading track in the tau decay. In Figure 3-14 we compare the leading tau track with the leading track in a jet. The jet sample is chosen to have an E_T spectrum similar to the taus. We use a jet trigger data sample and consider only the non-leading jet to avoid trigger bias. The spectrum is similar. This means that there is no optimum threshold cut to maximize the rejection of jets. The next consideration is the probability of a track from the underlying event falling within the cone. To maximize the acceptance for taus we want to set the threshold as low as possible without being susceptible to tracks from the underlying event. Figure 3-14 shows the track P_T distribution for all tracks in a minimum bias event. If we consider a minimum bias event to be equivalent to the underlying event then we form a cone of angle 7.5° and ask what is the probability is that a track from the underlying event lies within that cone. Since this probability changes with η we scan the cone over η. Table 3.3 shows this probability. We require the leading track to be $P_T > 2.5$ GeV. The probability for a track with $P_T > 2.5$ GeV from the underlying event to fall within the cone is less

than 0.01 %. The efficiency of this requirement is for hadronic taus in simulated (ISAJET) $p\bar{p} \rightarrow t\bar{t} \rightarrow H^+H^-b\bar{b}$, $H^\pm \rightarrow \tau\nu$ events (m_{H^+}=50 GeV, m_t=70 GeV) is 81 %.

η range	Probability(%) of track with $P_T > 2.5$ GeV in 7.5 ° cone	Probability(%) of track with $P_T > 1.0$ GeV in 7.5 ° cone	Probability(%) of track with $P_T > 1.0$ GeV in 7.5 °-17.5 ° annulus
$0.1 < \|\eta\| < 0.3$	0.023	0.41	1.7
$0.3 < \|\eta\| < 0.5$	0.029	0.46	1.9
$0.5 < \|\eta\| < 0.7$	0.033	0.49	2.2
$0.7 < \|\eta\| < 0.9$	0.037	0.68	2.7

Table 3.3: The probability of a track from the underlying event with: $P_T >$ 1.0, 2.5 GeV lying in the 7.5 ° cone , $P_T > 1.0$ GeV lying in the 7.5 ° -17.5 ° annulus.

The requirement that there be no tracks with $P_T > 1.0$ GeV in the 7.5°-17.5° annulus is to implement the isolation requirement. It is this requirement that significantly rejects jets. The tracks from tau decays are typically much closer to the cluster axis than the tracks associated with jets. This is because of the low mass of the tau. We use a tracking isolation variable rather than a calorimeter isolation variable because the hadrons in tau decays form hadronic clusters which typically extend over several towers. The consequence of this is that the taus and jets form clusters that are less easily distinguishable with a calorimeter isolation variable. The P_T spectrum of tracks from jets is similar to taus and so we again wish to set the P_T threshold as low as possible without having a high probability for a track from the underlying event to lie in the annulus. Table 3.3 gives this probability for tracks with $P_T > 1.0$ Gev and it can be seen that this threshold causes only 1-2 % of taus to be rejected due to overlap with the underlying event.

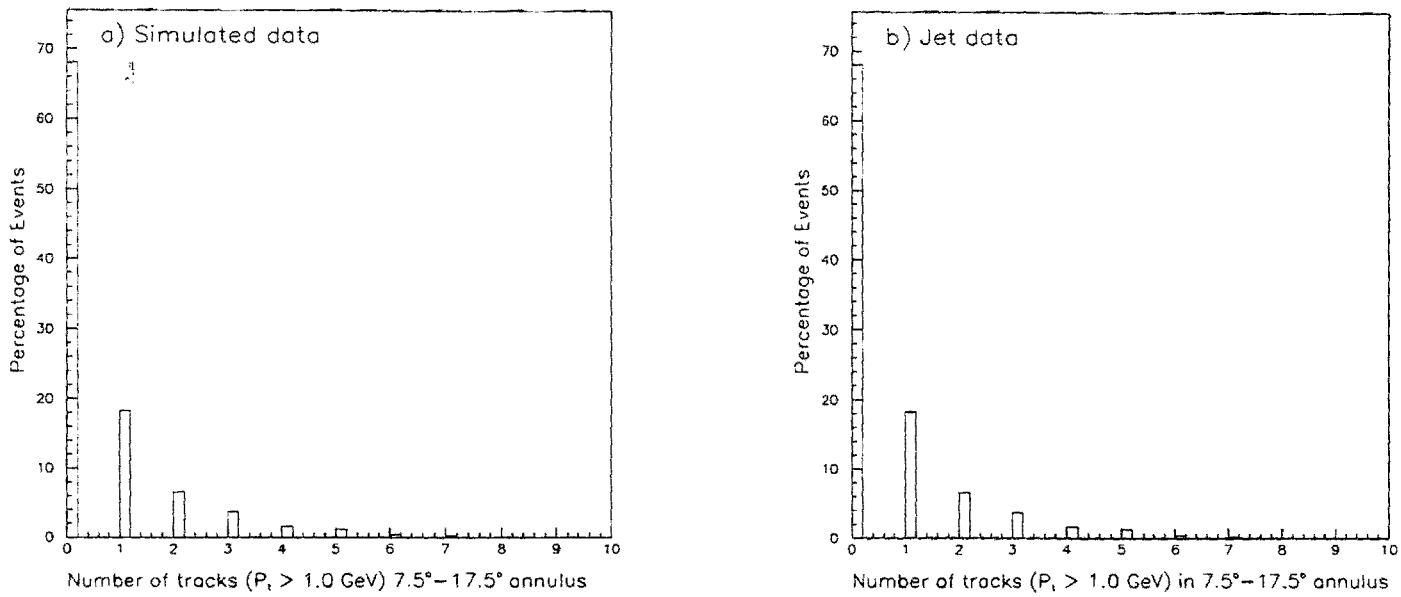

Figure 3-15: The number of tracks with $P_T > 1.0$ GeV in a 7.5°- 17.5° annulus about the tau cluster centroid for taus in simulated (ISAJET) $p\bar{p} \rightarrow t\bar{t} \rightarrow H^+H^-b\bar{b}$, $H^\pm \rightarrow \tau\nu$ events (m_{H^+}=50 GeV, m_t=70 GeV) .

Figure 3.3 shows the number of tracks with $P_T > 1.0$ GeV in the 7.5°-17.5° annulus for both taus and and a sample of jets taken from a jet trigger data set as described previously. Requiring no tracks in this region gives good rejection of jets. The efficiency of this cut for simulated (ISAJET) $p\bar{p} \rightarrow t\bar{t} \rightarrow H^+H^-b\bar{b}$, $H^\pm \rightarrow \tau\nu$ events (m_{H^+}=50 GeV, m_t=70 GeV) is 0.78 %.

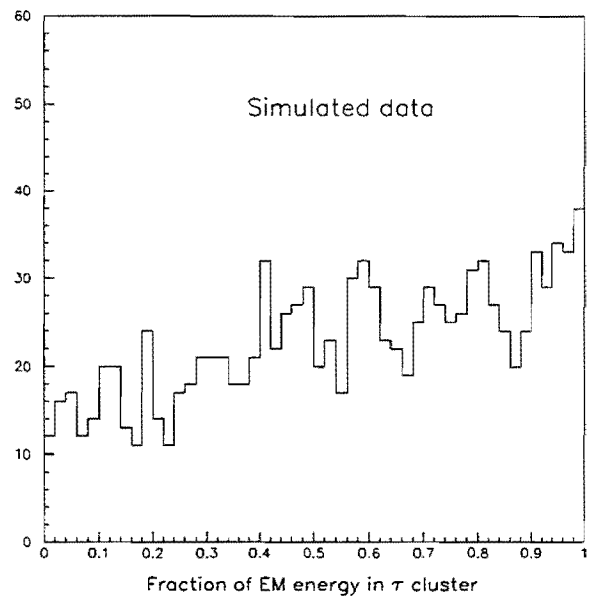

Figure 3-16: The fraction of the total cluster energy which is electromagnetic for taus in simulated (ISAJET) $p\bar{p} \rightarrow t\bar{t} \rightarrow H^+H^-b\bar{b}$, $H^\pm \rightarrow \tau\nu$ events (m_{H^+}=50 GeV, m_t=70 GeV) .

3.5.3 Electron removal

The algorithm also has high acceptance for electrons since they form narrow, often isolated, clusters with a track. An additional requirement must be added to the algorithm to remove electrons. We use the following cut on the tau cluster.

$$EM/E < 1.0 - 1.0/(7E/P)$$

where:

- E is the total energy of the tau calorimeter cluster. The total energy is the sum of the electromagnetic energy EM and the hadronic energy HAD. E=EM+HAD.
- P is the magnitude of the vector sum of all tracks with $P_T > 1.0$ GeV in the 7.5^o cone. P=$|\sum \vec{p_i}|$.

This cut is a hyperbola in the (E/P, EM/E) plane. At first glance this may seem a rather complicated way of removing electrons. Electrons have a very high fraction of electromagnetic energy. The obvious solution would be to cut on this quantity and indeed a cut of EM/E< 0.8 would remove 100 % of electrons. However, it would also remove 25 % of tau clusters. Figure 3-16 shows the EM fraction for taus. EM/E is often high since the tau decays often contain one or more π^o's which shower electromagnetically. A 25 % loss of efficiency would have a serious impact on the sensitivity of the analysis. A more efficient cut can be made by realising that a typical tau decay has one or more π^o's and one or more $\pi^\pm$ (see table 3.2). This means that when the π^o carries most of the parent tau energy the $\pi^\pm$ will have very little of the parent tau energy. The π^o showers electromagnetically and is well contained within the EM calorimeter at a typical tau P_T of 20-25 GeV. The $\pi^\pm$ often begins showering in the EM calorimeter but on average most of the energy is deposited in the HAD calorimeter. However, we can also measure the $\pi^\pm$ energy by measuring the momentum of the charged tracks in the tau decay. To translate this into experimental quantities for the tau cluster we define EM/E as the electromagnetic fraction of energy in the calorimeter cluster, and P is the total momentum of the tau decay tracks. We can then state that for a tau cluster: When EM/E is high (> 0.8), E/P is high (> 1). We now compare this to an electron. We expect an electron to shower electromagnetically with EM/E $\approx$ 1.0. We also expect that the charged track associated with the electron carries all the electrons energy so E/P $\approx$ 1.0. This means that the electrons and taus should populate a different region of the (E/P, EM/E) plane. However, to define these regions requires some care because of the effects of calorimeter resolution, charged pions that shower in the electromagnetic calorimeter, leakage of electrons showers from the electromagnetic calorimeter into the hadron calorimeter, and electron bremsstrahlung. We first consider the case where none of these effects occur. This is an ideal experiment. Figure 3-17 shows that the electrons should be at a point in the (E/P,EM/E) plane. All the electron energy is measured infinitely accurately by the EM calorimeter so EM/E=1.0. All of the energy of the electron charged track is deposited in the calorimeter so E/P =1.0.

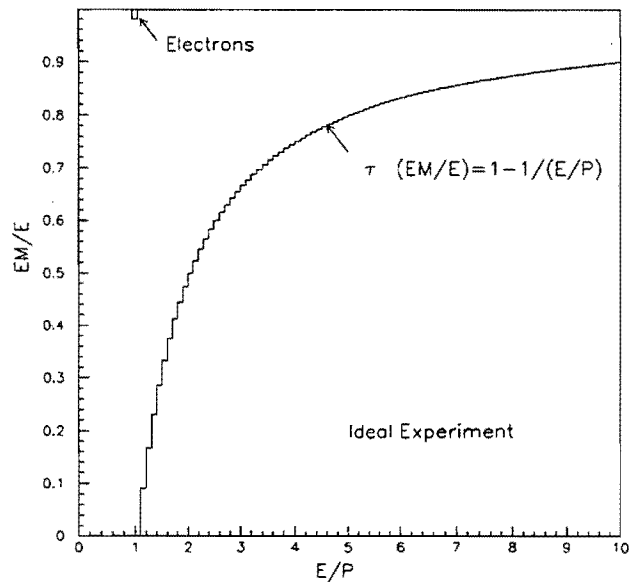

Figure 3-17: The electromagnetic energy fraction vs energy/momentum for taus and electrons in an ideal experiment.

In an ideal experiment the taus should lie along a hyperbola. We can see this as follows

$$\mathrm{EM} + \mathrm{HAD} = \mathrm{E}$$

All the charged pion momentum is measured perfectly by the tracking chamber. All the HAD energy comes from the charged tracks and is measured perfectly so HAD=P. Then substituting

$$\mathrm{EM} + \mathrm{P} = \mathrm{E}$$

Then dividing by E throughout

$$\mathrm{EM/E} = 1 - 1/(\mathrm{E/P})$$

We now consider the effects in a real experiment which smear out these regions. This is illustrated in figure 3-18. If the electron shower is not fully contained in the EM calorimeter then EM/E < 1.0. For real electrons the EM/E distribution drops approximately exponentially to zero at about EM/E $\approx$ 0.8-0.85. The EM calorimeter also has a finite but low resolution (compared to the HAD calorimeter) so the point

is also smeared slightly in the ± E/P direction. If the electron bremsstrahlungs, the radiated photon energy is measured in the calorimeter cluster along with the electron, but the momentum of the measured charged track is reduced so E/P > 1.0. For real electrons the E/P distribution drops rapidly to a small value at about 1.5-2.0 but there is still a small but decreasing probability out to much higher value. The two effects of leakage and bremsstrahlung are uncorrelated so that when EM/E is low, E/P is unlikely to be high and vice versa. The electron populates the region shown in figure 3-18.

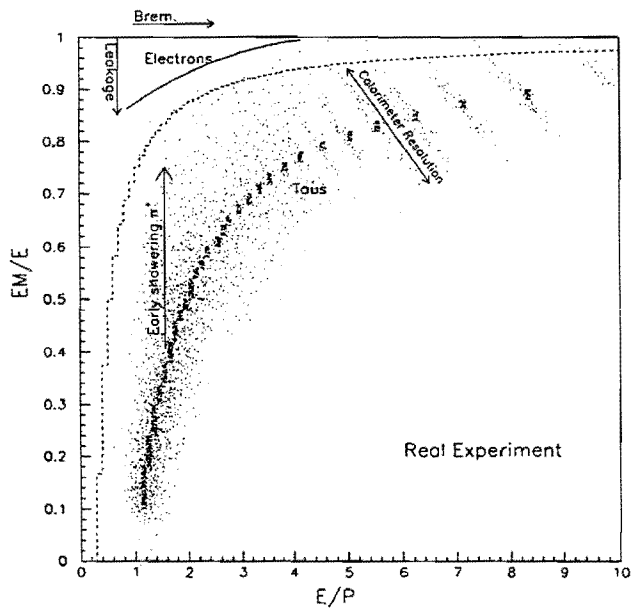

Figure 3-18: The electromagnetic energy fraction vs energy/momentum for taus and electrons in an real experiment from a toy Monte Carlo.

If we now consider the tau in a real experiment. First, if the charged pions deposit energy in the EM calorimeter, E and P remain the same. EM/E is increased while E/P stays constant. The taus are shifted in the +EM/E direction away from the hyperbola. Second, the resolution of the HAD calorimeter is large. To illustrate the effect we consider a set of points along the hyperbola. We then fluctuate the HAD energy measurement and recalculate EM/E and E/P. The points are smeared out as shown in figure 3-18. The line which bounds these points is still a hyperbola but shifted. The appropriate choice of cut to separate the electron region from the tau

region is then

- EM/E < 1.0 - 1.0/(7.E/P) taus
- EM/E > 1.0 - 1.0/(7.E/P) electrons

This cut is tuned by using real electrons and simulated taus. Figure 3-19 shows the regions populated by unbiased electrons from Z decay data and taus from simulated (ISAJET) $p\bar{p} \rightarrow t\bar{t} \rightarrow H^+H^-b\bar{b}$, $H^\pm \rightarrow \tau\nu$ events (m_{H^+}=50 GeV, m_t=70 GeV) .

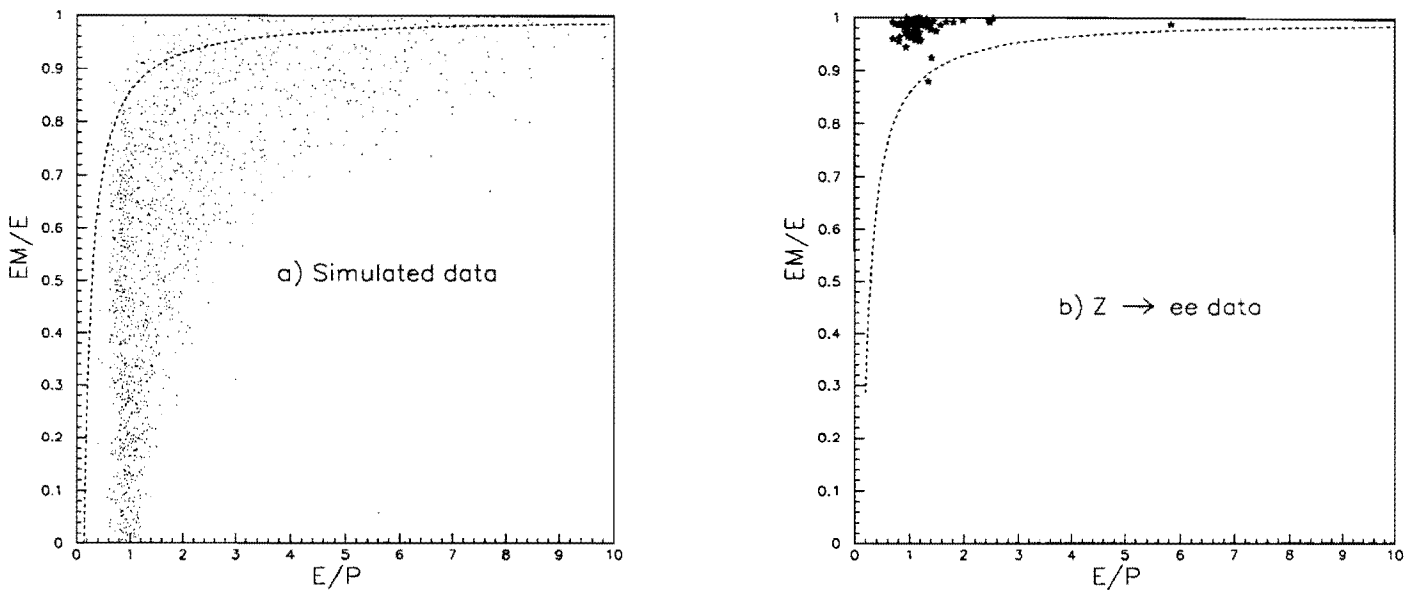

Figure 3-19: The electromagnetic energy fraction vs energy/momentum for a) taus in simulated (ISAJET) $p\bar{p} \rightarrow t\bar{t} \rightarrow H^+H^-b\bar{b}$, $H^\pm \rightarrow \tau\nu$ events (m_{H^+}=50 GeV, m_t=70 GeV) which have passed the tau cluster and track requirements. b) Unbiased electrons from $Z \rightarrow ee$ events. The cut used to separate taus and electrons EM/E < 1-1/(7E/P) is shown.

In the Z→ e^+e^- sample we require one good central electron with the standard electron cuts used in several previous analysis at the CDF (see appendix A). We form the invariant mass of this electron with a tau cluster (i.e the other electron) as defined above and require 80 GeV < M_{ee} < 105 GeV. The cut removes $98.0 \pm 1.5\%$ of electrons. This efficiency is also confirmed with simulated electron data. We use

the simulated taus to estimate that 94 % of taus, which have passed the cluster and track requirements of the tau algorithm, are accepted.

3.5.4 Summary of tau algorithm cuts

Description	Cut	Efficiency for $t \rightarrow H^+b$ events (m_{H^+} = 50 GeV,m_t = 70 GeV)
Geometrical acceptance	At least one hadronic tau $0.1 < \|\eta\| < 1.0$	0.66
Kinematic acceptance	Tau forms cluster $E_T > 15$ GeV	0.65
Hadronic tau algorithm	Leading track $P_T > 2.5$ GeV	0.81
	Isolation: No tracks $P_T > 1.0$ GeV in 7.5°-17.5° annulus	0.79
	Electron removal: E/P < 1-1/(7E/P)	0.94
Total		0.26

Table 3.4: A summary of the tau algorithm cuts and the efficiencies for simulated (ISAJET) $p\bar{p} \rightarrow t\bar{t} \rightarrow H^+H^-b\bar{b}$, $H^\pm \rightarrow \tau\nu$ events (m_{H^+}=50 GeV, m_t=70 GeV) . The efficiencies are calculated sequentially. The total is the product.

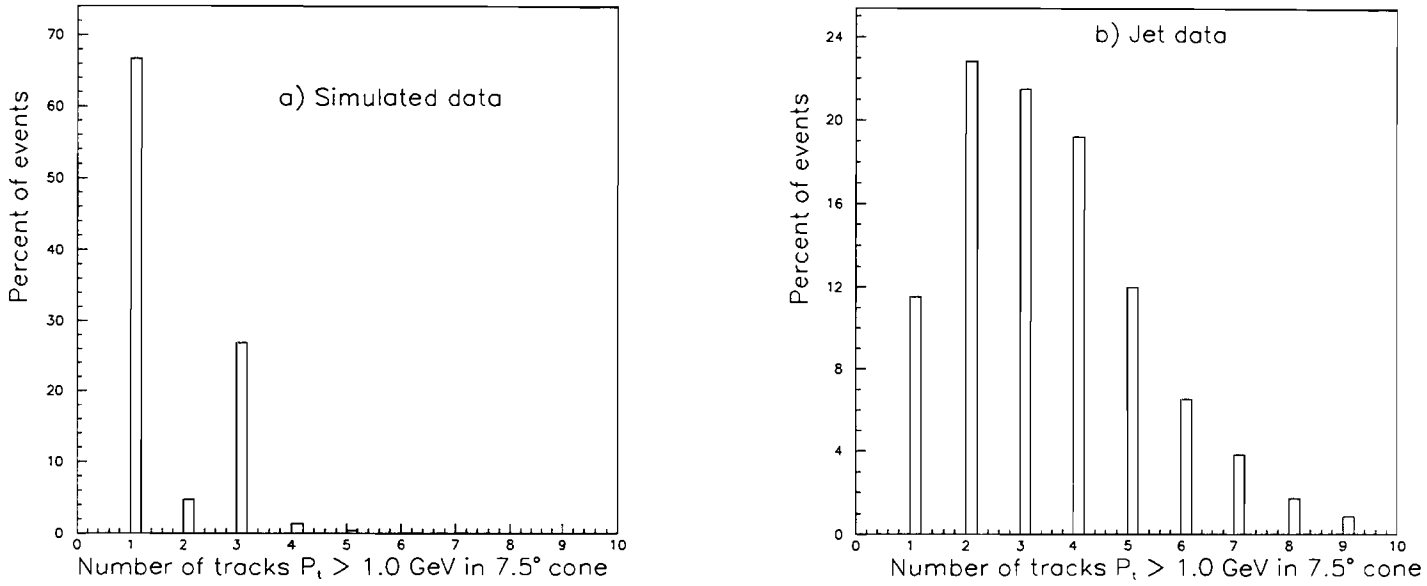

Figure 3-20: Number of tracks in 7.5° cone with $P_T > 1.0$ GeV (N_{track}) a) taus in simulated (ISAJET) $p\bar{p} \rightarrow t\bar{t} \rightarrow H^+H^-b\bar{b}$, $H^\pm \rightarrow \tau\nu$ events (m_{H^+}=50 GeV, m_t=70 GeV) . b) Jets in a jet data set. The E_T and η distributions of the jets are the same as the tau sample. The taus and jets are required to pass all tau algorithm cuts.

We summarize the hadronic tau algorithm cuts and the efficiencies in table 3.4. This algorithm is 60 % efficient for taus with $0.1 < |\eta| < 1.0$ which have formed a cluster with $E_T > 15.0$ GeV, and rejects 87 % jets with $E_T > 15.0$ GeV. Most of this rejection comes from the isolation requirement. To distinguish between taus and jets that pass the tau algorithm cuts we define a signal variable as the number of tracks in the 7.5° cone with $P_T > 1.0$ GeV (N_{track}) as shown in figure 3-20. Taus have a characteristic one and three prong surplus. The distribution for jets is quit different. The jet sample has been chosen to have the same E_T and η distribution as the taus. The jet data was taken from a sample which required a jet trigger to be passed. To avoid trigger bias we use the non-leading jets. To verify the algorithm on real data we now show that we can find a $W \rightarrow \tau\nu$ signal.

3.6 Testing the hadronic tau algorithm

The algorithm in section 3.5 is based on that used in a previous CDF paper which measured the ratio of cross sections $\sigma(p\bar{p} \rightarrow W \rightarrow \tau\nu)/\sigma(p\bar{p} \rightarrow W \rightarrow e\nu)$. This is a test of lepton universality. If the SU(2)$\otimes$U(1) structure of the standard model is correct then we expect the coupling of $W^{\pm}$ to $\tau\nu$ to be the same as the coupling of $W^{\pm}$ to $e\nu$ i.e $g_{\tau} = g_e$. The CDF has measured $g_{\tau}/g_e = 0.97 \pm 0.07$ [57]. The algorithm used in this thesis differs from that used in $W \rightarrow \tau\nu$ analysis because it has been tuned for $t\bar{t}$ events as opposed to $W \rightarrow \tau\nu$ events in the universality measurement. The taus in $t\bar{t}$ events are less isolated as there is more jet activity. Also since $m_{H^+} < m_{W^+}$ the taus have lower E_T . However we should be able to use our algorithm to find a distinct one and three prong tau signature from $W \rightarrow \tau\nu$ events. We should further show that the number of taus estimated is consistent with the $W \rightarrow \tau\nu$ analysis. Using the $t\bar{t}$ tau algorithm we require

- One hadronic tau (defined in section 3.5)
- No other cluster with $E_T > 10$ GeV
- $\not{E}_T > 25$ GeV, $Z_{vertex} < 60$cm
- $\frac{\not{E}_T}{\sqrt{\sum E_T}} > 2.5$
- $\not{E}_T$ trigger and $\not{E}_T$ filter passed

The $\not{E}_T$ requirements etc are just those of our $\not{E}_T$ data stream which is the same data stream used for the previous $W \rightarrow \tau\nu$ analysis. Figure 3-21 shows the distribution of tracks in the signal cone for the 576 events that satisfy these requirements. Also shown is the E_T distribution.

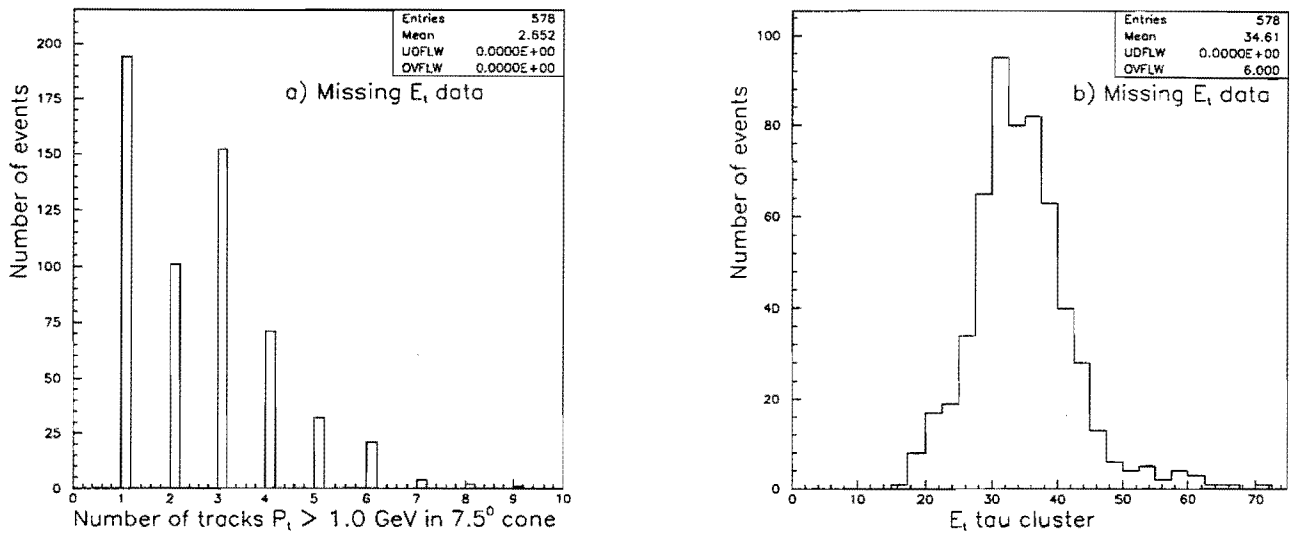

Figure 3-21: The E_T and N_{track} for W $\rightarrow \tau\nu$ candidate events from the $\not{E}_T$ data set

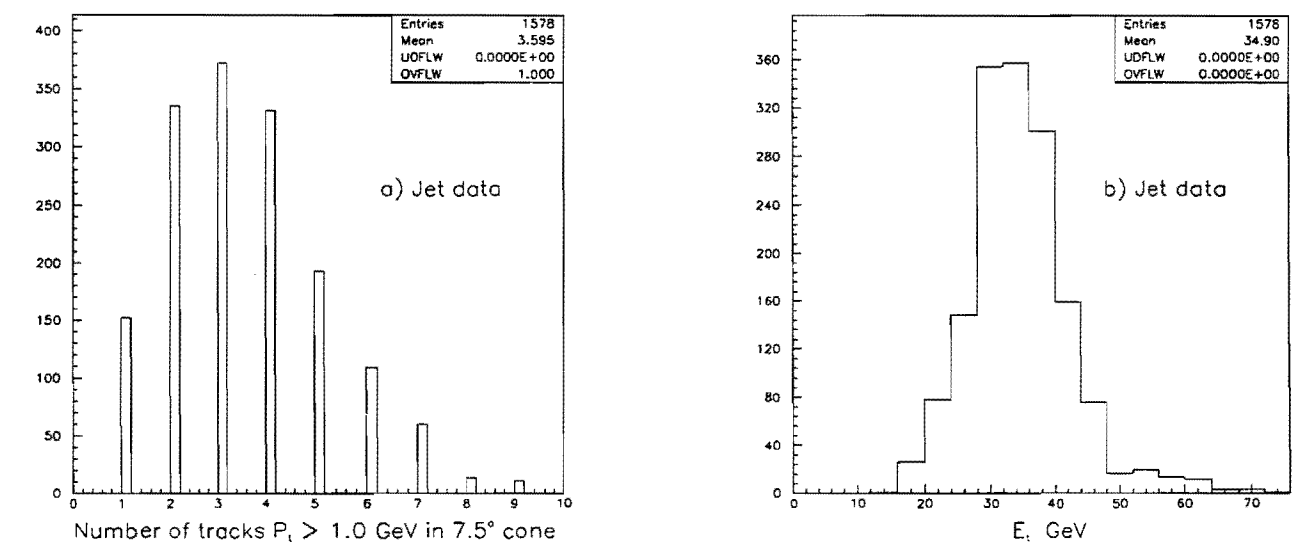

Figure 3-22: The E_T and N_{track} for a sample of unbiased QCD jets, from a jet data set, which pass the hadronic tau algorithm requirements

The one and three prong surplus is clear. However, note that even with the requirement of this quite distinct topology there is still significant background. To estimate

the number of taus we must estimate the backgrounds. There are three significant backgrounds.

- QCD - typically a dijet event in which one jet is miss-measured to give spurious $\not{E}_T$ and the other jet passes the tau algorithm cuts.
- Residual Electrons. The electron removal procedure removes 98.5±1.5 % events so we expect some residual electrons from $W \rightarrow e\nu$.
- $Z \rightarrow \tau\tau$ where the neutrino in the tau decay causes $\not{E}_T$.

Figure 3-22 shows the track multiplicity and E_T distribution of a sample of QCD jets taken from a jet data stream. We use non-leading jets to avoid trigger bias. The jets are required to pass the tau algorithm cuts described above and are selected so that the E_T, η distribution of the QCD sample is the same as the data. In figure 3-23 we normalize the QCD background sample and compare to data.

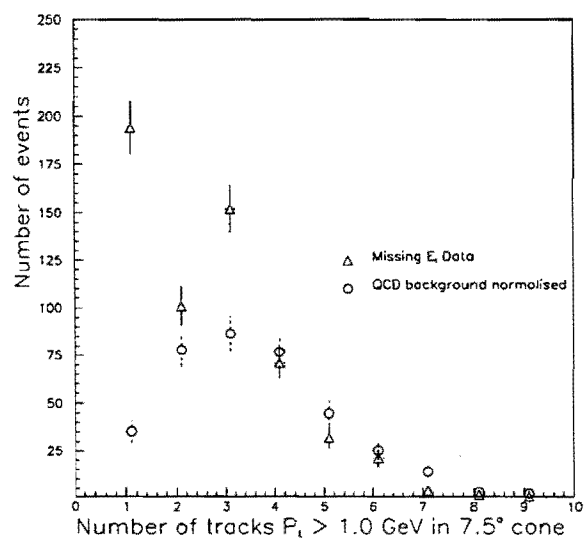

Figure 3-23: N_{track} for $W \rightarrow \tau\nu$ candidate events from the $\not{E}_T$ data set, and for a normalized QCD jet background sample taken from unbiased jets in a jet data set

The normalization is done by recognizing that in the data the 2,4,5,6 track bins are almost entirely jets while the 1 and 3 track bins contain jets plus taus. After

subtraction we estimate a surplus of 223±22 events. The error is due to the binning statistics. The systematic errors in this estimation due to 1. variation in the E_T distribution of the background sample 2. the fact that some taus are 2 prong (see figure 3-20) are negligible compared to this error. Of the 223±22 we estimate that 39±29 are residual electrons, by counting the number of electrons removed by the cut in figure 3-19 and knowing that the efficiency is 98±1.5 %. We therefore estimate 184(36) taus. The contribution from Z→ $\tau\tau$ is estimated using the ISAJET Monte Carlo to be 18 events and so measure 166±36 W → $\tau\nu$ events. One of these events is shown in figure 3-24 and figure 3-25.

The tau algorithm used above is similar to that used in the previous CDF W → $\tau\nu$ analysis. In the above measurement of the number of W → $\tau\nu$ we use the same trigger and the data stream cuts as reference [57]. The tau algorithm is different (the cuts for the W → $\tau\nu$ analysis in reference [57] are given in appendix B). It follows that the number of W → $\tau\nu$ events observed should scale with the relative acceptances which can be estimated with an ISAJET W → $\tau\nu$ Monte Carlo data set. In [57] 132±14 taus are observed. We estimate that in our analysis we should get approximately 15 % more taus and so we would expect 152±16. We observe 166±39. The two results are consistent so that our algorithm produces a result which is consistent with lepton universality. The difference is the algorithms is due to the decreased size of the tau isolation cone and the lower track thresholds which give a higher efficiency for taus.

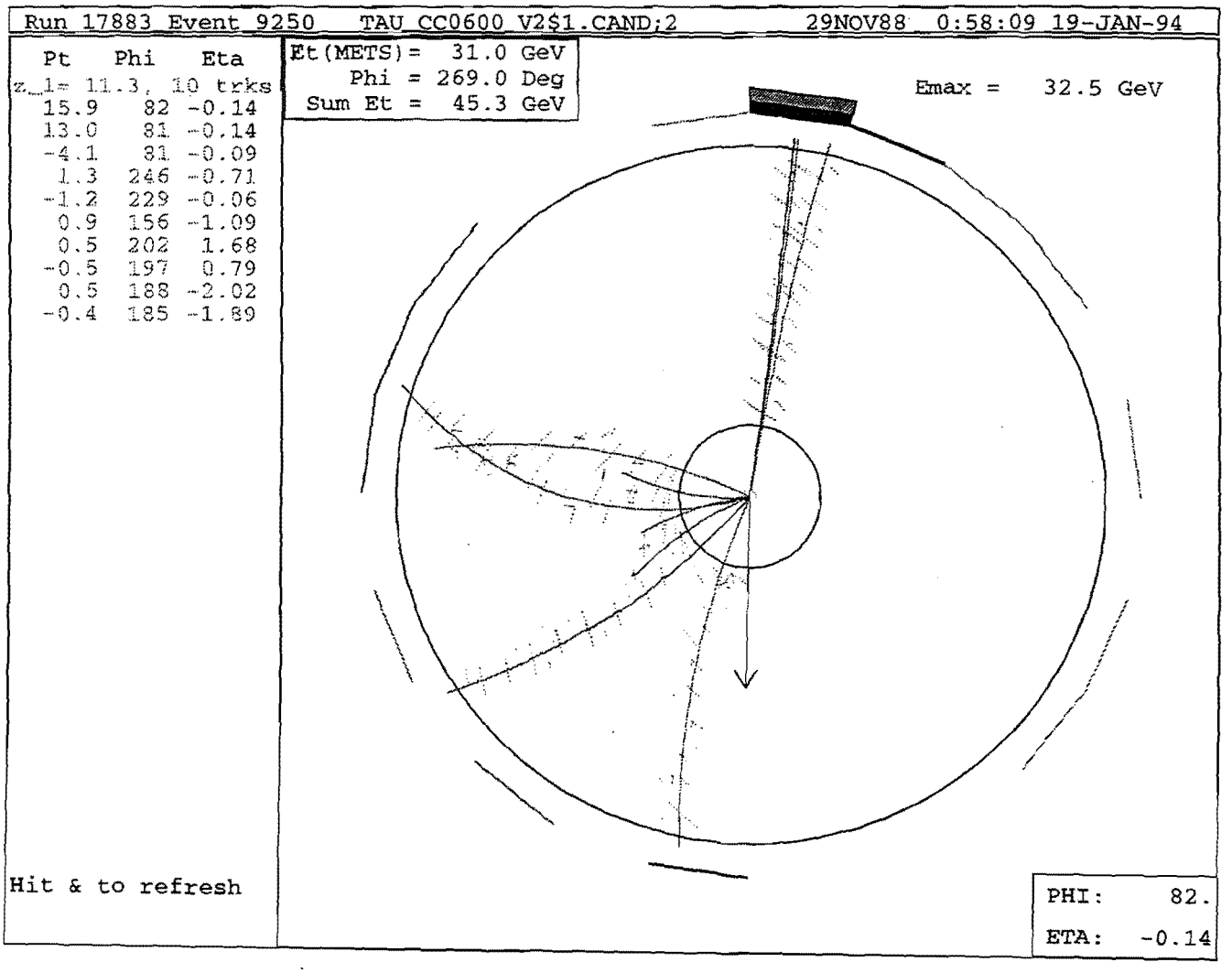

Figure 3-24: A candidate W $\rightarrow \tau\nu$ event. The central tracking chamber is shown. The event contains a three prong W $\rightarrow \tau\nu$ and large $\not{E}_T$ opposite the candidate cluster.

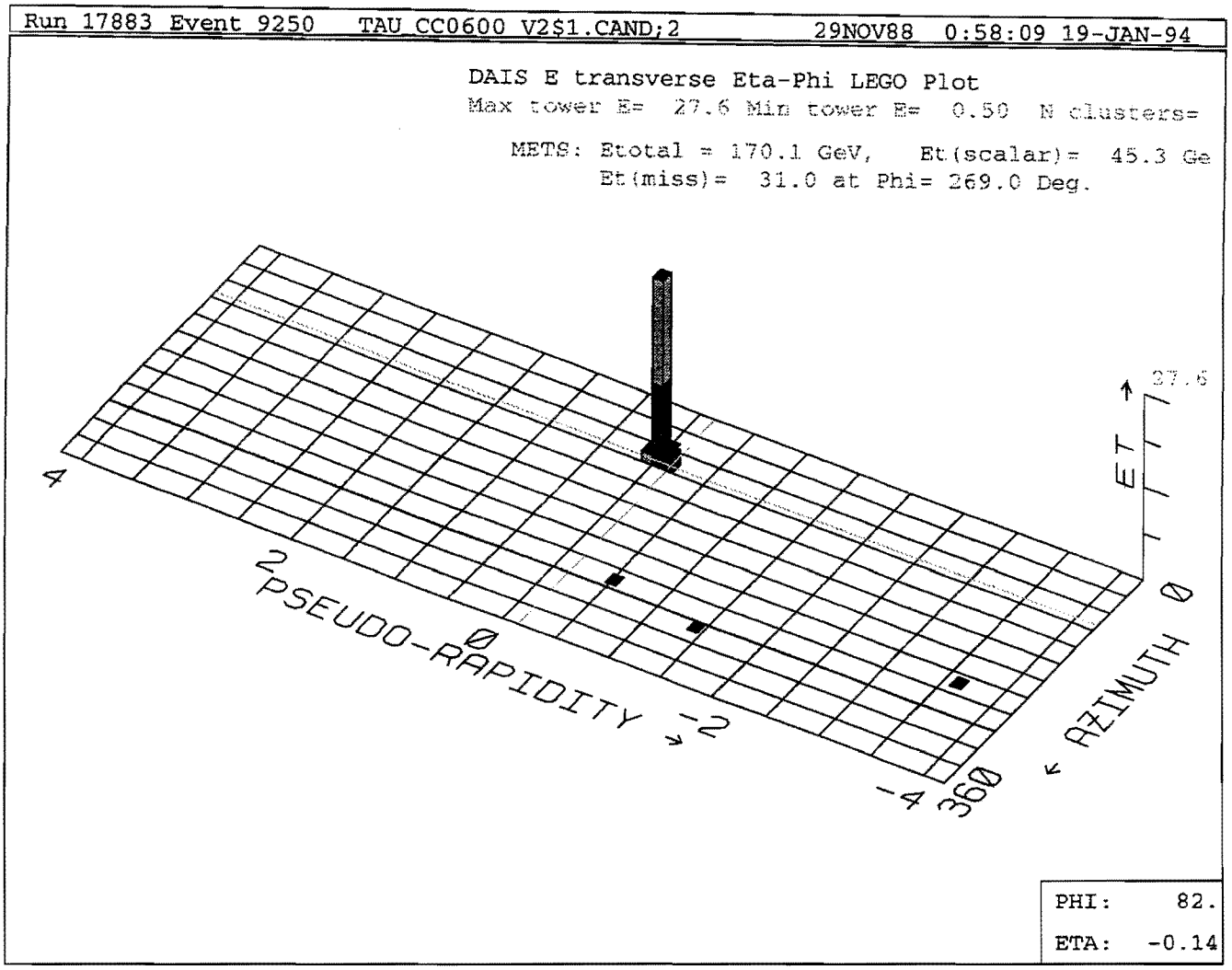

Figure 3-25: A candidate W $\rightarrow \tau\nu$ event. A lego plot of the calorimeter is shown. The distinct "monojet" topology is apparent.

3.7 Defining a top to charged Higgs signature using hadronic taus $\not{E}_T$ and jets

We combine the previous sections to define a top to charged Higgs signature. We require

- The $\not{E}_T$ trigger be passed as described in section 3.3
- The $\not{E}_T$ data stream cuts be passed as described in section 3.4.2
- There be at least one hadronic tau as described in section 3.5
- There be at least one other calorimeter cluster (R=0.4) with $E_T > 12$ GeV and $|\eta| < 3.5$.

The last requirement is because a $t\bar{t}$ event almost always has a calorimeter cluster other than the hadronic tau. This cluster is one of the following

1. b jets
2. The other tau that did or did not pass the hadronic tau cuts.
3. a gluon jet

Figure 3-26 shows the E_T and η of the highest E_T cluster (R=0.4) other than the highest E_T tau candidate. This may be a tau that did or did not pass the tau identification cuts, a jet from the b or a jet arising from initial or final state gluon radiation. We require this cluster to be $E_T > 12.0$ GeV and $|\eta| <$ .lt.3.5. Requiring this additional cluster gives an acceptance of 75 % of the events that pass all the preceding cuts.

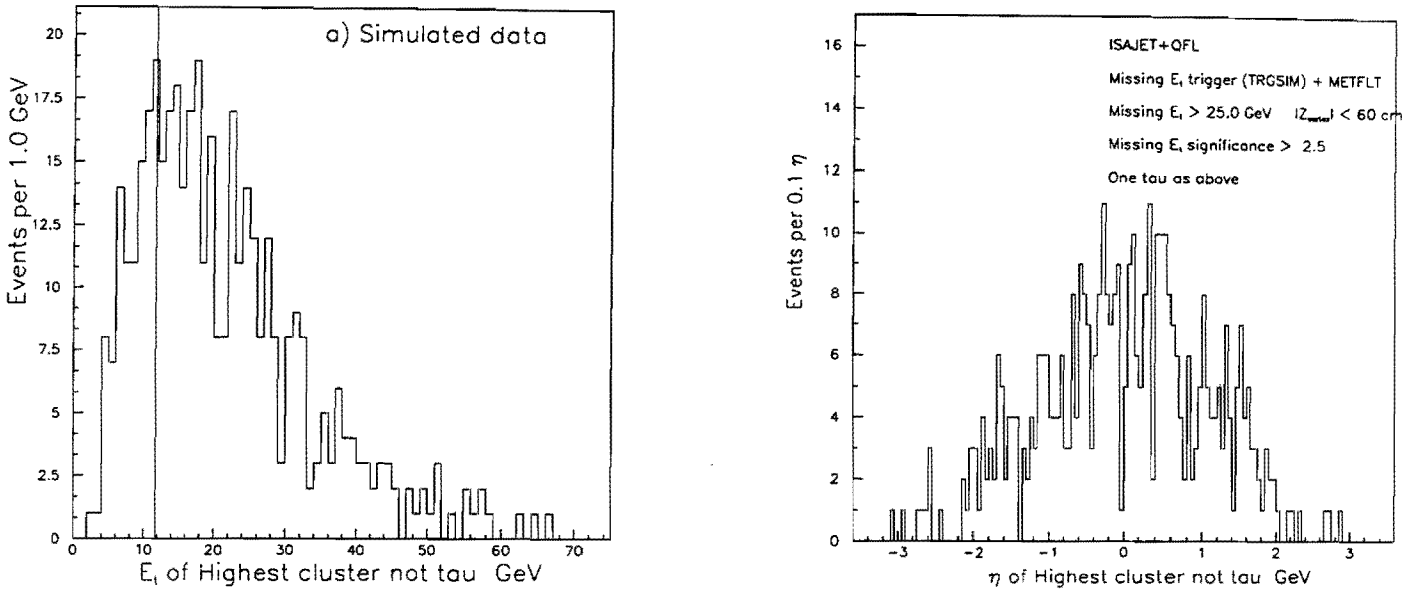

Figure 3-26: The E_T and η of highest E_T cluster which is not a tau candidate, for simulated (ISAJET) $p\bar{p} \rightarrow t\bar{t} \rightarrow H^+H^-b\bar{b}$, $H^\pm \rightarrow \tau\nu$ events (m_{H^+}=50 GeV, m_t=70 GeV) .

3.8 Calculation of overall efficiency

We have tabulated the efficiencies of the selection cuts for simulated (ISAJET) $p\bar{p} \rightarrow t\bar{t} \rightarrow H^+H^-b\bar{b}$, $H^\pm \rightarrow \tau\nu$ events (m_{H^+}=50 GeV, m_t=70 GeV) in table 3.1, table 3.4 and above. In this case the expected number of events is

$$N = \sigma_{t\bar{t}} \cdot \int Ldt.A.\epsilon_1.K$$

$A.\epsilon$ is the product of the quoted efficiencies. K is a small correction factor that arises because some of the hadronic tau candidates are actually b's or jets. In the calculation of the efficiency we require the hadronic tau candidate be matched to a generated tau. This removes the b jets and gluon jets that fake a tau candidate, and is equivalent to the background subtraction that we use to remove jets from the tau candidates in the data. For the example we are considering K=0.89. The expected number of events is then 47. In chapter 4 we tabulate the expected number of events

for the range of m_{H^+}, m_t, $Br(H^+ \rightarrow \tau\nu_\tau)$ in the search region defined in chapter 1. We also discuss the systematic errors associated with this estimation.

Chapter 4

Computing the Expected Number of Signal events and the Error

In this chapter we describe the computation of the expected number of signal events (N_{expect}). This calculation has three components, the theoretical $t\bar{t}$ production cross section $\sigma_{t\bar{t}}$, the total integrated luminosity $\int$Ldt and the overall acceptance$\times$ efficiency of the selection cuts A.ϵ. The expected number of signal events is then given by

$$N_{expect} = \sigma_{t\bar{t}} \; . \; \int Ldt \; . \; A.\epsilon$$

We first describe the theoretical calculation of $\sigma_{t\bar{t}}$ and the uncertainties in the calculation. The estimation of the overall acceptance$\times$efficiency has been described in detail in chapter 3. Here we briefly describe the ISAJET Monte Carlo that was used extensively to estimate the $A.\epsilon$, and discuss systematic errors associated with this estimation. Finally we tabulate the expected number of signal events and the error for the range of m_{H^+},m_t and $Br(H^+ \rightarrow \tau\nu_\tau)$ under consideration.

4.1 Theoretical calculation of $t\bar{t}$ cross sections

In this thesis we use the next-to-leading order calculation of Ellis *et al.* [49]. We do not attempt a detailed discussion of the calculation but rather a brief outline of the technique with particular emphasis on the theoretical uncertainties involved.

4.1.1 Outline of the calculation

We begin by writing down the expression for top production using the QCD improved parton model. The cross section σ for a hard scattering with the characteristic momentum scale $\mu_R = \mu_F = q^2$, between a proton and an anti-proton with momenta P_1, P_2 is

$$\sigma(P_1, P_2, \mu_R, \mu_F) = \sum_{i,j} \int dx_1 dx_2 f_i^p(x_1, \mu_F) f_i^{\bar{p}}(x_1, \mu_F) \hat{\sigma}_{ij}(x_1 P_1, x_2 P_2, \alpha_S(\mu_R))$$

f_i^p and $f_i^{\bar{p}}$ are the parton structure functions for partons of type i,j with fraction x of the proton(antiproton) momentum. The short distance cross section $\hat{\sigma}_{ij}$, calculated at the rescaled value of the incoming hadron momenta P_1, P_2, is expressed as a perturbative expansion in powers of $\alpha_S(\mu_R)$. The mass singularities, which arise as a result of the emission of collinear gluons, are factored from the short distance cross section and placed in the parton distribution functions. The parton distribution functions are then functions of the scale at which this is done, μ_F. The renormalization scale μ_R is the scale at which ultraviolet divergences are subtracted. The $\overline{MS}$ [50] renormalization scheme is used with five active flavors. In top quark production the typical scale of the momentum transfer q^2 is of the order of m_t and this sets the scales $\mu_R = \mu_F = q^2$. The high value of q^2 ensures that the quarks are sufficiently free and thus that perturbation theory is valid. The particular choice of values for μ_R, μ_F should not in principle affect the result. In practice it does because we are only able to calculate to a finite order in $\alpha_S(\mu_R)$. The sensitivity of the calculation to changes in the choice of μ_R, μ_F is indicative of the contribution of uncalculated higher order diagrams and is an important test for the validity of the perturbative expansion.

Figure 4-1 shows the leading, and some next-to-leading order diagrams for heavy quark production. The calculation is complete to next-to-leading order $(\alpha_S(\mu_R)^3)$.

The total cross section is calculated by integrating the matrix elements over the structure functions and the appropriate phase space factors. The form of the light quark (u,d) structure functions is determined from deep inelastic scattering experiments for x$\geq$ 0.01 and μ_F < 15 GeV. The gluon structure function can not be directly measured and is inferred from these experiments. Figure 4-2 shows the total cross-section as function of top mass. It can be seen that the cross section falls very rapidly as the mass increases. The calculation also shows that the dominant part of the $t\bar{t}$ cross section is from t and $\bar{t}$ quarks produced centrally, with a P_T of the order of m_t, and close to each other in rapidity $|\Delta y| \approx 1$.

4.1.2 Uncertainties in the calculation

The uncertainty in the calculation derives from uncertainties in the choice of Λ, the structure functions and the effect of uncalculated higher order graphs. Λ is the QCD parameter in $\overline{\text{MS}}$ renormalization scheme with five active flavors. It affects the running of the coupling constant since $\alpha_S(\mu_R)$ is given by

$$\alpha_S(\mu_R) = \frac{1}{b\ln(\mu_R^2/\Lambda^2)}\left[1 - \frac{b'\ln(\ln(\mu_R^2/\Lambda^2))}{b\ln(\mu_R^2/\Lambda^2)} + ...\right]$$

To get an estimate of the uncertainty from Λ this parameter is varied in the range

$$100\text{MeV} < \Lambda < 250\text{MeV}$$

For a top mass of 100 GeV this implies a variation in $\alpha_S(\mu_R)$ of

$$0.104 < \alpha_S(\mu_R) < 0.118$$

The extraction of Λ from deep inelastic scattering is correlated with the form assumed for the gluon structure function. This is because the data used to infer the gluon structure function can be described by a stiff gluon distribution and a large Λ, or a softer gluon distribution and a smaller Λ. The gluon distribution function itself is the least well known structure function since it cannot be directly measured. To estimate the uncertainty due to gluon distribution and the correlated Λ uncertainty, three different sets of structure functions due to Diemoz *et al.* [62] are used with values of Λ=100,170 and 250 MeV. The sensitivity of the the calculation to changes in $\mu = \mu_R = \mu_F$ gives an indication of the uncertainty due to higher order uncalculated

graphs. Figure 4-3 shows the variation of the cross section with μ for the leading and next-to-leading order calculations. It can be seen that the next-to-leading order calculation is stabilizing with respect to the leading order calculation, i.e getting less sensitive to changes in μ. This gives confidence that the perturbation expansion is valid. It also allows selection of an appropriate range over which to vary μ to get a measurement of the uncertainty from higher order contributions. The range used is

$$\mu/2 < \mu < 2\mu$$

The overall theoretical uncertainty is computed using the extrema of these variations. The cross sections are given for the relevant top mass range, with the upper and lower bounds, in table 4.1. We use the lowest values in the estimation of the number of signal events expected.

m_t GeV	low $\sigma_{t\bar{t}}$(pb)	$\sigma_{t\bar{t}}(pb)$	high $\sigma_{t\bar{t}}$(pb)
40	7460	9628	11950
50	2507	3210	3882
60	1005	1274	1508
70	457	574	673
80	229	284	332
90	124	153	176

Table 4.1: The $t\bar{t}$ production cross sections at 1.8 TeV from Ellis *et al.*, with upper and lower bounds due to the theoretical uncertainty in the calculation

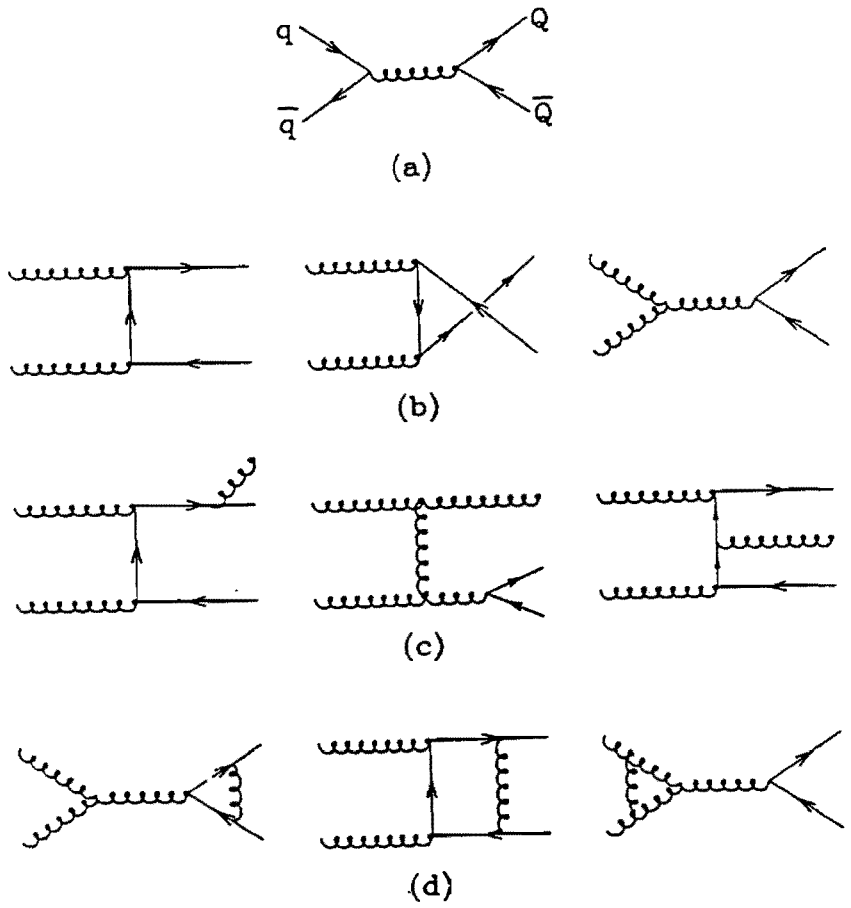

Figure 4-1: The leading order and some next-to-leading order diagrams for $t\bar{t}$ production.(a) Leading order quark fusion.(b) Leading order gluon fusion (c) Next-to-leading order real emission processes.(d) Next-to-leading order loop diagrams

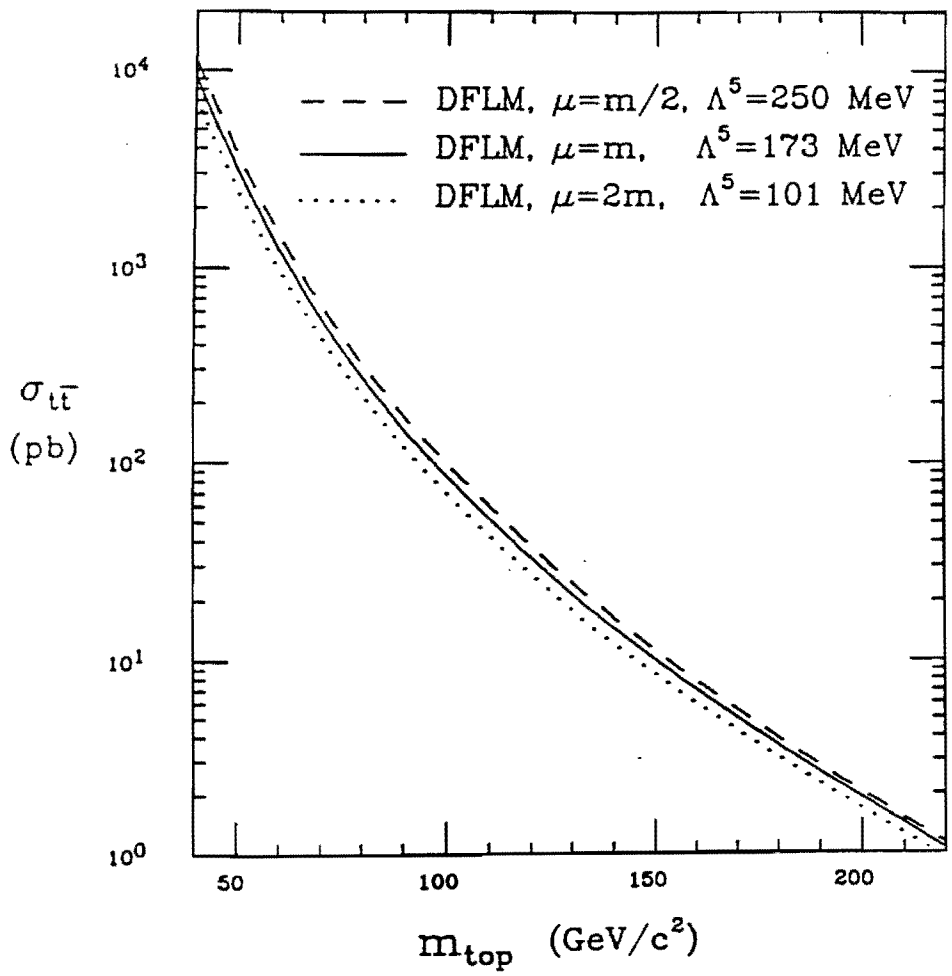

Figure 4-2: The $t\bar{t}$ production cross section as a function of m_t at 1.8 TeV to order $\alpha_S(\mu_R)^3$.

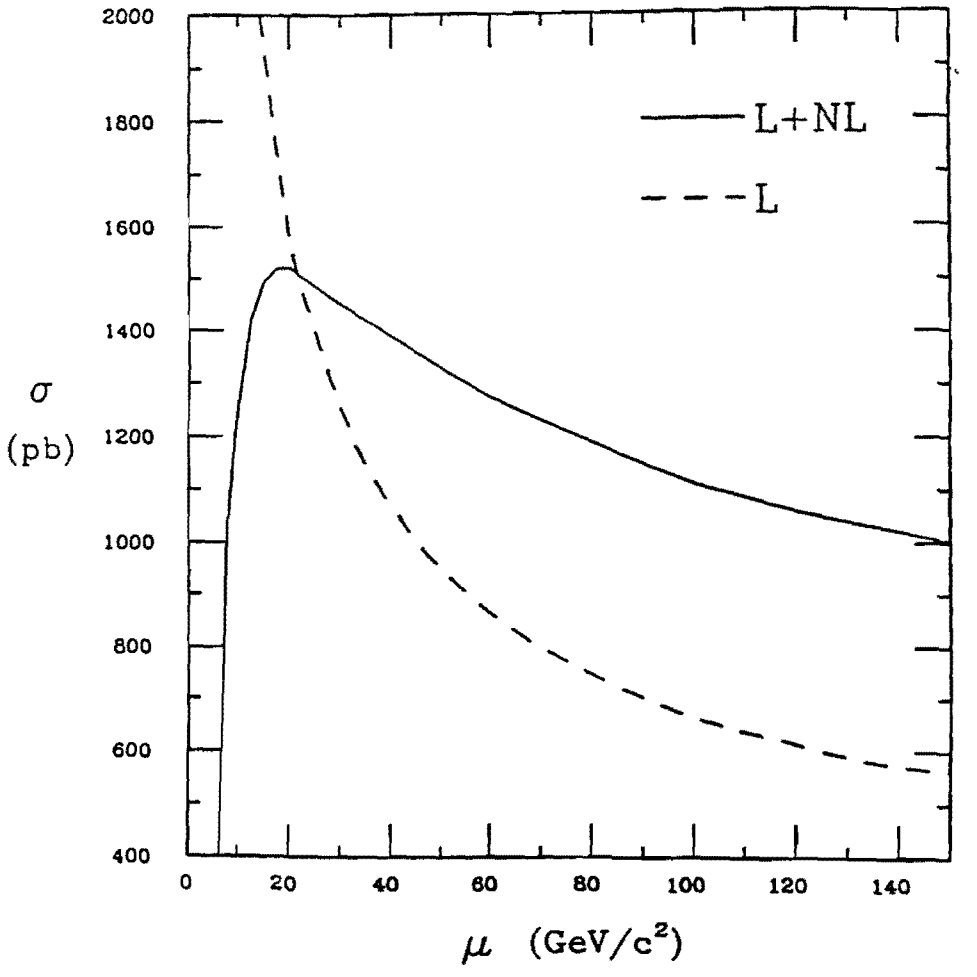

Figure 4-3: The dependence of the $t\bar{t}$ production cross section at 1.8 TeV with $m_t = 60$ GeV on the renormalization and factorization scale μ.

4.2 The ISAJET Monte Carlo

We use the ISAJET Monte Carlo [47] to generate samples of

$$p\bar{p} \rightarrow t\bar{t} \rightarrow H^+H^-b\bar{b}; H^+ \rightarrow \tau^+\nu_\tau, H^+ \rightarrow \tau^-\bar{\nu}_\tau$$

events for different (m_{H^+}, m_t) combinations. The charged Higgs is built into version 6.36 and only a small modification is required to take care of the correct polarization of the tau from the Higgs decay [48]. ISAJET only calculates the production cross sections to leading order. The Monte Carlo data sets are used to calculate the acceptances and efficiencies of the various selection cuts. The calculations are then normalized to the next-to-leading order theoretical cross sections described in section 4.1. This is a valid procedure since the addition of the next-to-leading diagrams changes only the absolute cross section and does not significantly affect the kinematics of the $t\bar{t}$ production.

ISAJET begins the process of generating $t\bar{t}$ events by convoluting the leading order QCD cross sections with the parton structure functions. The parton structure functions are evolved to the correct q^2 using the Altarelli-Parisi equations. The EHLQ1 structure functions were used and the QCD scale is set to

$$q^2 = \frac{2stu}{s^2 + t^2 + u^2}$$

where s,t,u are the Mandelstam variables for the hard scatter. This is equivalent to the $q^2 = m_t$ scale used in the theoretical calculations. The initial and final state partons are developed into parton cascades using the independent branching approximation algorithm of Fox and Wolfram [58]. The essential feature of this algorithm is that one may neglect interference between the amplitudes for successive emissions and the spectra of the radiated partons are described by independent probability distributions. The application of this algorithm to initial state radiation uses a technique by Sjostrand [59]. The algorithm starts with the hard scattering partons and successively reconstructs preceding branchings in a falling sequence of q^2. The advantage of this is that the Altarelli-Parisi equations can be recast in a suitable form to make the algorithm numerically efficient. The next step in the generation is to fragment the final state partons into hadrons and we briefly describe the essential features of this process.

In a $q\bar{q}$ event the color charge of the q is exactly balanced by the color charge of the $\bar{q}$. As the q and $\bar{q}$ recoil against each other they stretch the color flux lines that bind them. Eventually the flux lines break, materializing $q\bar{q}$ pairs, and the various colored components that result regroup into colorless hadrons. The central concept used in fragmentation models is that the regrouping into hadrons takes place locally and so the properties of the quark jet depend only upon the quark (its color charge, quantum numbers, and momentum). This implies that the process is not affected by the initial state partons, which is a good assumption for the high energy processes we are considering since the time scale of the hard scatter is much less that the time taken for hadronization. This is known as the independent fragmentation model [60]. Fragmentation is described by a set of fragmentation functions $D(z)^h$ analogous to structure functions. $D(z)^h$ is the probability of finding a hadron h with a longtitudal momentum fraction z of its parent parton. The longtitudal momentum is the momentum along the parent parton direction of motion. The parameterization of these functions is based on phenomenological arguments and comparison to data.

ISAJET uses the independent fragmentation model described above. In the case of heavy quarks (c,b,t) the Peterson model [51] is used. This has been shown to correctly model the fragmentation of the c and b quarks. It is relevant to top production, in the mass range considered, since the width of the top quark is small enough that it fragments before it decays [52] (figure 4-4). This model is based on the observation that a heavy quark does not have to give up much energy to pick up a light quark travelling at the same velocity. Consequently, heavy quarks should fragment into heavy hadrons with large z. This is described by a fragmentation function of the form

$$D(z)^h = \frac{K}{z(1 - \frac{1}{z} - \frac{\epsilon_q}{1-z})^2}$$

K is a normalization constant. ϵ_q is 0.8 GeV^2/m_q^2 for charm and 0.5 GeV^2/m_q^2 for top and bottom. Figure 4-5 shows the function for u,c,t quarks.

Independent fragmentation describes the fast hadrons in a jet, but violates energy-momentum and flavor conservation. To restore energy-momentum conservation the hadrons are boosted to the rest frame of the fragmented jets, the three-

momenta are rescaled by a common factor, and the energies are recalculated. After fragmentation the final stage in the ISAJET generation is to add beam jets using a modified scheme that describes beam jets in minimum bias data [61]. The modification is to take account of the fact that the spectators interact more in hard scatter events.

We generate a large number of Monte Carlo data sets in order to cover the possible m_{H^+}, m_t combinations. However, before calculating the expected number of events we describe the systematic errors associated with this calculation.

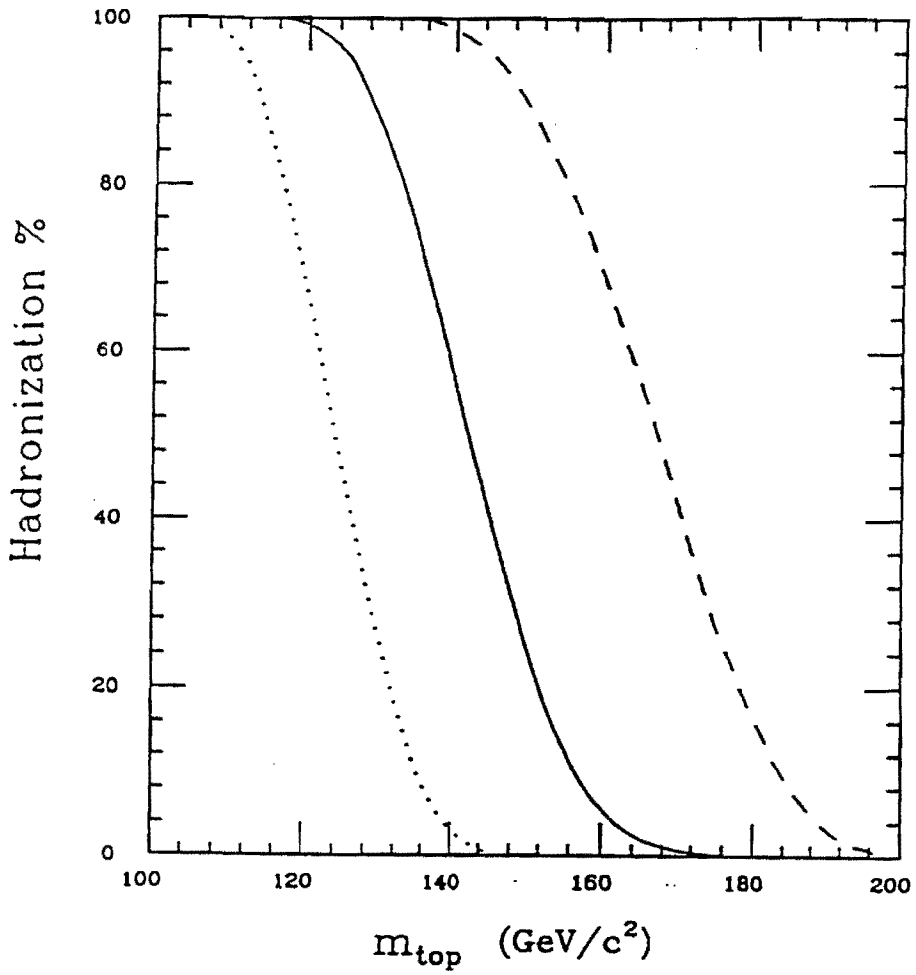

Figure 4-4: The percentage of the $t\bar{t}$ cross section at 1.8 TeV which fragments before the top decays as a function of m_t Solid line: Hadronization scale Λ^{-1} = 1 fm. Dotted line: Λ^{-1} = 0.5 fm. Dashed line: Λ^{-1} = 1 fm.

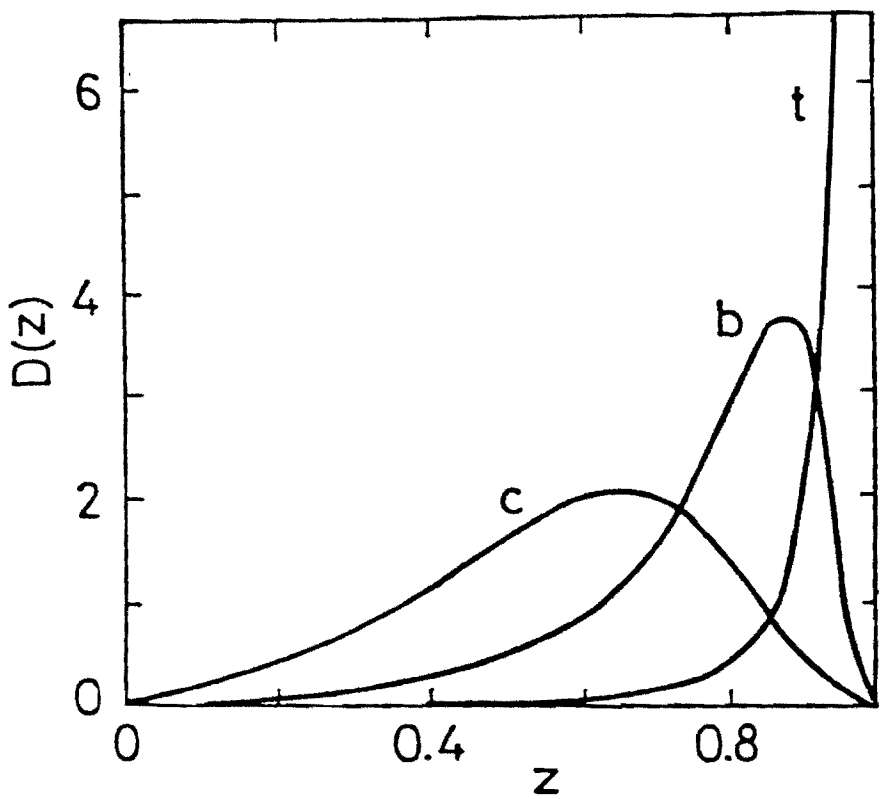

Figure 4-5: The Peterson fragmentation fraction $D(z)^h$ for c,b,t quarks

4.3 Systematic errors in N_{expect}

There are several systematic errors in the estimation of the expected number of events. The systematics are in general a function of $m_{H^+}, m_t, Br(H^+ \rightarrow \tau\nu_\tau)$. We will quantify the errors as a percentage of N_{expect}. The systematic errors are in general a function of m_{H^+}, m_t and so we quote the range of each error in this section. The values for each m_{H^+}, m_t case are tabulated at the end of this chapter.

4.3.1 Uncertainty in energy scale (E_{es})

There is a systematic uncertainty in the single pion response and an uncertainty in the jet response. The single pion response has been studied both in a pion testbeam and *in situ* using a single track trigger [57]. The jet response has been studied by comparing the momenta of tracks associated with a jet to the calorimeter response [68]. The uncertainty is in relating the generated parton E_T to the reconstructed E_T. This has several components; the single pion, electron and photon response; fragmentation tuning; the underlying event leaking into the jet cone; leakage through cracks in the detector. When these uncertainties are convoluted into our Monte Carlo they affect the E_T of jets and taus and also the $\not{E}_T$ and combine to give a total uncertainty of 7-14 %.

4.3.2 Modeling of gluon radiation (E_{gl})

Since there are theoretical uncertainties that go into the modelling of initial and final state radiation in ISAJET we need to understand whether the clusters required in addition to the tau derive from b's, and unidentified tau or gluon radiation. Accordingly we recompute the acceptance using only clusters that are tagged as taus or b's. The difference in acceptance is is typically 10-30 %. We believe that the exact probability of gluon radiation lies between zero and the value used in ISAJET. However, we are unable estimate this probability with any certainty. A reasonably conservative approach is to assume that the probability is half the value used in ISAJET and that the uncertainty is comparable. We therefore reduce the acceptance by half difference ie. 5-15 % and then set the systematic at half the

difference 5-15 % [69]. This systematic is most significant when $m_t - m_{H^+}$ is small since the b quark then has low P_T. This means that the jet requirement $E_T > 12$ GeV is more often satisfied by a gluon jet.

4.3.3 Uncertainty in tau branching ratio (E_{br})

The measured tau branching ratios are listed in section 3.5. Each measurement has some uncertainty and this can translate into an uncertainty in the overall acceptance. For example, suppose that there is a particular mode with a branching ratio of 20±2 %. We now compute our overall acceptance and find that in fact it is only this mode that passes our cuts. The uncertainty in the expected number of events, expressed as a percentage of the total number of expected events would then be 2/20 = 10 %. We have quoted all the acceptances and efficiencies after summing over all the decay modes of the tau rather than tabulate for each particular mode. It turns out that many modes contribute and so the systematic from the uncertainties in the measured branching ratios is rather complicated. To estimate the systematic we first generate a large sample of $t \rightarrow H^+b$ events, so that there are many events of each particular mode. We then pick a finite subset of these events (10,000) according to a branching ratio table and compute the overall acceptance. This process is repeated many times with a different branching ratio table each time. The branching ratio table is selected by fluctuating each mode with a Gaussian random number. The width of the Gaussian is the quoted error on the measured branching ratio. There is a slight complication in that the sum of the branching ratios generated by this procedure is not in general 1.0. In this case the remainder is divided up according to current branching ratio numbers and added to each mode (i.e the remainder is weighted by mode). After this procedure is repeated many times we end up with a Gaussian distribution of the overall acceptance. We use the width of this distribution as the systematic error. The overall systematic is estimated to be 4-6 %.

4.3.4 Monte Carlo statistics (E_{mc})

Since each of our Monte Carlo data sample is a finite size there is a statistical uncertainty in the computation of acceptances. We have used a data set of 10000

events for each (m_{H^+}, m_t) and this results in a 5 % uncertainty.

4.3.5 Uncertainty in trigger efficiency (E_{tr})

There is a systematic uncertainty in the trigger efficiency of 5-7 % which is described in detail in section 3.3.

4.3.6 Uncertainty in integrated luminosity (E_{lu})

There is a 7 % uncertainty in the integrated luminosity.

4.3.7 Uncertainty in Peterson fragmentation parameter

The Peterson fragmentation function parameter (described in section 4.2) has been varied from $0.5/\mathcal{M}_T^2$ to $1.5/\mathcal{M}_T^2$ [69] and the acceptance changes by 1 %.

4.3.8 Uncertainty in underlying event modeling

Since we require there to be no tracks in a cone about the tau cluster the presence of tracks from the underlying event would decrease the acceptance. We take a sample of 200,000 minimum bias events and compute the probability of a track of a certain P_T being in a unit solid angle as a function of pseudorapidity. This probability table is then convoluted into our acceptance calculation to give an uncertainty of < 1 %. This systematic is negligible as we would expect since the track thresholds in the tau algorithm have been chosen so that the probability of an underlying event track being in the track cones is < 1 %.

4.4 N_{expect} for different m_{H^+}, m_t for $Br(H^+ \rightarrow \tau\nu_\tau) = 1.0$, $Br(t \rightarrow H^+b) = 1.0$

The expect number of events with errors is given in table 4.2. The total integrated luminosity of the data set collected with the $\not{E}_T$ trigger used in this analysis is

$\int Ldt = 4.1 \pm 0.3$ pb^{-1}. The systematic errors are added in quadrature. The total systematic error is convoluted with the Poisson statistical error to give a total error that is typically 25-30 %.

4.5 N_{expect} for different m_{H^+}, m_t for $Br(H^+ \rightarrow \tau\nu_\tau) < 1.0$, $Br(t \rightarrow H^+b) < 1.0$

If $Br(t \rightarrow H^+b) < 1.0$ then we have three possible final states.

1. $p\bar{p} \rightarrow t\bar{t} \rightarrow H^+H^-b\bar{b}$
2. $p\bar{p} \rightarrow t\bar{t} \rightarrow H^+W^-b\bar{b}$
3. $p\bar{p} \rightarrow t\bar{t} \rightarrow W^+W^-b\bar{b}$

Suppose that $Br(t \rightarrow H^+b) = Y$ then the fraction of the total branching ratio for each of the above is

1. $Br(HH) = Y^2$
2. $Br(HW) = 2Y(1 - Y)$
3. $Br(WW) = (1 - Y)^2$

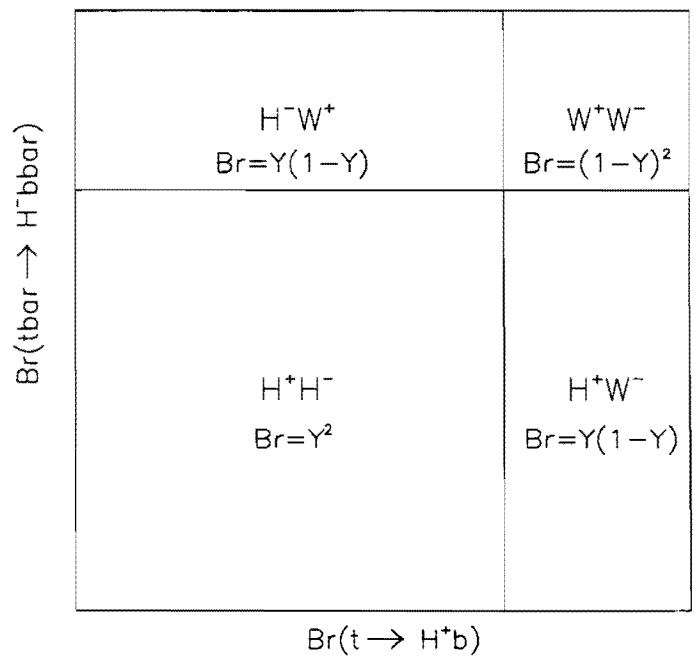

Figure 4-6: Schematic of the total $t\bar{t}$ branching ratio in the case $Br(t \to H^+b) = Y$. The areas represent the fraction of the total $t\bar{t}$ branching ratio for H^+H^-, H^+W^-, H^-W^+, W^+W^-

This means that if we compute the acceptance for each of the three cases $\varepsilon_{HH}, \varepsilon_{HW}, \varepsilon_{WW}$ then the overall acceptance ε for $Br(t \to H^+b) = Y$.

$$\varepsilon = \varepsilon_{HH}.Y^2 + \varepsilon_{HW}.2Y(1-Y) + \varepsilon_{WW}.(1-Y)^2$$

However since $Br(W \to \tau\nu) = 1/9$ ε_{WW} is very small so

$$\varepsilon = \varepsilon_{HH}.Y^2 + \varepsilon_{HW}.2Y(1-Y)$$

If $Br(H^+ \to \tau\nu_\tau) < 1.0$ we now have five possible final states (excluding WW)

1. $p\bar{p} \to t\bar{t} \to H^+H^-b\bar{b} \to \tau\tau\nu\nu b\bar{b}$
2. $p\bar{p} \to t\bar{t} \to H^+H^-b\bar{b} \to \tau\nu cs b\bar{b}$
3. $p\bar{p} \to t\bar{t} \to H^+H^-b\bar{b} \to cscs b\bar{b}$

4. $p\bar{p} \rightarrow t\bar{t} \rightarrow H^+W^-b\bar{b} \rightarrow \tau\nu W^-b\bar{b}$

5. $p\bar{p} \rightarrow t\bar{t} \rightarrow H^+W^-b\bar{b} \rightarrow csW^-b\bar{b}$

If $Br(H^+ \rightarrow \tau\nu_\tau) = X$ then

1. $Br(\tau\tau) = Y^2.X^2$

2. $Br(\tau cs) = Y^2.2X(1-X)$

3. $Br(cscs) = Y^2.(1-X)^2$

4. $Br(\tau W) = 2Y(1-Y).X$

5. $Br(csW) = 2Y(1-Y).(1-X)$

This means that if we compute the acceptance for each of the three cases $\varepsilon_{\tau\tau}, \varepsilon_{\tau cs}, \varepsilon_{cscs}, \varepsilon_{\tau W}, \varepsilon_{csW}$ then the overall acceptance ε for $Br(t \rightarrow H^+b) = Y$. $Br(H^+ \rightarrow \tau\nu_\tau)$=X is

$$\begin{aligned} \varepsilon \;=\; & \varepsilon_{\tau\tau}.Y^2.X^2 & + \\ & \varepsilon_{\tau cs}.Y^2.2X(1-X) & + \\ & \varepsilon_{cscs}.Y^2.(1-X)^2 & + \\ & \varepsilon_{\tau W}.2Y(1-Y).X & + \\ & \varepsilon_{csW}.2Y(1-Y).(1-X) & \end{aligned}$$

Since we have no sensitivity to a multijet final state ε_{cscs} =0.0 Also $Br(W \rightarrow \tau\nu) = 1/9$ so ε_{csW} =0.0 so the final acceptance reduces to

$$\varepsilon = \varepsilon_{\tau\tau}.Y^2.X^2 + \varepsilon_{\tau cs}.Y^2.2X(1-X) + \varepsilon_{\tau W}.2Y(1-Y).X \tag{4.1}$$

We therefore need three Monte Carlo data sets corresponding to cases 1,2 and 4 above. Tables 4.2, 4.3, 4.4 give the acceptances and errors for each case respectively. The expected number of of events can then be computed for the most general case using these tables and equation 4.1.

$$\begin{aligned} \varepsilon.\int Ldt.\sigma \;&=\; (N_{\tau\tau} \pm N^{err}_{\tau\tau}) + (N_{\tau cs} \pm N^{err}_{\tau cs}) + (N_{\tau W} \pm N^{err}_{\tau W}) \\ &=\; N \pm N^{err} \end{aligned}$$

where

$$N^{err} = \sqrt{(N^{err}_{\tau\tau})^2 + (N^{err}_{\tau cs})^2 + (N^{err}_{\tau W})^2}$$

Note that the highest acceptance is $\varepsilon_{\tau\tau}$ while $\varepsilon_{\tau W} \sim \frac{2}{3}\varepsilon_{\tau\tau}$ and $\varepsilon_{\tau cs} \sim \frac{1}{3}\varepsilon_{\tau\tau}$. This arises because of the decreased number of taus in the two latter cases and the fact that jets from H have lower E_T than from W since $m_{H^+} < m_{W^+}$ and therefore are less likely to satisfy the jet E_T requirements. The much lower efficiency $\varepsilon_{\tau cs}$ implies that the sensitivity of of the search will decrease rapidly as $Br(H^+ \to \tau\nu_\tau)$ decreases.

m_t GeV	m_{H^+} GeV	X pb	$\epsilon_{\tau\tau}$ %	N	MC	E_{st} %	E_{es} %	E_{gl} %	E_{br} %	E_{mc} %	E_{tr} %	E_{lm} %	E_{to} %
85	80	168	6.5	44±11	10000	15	7	15	2	3	6	7	24
85	75	168	5.6	38±9	10000	16	9	13	2	4	5	7	24
85	70	168	4.9	34±8	6816	17	10	10	4	5	7	7	25
85	65	168	4.6	32±8	10000	18	9	7	4	4	6	7	24
85	60	168	4.1	28±7	10000	19	8	5	3	5	5	7	24
85	55	168	3.8	26±7	10000	19	11	5	4	5	4	7	25
85	50	168	3.4	24±6	10000	21	9	5	3	5	5	7	25
85	45	168	3.1	21±6	5756	22	10	5	7	7	2	7	27
80	75	229	5.7	54±13	5000	14	5	15	5	5	5	7	24
80	70	229	4.8	45±11	10000	15	10	13	4	4	5	7	24
80	65	229	4.3	41±10	10000	16	10	10	2	4	6	7	23
80	60	229	3.9	36±9	5000	17	13	7	5	7	7	7	26
80	55	229	3.6	34±8	8352	17	10	5	2	6	5	7	23
80	50	229	3.1	29±7	10000	18	8	5	0	5	6	7	23
80	45	229	2.4	23±6	9418	21	9	5	6	6	5	7	26
75	70	323	4.6	60±15	10000	13	9	15	3	4	6	7	24
75	65	323	4.0	53±13	9591	14	12	13	2	5	7	7	25
75	60	323	3.7	49±12	10000	14	13	10	2	5	7	7	25
75	55	323	2.8	37±9	10000	17	11	7	7	6	6	7	25
75	50	323	2.9	38±9	7966	16	10	5	4	6	5	7	23
75	45	323	2.5	33±8	8713	17	9	5	4	6	7	7	23
70	60	457	3.2	60±14	10000	13	9	13	3	5	7	7	24
70	60	457	3.2	60±14	10000	13	9	13	3	5	7	7	24
70	55	457	2.5	48±11	10000	15	9	10	6	6	8	7	24
70	50	457	2.5	46±11	10000	15	13	7	3	6	9	7	24
70	45	457	2.0	37±9	10000	17	11	5	5	7	5	7	24
65	60	678	2.8	77±18	10000	11	9	15	2	5	7	7	24
65	55	678	2.6	71±18	10000	12	11	13	6	6	8	7	25
65	50	678	2.3	63±15	5000	13	8	10	6	9	9	7	24
65	45	678	2.0	54±13	9529	14	14	7	2	7	5	7	23
60	55	1005	2.4	97±24	10000	10	12	15	3	6	5	7	24
60	50	1005	1.7	70±18	10000	12	12	13	4	7	9	7	26
60	45	1005	1.6	66±18	8002	12	17	10	3	8	7	7	27
55	50	1587	1.5	97±25	10000	10	13	15	3	7	7	7	26
55	45	1587	1.3	84±21	7602	11	11	13	4	9	8	7	25

Table 4.2: Acceptances and errors for $p\bar{p} \rightarrow t\bar{t} \rightarrow H^+H^-b\bar{b} \rightarrow \tau^+\tau^-b\bar{b}$

m_t GeV	m_{H^+} GeV	X pb	$\epsilon_{\tau W}$ %	N	MC	E_{st} %	E_{es} %	E_{gl} %	E_{br} %	E_{mc} %	E_{tr} %	E_{lm} %	E_{to} %
85	80	168	3.9	27± 6	5000	19	5	8	5	7	3	7	24
85	75	168	3.0	21± 6	5000	22	9	7	5	8	4	7	27
85	70	168	2.7	19± 5	5000	23	11	5	5	8	2	7	29
85	65	168	2.3	19± 5	5000	23	11	5	5	8	2	7	29
85	60	168	1.9	13± 4	5000	28	13	3	5	10	4	7	34
85	55	168	1.6	11± 4	5000	30	5	3	5	11	6	7	34
85	50	168	1.4	10± 4	5000	32	9	3	5	12	2	7	36
85	45	168	1.4	10± 4	5000	32	9	3	5	12	9	7	38
80	75	229	3.0	28± 7	5000	19	9	8	5	8	3	7	26
80	70	229	2.2	21± 6	5000	22	5	7	5	9	3	7	27
80	65	229	2.0	18± 5	5000	23	6	5	5	10	3	7	28
80	60	229	1.8	17± 5	5000	25	6	4	5	10	7	7	30
80	55	229	1.6	17± 5	5000	25	6	4	5	10	7	7	30
80	50	229	1.4	17± 5	5000	25	6	4	5	10	7	7	30
80	45	229	1.2	17± 5	5000	25	6	4	5	10	7	7	30
75	70	323	2.4	32± 8	5000	18	1	8	5	9	7	7	24
75	65	323	2.0	32± 8	5000	18	1	8	5	9	7	7	24
75	60	323	1.6	21± 6	5000	22	13	5	5	11	7	7	30
75	55	323	1.4	14± 5	5000	27	11	4	5	13	5	7	34
75	50	323	1.2	14± 5	5000	27	11	4	5	13	5	7	34
75	45	323	1.0	14± 5	5000	27	11	4	5	13	5	7	99
70	65	457	2.0	37±11	5000	17	16	8	5	10	9	7	29
70	60	457	1.9	35± 8	5000	17	7	7	5	10	4	7	24
70	55	457	1.5	35± 8	5000	17	7	7	5	10	4	7	24
70	50	457	1.0	19± 6	5000	23	7	4	5	14	7	7	30
70	45	457	1.0	19± 6	5000	23	7	4	5	14	7	7	30
65	60	678	1.7	47±12	5000	15	14	8	5	10	8	7	26
65	55	678	1.4	47±12	5000	15	14	8	5	10	8	7	26
65	50	678	1.1	47±12	5000	15	14	8	5	10	8	7	26
65	45	678	0.9	47±12	5000	15	14	8	5	10	8	7	26
60	55	1005	1.2	48±14	5000	14	17	8	5	12	6	7	28
60	50	1005	1.0	40±10	5000	16	9	7	5	14	3	7	26
60	45	1005	0.9	40±10	5000	16	9	7	5	14	3	7	26
55	50	1587	0.9	56±20	5000	13	17	8	5	15	7	7	36
55	45	1587	0.7	56±20	5000	13	17	8	5	15	7	7	36

Table 4.3: Acceptances and errors for $p\bar{p} \to t\bar{t} \to H^+W^-b\bar{b} \to \tau^+W^-b\bar{b}$

m_t GeV	m_{H^+} GeV	X pb	$\epsilon_{\tau cs}$ %	N	MC	E_{st} %	E_{cs} %	E_{gl} %	E_{br} %	E_{mc} %	E_{tr} %	E_{lm} %	E_{to} %
85	80	168	2.8	19± 6	2500	23	9	8	5	11	4	7	30
85	75	168	2.4	16± 6	2500	25	23	7	5	12	2	7	38
85	70	168	1.9	13± 5	2500	27	13	5	5	14	1	7	35
85	65	168	1.9	13± 5	2500	28	13	4	5	14	7	7	36
85	60	168	1.4	13± 5	2500	28	13	4	5	14	7	7	36
85	55	168	0.9	6± 3	2500	40	17	3	5	21	4	7	49
85	50	168	0.8	6± 3	2500	42	21	3	5	22	7	7	53
85	45	168	0.8	5± 3	2500	43	6	3	5	22	7	7	50
80	75	229	2.4	22± 7	2500	21	15	8	5	12	4	7	31
80	70	229	1.8	17± 5	2500	24	9	7	5	14	3	7	31
80	65	229	1.9	18± 6	1230	23	10	5	5	20	7	7	34
80	60	229	1.7	16± 5	2500	25	6	4	5	15	1	7	31
80	55	229	0.8	8± 4	2500	36	14	3	5	22	8	7	46
80	50	229	0.6	5± 3	2500	44	9	3	5	26	9	7	53
80	45	229	0.4	4± 2	2500	53	6	3	5	32	8	7	63
75	70	323	1.7	22± 6	2500	21	4	8	5	15	4	7	29
75	65	323	1.9	25± 7	2500	20	12	7	5	14	1	7	29
75	60	323	1.4	19± 6	2500	23	14	5	5	16	9	7	35
75	55	323	0.8	10± 4	2500	31	10	4	5	22	10	7	42
75	50	323	0.6	8± 4	2500	35	25	3	5	25	13	7	52
75	45	323	0.4	8± 4	2500	35	25	3	5	25	13	7	52
70	65	457	1.9	36±11	2500	17	17	8	5	14	3	7	30
70	60	457	1.2	22± 8	2500	21	18	7	5	18	5	7	35
70	55	457	0.6	11± 5	2500	30	4	5	5	25	13	7	42
70	50	457	0.6	11± 4	5000	31	17	4	5	18	1	7	41
70	45	457	0.4	8± 4	2500	35	19	3	5	30	9	7	52
65	60	678	1.4	39±10	2500	16	2	8	5	16	2	7	25
65	55	678	1.1	31± 9	2500	18	10	7	5	18	3	7	30
65	50	678	0.5	14± 6	2500	27	15	5	5	27	12	7	44
65	45	678	0.4	11± 6	2500	30	23	4	5	31	8	7	51
60	55	1005	1.4	59±16	2500	13	11	8	5	16	9	7	27
60	50	1005	0.8	34±13	2500	17	23	7	5	21	9	7	39
60	45	1005	0.2	9± 5	2500	33	11	5	5	41	4	7	55
55	50	1587	0.7	47±15	2500	15	14	8	5	23	2	7	32
55	45	1587	0.4	25±11	2500	20	15	7	5	31	11	7	43

Table 4.4: Acceptances and errors for $p\bar{p} \to t\bar{t} \to H^+H^-b\bar{b} \to \tau c\bar{s}b\bar{b}$

Chapter 5

Results

In chapter 4 we tabulated the expected number of events for different cases of $m_{H^+}, m_t, Br(H^+ \rightarrow \tau\nu_\tau)$ using the signature defined in chapter 3. The signal variable used is the number of tracks associated with the tau cluster (N_{track}) and we used it to demonstrate a $W \rightarrow \tau\nu$ signature by virtue of the one and three prong surplus (see figure 3-23) and show consistency with lepton universality. Recalling the signature definition for top to charged Higgs events:

$$\text{one central } \tau \ (E_T > 15 \text{ GeV}) + \not{E}_T + \geq 1 \text{ jet } (E_T > 12 \text{ GeV})$$

We apply this definition to the data and first show the signal plot (N_{track}) with backgrounds included and then describe and subtract each background.

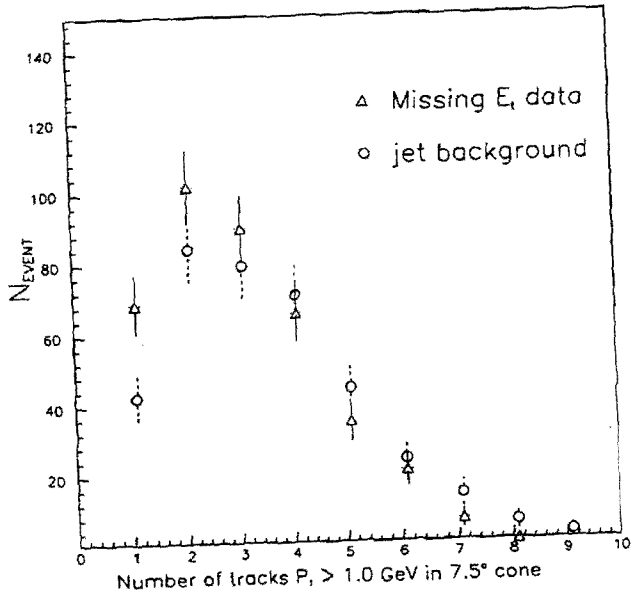

Figure 5-1: The number of tracks with $P_T > 1.0$ GeV in 7.5° cone. The distributions for the $\tau + \not{E}_T + \geq 1$ jet data sample and the normalized QCD background sample are shown.

5.1 Signal with background

Figure 5-1 shows N_{track} for the tau candidates in events which satisfy the above criteria. There are 391 events, with a large QCD background from multijet events in which one jet is mismeasured to give spurious $\not{E}_T$ and another jet fragments to look like a hadronic tau. There are also a small amount of residual electrons due to the fact that our electron removal cut was only 98.0 ± 1.5 % efficient. In addition we expect a background from $W \rightarrow \tau\nu$ + jet events in which the jet derives from initial state radiation and the τ and ν satisfy the τ definition and $\not{E}_T$ requirements respectively.

5.2 Subtraction of QCD and electron background

The distribution for a normalized QCD background is also shown in the figure. The normalization and choice of background data set is described in section 3.6. A one prong surplus can be seen. We subtract the QCD background as before to leave 41 $\pm$ 16 events. To estimate the number of residual electrons we remove the electron cut and this adds an additional 229 events. Since the electron removal cut is 98 $\pm$ 1.5 % efficient this implies that we have 5 $\pm$ 2 residual electrons. We thus have 36 $\pm$ 16 $\tau + \not{E}_T$+jet events.

5.3 Estimation of vector boson background

There are two vector boson backgrounds

- $Z \rightarrow \tau\tau$+ jets
- W $\rightarrow \tau\nu$+ jets

The first we can estimate using ISAJET which is the standard simulation for z + jet events. With a sample of 5000 events we used exactly the same analysis path as described previously for the data sample and estimate a contribution of 3 $\pm$ 1 events. The second is more problematic because of the theoretical uncertainty in the absolute value of the cross section for W + jet production. We can avoid this problem by recognizing that in our $\not{E}_T$ data set we also have W $\rightarrow$ eν + jets. Since lepton universality is well verified [57] the cross section for W $\rightarrow \tau\nu$ + jets is the same as for W $\rightarrow$ eν + jets. This means that we can normalize our W $\rightarrow \tau\nu$ + jets estimate to the measured W $\rightarrow$ eν + jets by estimating the ratio of acceptances for W $\rightarrow \tau\nu$ + jets:W $\rightarrow$ eν + jets. The absolute cross section cancels, and since electrons are very well understood in the CDF detector, we have the advantage of normalizing to a reliable data set. Additionally, the ratio of acceptances (# W $\rightarrow$ eν + jets

events):(# W $\rightarrow \tau\nu$ + jets events) will be determined by the kinematics of the tau decay and by detector effects and both of these can be well modeled by a Monte Carlo. We will use the VECBOS [70] Monte Carlo, which has been demonstrated to model W $\rightarrow e\nu$ + jet events well [71], to create two data sets. The first will be a W $\rightarrow e\nu$ + jets data set and in the second we will replace the electron by a tau . The W + jet Monte Carlo data sets have been created with the following criteria

- Lepton $P_T > 12$ GeV , $\eta < 1.2$
- Jet $P_T > 8$ GeV , $\eta < 3.5$

We pass the two Monte Carlo data sets through the same analysis path as the data except that for the W $\rightarrow e\nu$ + jets data set we require a good central electron $E_T > 15$ GeV using the standard quality cuts as defined in appendix A. We find that the ratio of acceptances is

$$\frac{A.\epsilon(W\rightarrow\tau\nu+\text{jets})}{A.\epsilon(W\rightarrow\tau\nu+\text{jets})} = 0.21 \pm 0.025$$

The error quoted is purely statistical. We must consider the systematic error associated with this ratio. The only systematics we need to worry about are those that affect the tau but not the electron efficiencies since these do not cancel. The first is the energy scale. This systematic is described in section 4.3.1 and causes an uncertainty in the ratio of 0.024. There is also an uncertainty in the measured tau decay branching ratios described in section 4.3.3. This systematic causes an uncertainty in the ratio of 0.014. We then have three errors that we must combine, the statistical error from the finite size of the Monte Carlo sample, the energy scale and the branching ratio. We combine these errors, as percentage errors in the ratio, in quadrature. This then results in a ratio

$$\frac{A.\epsilon(W\rightarrow\tau\nu+\text{jets})}{A.\epsilon(W\rightarrow\tau\nu+\text{jets})} = 0.21 \pm 0.035$$

To demonstrate that VECBOS models W $\rightarrow$ eν+ jet events well we compare the transverse mass of the data with simulated W $\rightarrow$ eν+ jet events. The transverse mass $m_{tran}$is defined as

$$m_{tran} = \sqrt{2.E_t^e.\not{E}_T(\cos\Delta\phi)}$$

E_t^e is the transverse energy of the electron. $\Delta\phi$ is the angle between the electron and the $\not{E}_T$ vector in the ϕ plane.

Figure 5-2 shows the transverse mass for W $\rightarrow$ eν + jet data where we have made exactly the same cuts as for the tau + $\not{E}_T$ + jets except that we have required a good electron (see appendix A) rather than a tau. Also shown is the VECBOS Monte Carlo data set where the same cuts have been made. The agreement is very good.

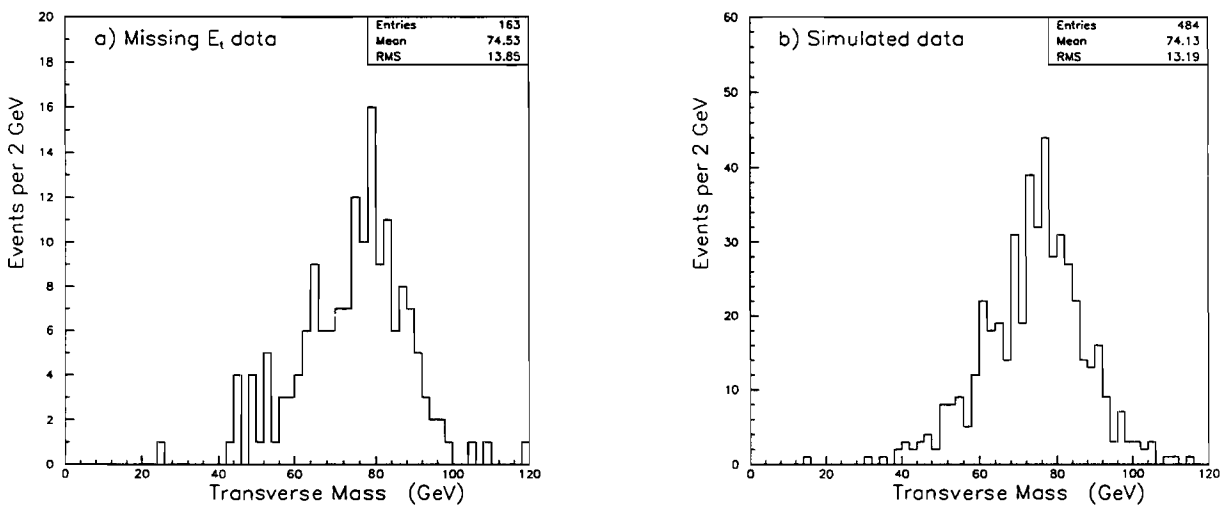

Figure 5-2: The transverse mass of e + jets in a) $\not{E}_T$data events and b) simulated (VECBOS) W $\rightarrow$ eν + jets events

Having now estimated the ratio of acceptances we now need to measure the number of W $\rightarrow$ eν + jets events in the data. Again we make the same analysis cuts as for the τ + $\not{E}_T$+ $\geq$ jet data set, except that we require a good electron rather than a τ. However in this case we must subtract the backgrounds. There are four backgrounds; a QCD background in which a jet fragments to

fake an electron; a background from W $\rightarrow \tau\nu$ + jets, $\tau \rightarrow \nu\nu$; a background from $Z \rightarrow ee$ + jets in which one electron is mismeasured; a background from $Z \rightarrow \tau\tau$ in which one of the τs decays to an electron. . The QCD background is estimated by relaxing the isolation [55] to be 3 events. The background from W $\rightarrow \tau\nu \rightarrow e\nu\nu$ is estimated to be 2 events using a VECBOS Monte Carlo data set. The $Z \rightarrow ee$ background is 1 event and the $Z \rightarrow \tau\tau$ background is 1 event using ISAJET. After subtraction of these backgrounds we are left with 156 W $\rightarrow e\nu$ + jets events. We then multiply this number by the ratio of acceptances to estimate a W $\rightarrow \tau\nu$ + jets background of 33$\pm$7 events.

5.4 Final result

The 36 $\pm$ 16 events can be fully accounted for by vector boson decays involving τ's. After subtracting this contribution we are left with 0 $\pm$ 17 event candidates for the process $p\bar{p} \rightarrow t\bar{t} \rightarrow H^+H^-b\bar{b}$ in which one or both of the charged Higgs decays to a τ.

Chapter 6

Limits

We have observed 0 ± 17 candidate events for a top to charged higgs decay. In chapter 4 we tabulated the expected number of events for different $m_{H^+}, m_t, Br(H^+ \rightarrow \tau\nu_\tau)$. We can now use these results to exclude regions of these parameter space. We first exclude regions in a model independent way, i.e in terms of branching ratios. Then we exclude regions for different versions of the two Higgs doublet model.

6.1 Model independent limits

In figure 6-1 the excluded regions for Br(t $\rightarrow$ H$^+$b)=1.0 and Br(H$^+$ $\rightarrow$ $\tau\nu_\tau$) =0.5,0.75,1.0 are shown. These limits are in terms of branching ratios and are therefore model independent. The sensitivity decreases as the top mass increases because of the diminished production cross section and also as the charged Higgs mass decreases due to the lower neutrino and tau transverse energies.

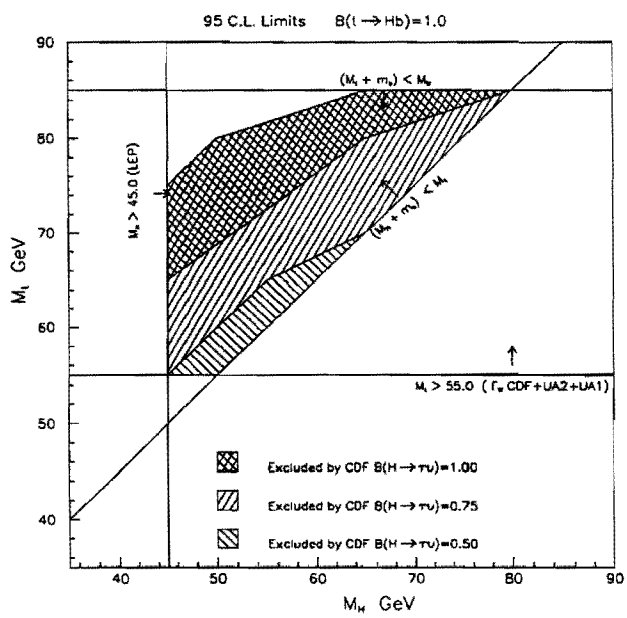

Figure 6-1: The excluded regions for Br(t $\rightarrow$ H$^+$b) = 1.0, Br(H$^+$ $\rightarrow$ $\tau\nu_\tau$) =0.5, 0.75, 1.0 in the (m_{H^+}, m_t) plane at 95 % Confidence Limit from CDF data

6.2 Limits for the two Higgs doublet model

In chapter 1 we described the Two Higgs Doublet Model in which both $Br(H^+ \rightarrow \tau\nu_\tau)$ and to a lessor extent $Br(t \rightarrow H^+b)$ are functions of $\tan\beta$. The explicit dependence on $\tan\beta$ differed according to how the fermions coupled to the Higgs doublets and led to four possibilities which we labelled as Models I,II,III,IV. It was pointed out that we will have different sensitivities to the different models. We now interpret our results for each of these different cases

6.2.1 Model I

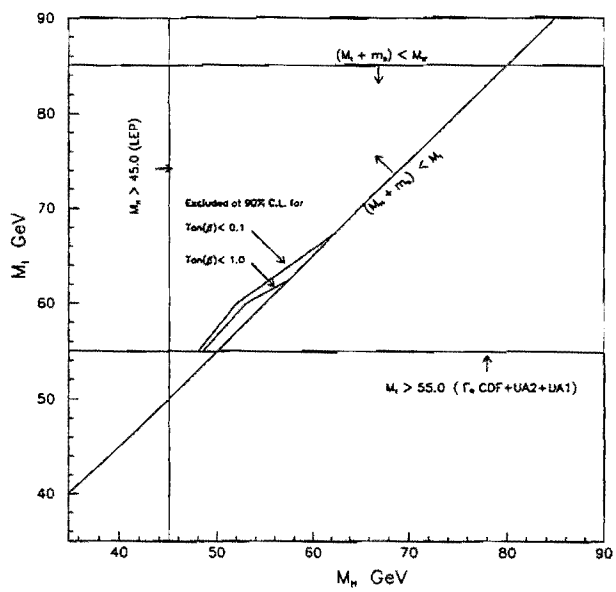

Figure 6-2: The excluded regions for model I in terms of $\tan\beta$ for the (m_{H^+}, m_t) plane of the two Higgs doublet model at 90 % confidence limit

Figure 6-2 shows the excluded regions for model I. We have very little sensitivity. This can be understood by recognizing that for this case $Br(H^+ \rightarrow \tau\nu_\tau)$ = 0.3. The model independent limits (figure 6-1) show that we are very insensitive for $Br(H^+ \rightarrow \tau\nu_\tau) < 0.5$. Note also that the model I limits are 90 % C.L whereas figure 6-1 are 95 % C.L.

6.2.2 Model II

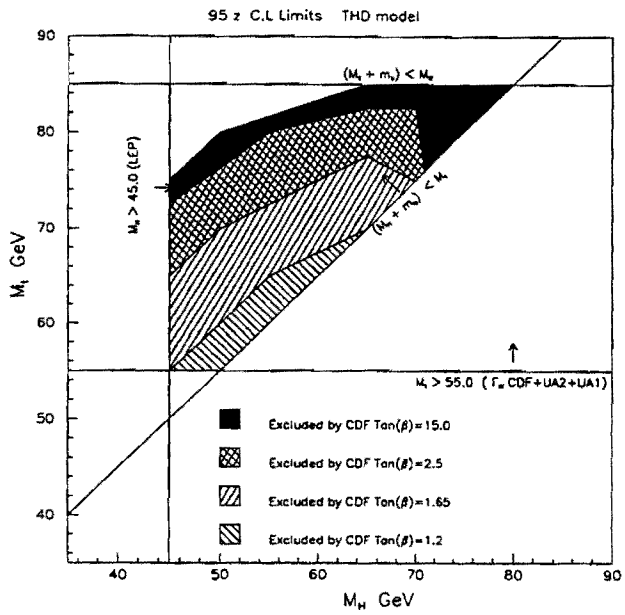

Figure 6-3: The excluded regions for model II in terms of tanβ for the (m_{H^+}, m_t) plane of the two Higgs doublet model at 95 % confidence limit

The limits for Model II are quite restrictive and are a substantial improvement on UA1 and UA2 who both test this case. In this model $Br(t \rightarrow H^+b) \approx 1.0$ for all tanβ except in the region $m_t \approx m_{W^+}$ in which case it is only true for large tanβ (> 10.0). This is because resonant production of W in the decay $Br(t \rightarrow W^+b)$ becomes competitive with the H mediated decay in this region. Figure 6-3 shows the excluded regions for this model for the cases tanβ = 1.2,1.65,2.5,15.0 which corresponds to $Br(H^+ \rightarrow \tau\nu_\tau)$ = 0.5,0.75,0.95,1.0 respectively.

6.2.3 Model III

The limits are exactly the same as for Model I 6-2 because the only region where both $Br(H^+ \rightarrow \tau\nu_\tau)$ and $Br(t \rightarrow H^+b)$ are significant is tan$\beta < 1.0$ (see chapter 1) and in this region both $Br(H^+ \rightarrow \tau\nu_\tau)$ and $Br(t \rightarrow H^+b)$ are the

same in model I and III.

6.2.4 Model IV

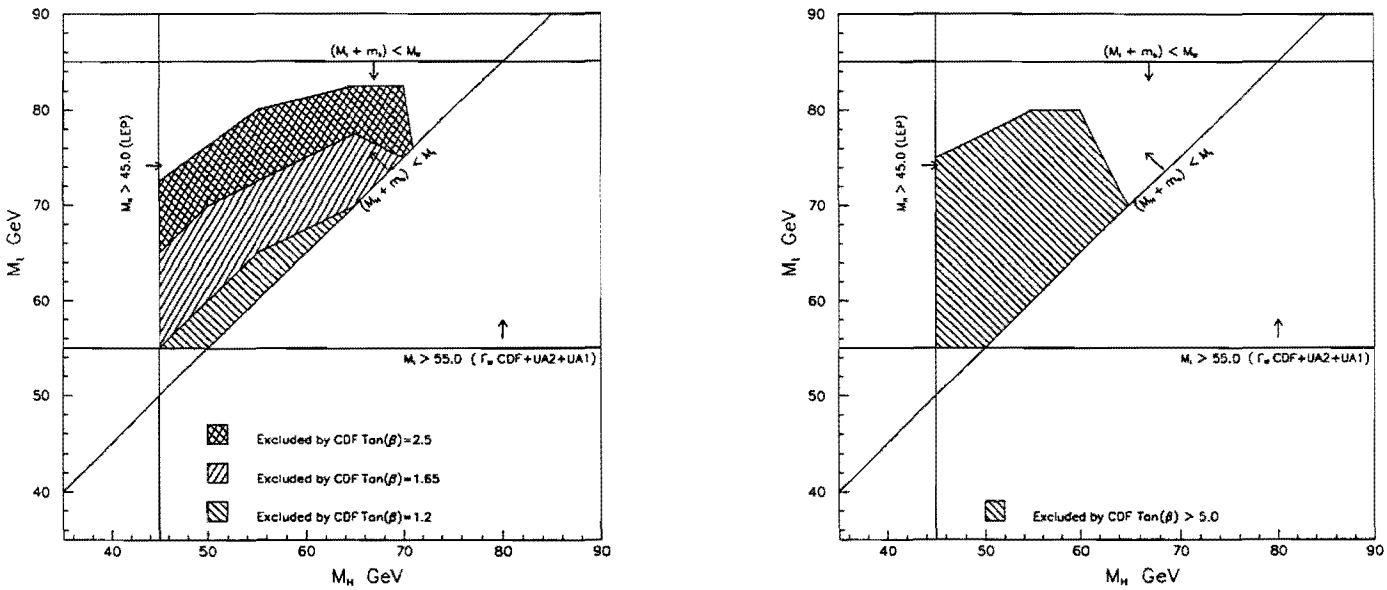

Figure 6-4: The excluded regions of the (m_t, m_{H^+}) plane in Model IV for $\tan\beta$ = 1.2, 1.65, 2.5 and $\tan\beta > 5.0$ at 95 % confidence limit. The sensitivity is a maximum for $\tan\beta$ =2.5 and then decreases to a constant value for $\tan\beta > 5.0$

Figure 6-4 shows the excluded regions for Model IV. The sensitivity rises to a maximum at $\tan\beta = 2.5$ and then declines to a constant for $\tan\beta > 5.0$ This is because $Br(H^+ \rightarrow \tau\nu_\tau)$ rises as $\tan\beta$ increases (see figure 1-6) while $Br(t \rightarrow H^+b)$ decreases (see figure 1-12).

Chapter 7

Conclusions

We have searched for $p\bar{p} \rightarrow t\bar{t}X \rightarrow H^+H^-b\bar{b}X$, where at least one the charged Higgs decays to a tau, in $p\bar{p}$ collisions at $\sqrt{s} = 1.8$ TeV. We find no evidence for this decay in 4.1 pb^{-1} of data collected during 1988-89 at the CDF at the Fermilab Tevatron. We are able to exclude significant regions of the $m_{H^+}, m_t, Br(H^+ \rightarrow \tau\nu_\tau)$ parameter space and also to interpret these results in terms of the two Higgs doublet model.

Appendix A

Electron Cuts

- $E_T > 15$ GeV
- $|\eta| < 1.0$ FIDELE passed
- $E/P < 1.5$
- LSHR < 0.2
- HAD/EM $< 0.055 + 0.045.E/100.0$
- δX strip match < 1.5 cm
- δZ strip match < 3.0 cm
- $\chi^2 < 15.0$
- ISOL $= (E_T(0.4)$ -$E_T(\text{ELES}))/E_T(\text{ELES}) < 0.1$

Appendix B

$W \rightarrow \tau\nu$ analysis cuts

The cuts used in reference [57] to measure lepton universality are as follows

- $\not{E}_T$ trigger passed
- $\not{E}_T > 25$ GeV
- Leading cluster have
  1. $E_T > 15$ GeV
  2. $|\eta| < 2.4$
  3. $E_{T1}^{em}/E_T(EM + HAD)$ ¿ 0.05
- $\not{E}_T/\sqrt{(\sum E_T)} > 2.4$
- $\Delta\phi$ between the highest E_T jet cluster and other jet clusters with $E_T >$ 5.0 GeV be $< 150^o$
- One tau with the tau defined as follows.
  1. The algorithm begins with a track cluster requirement. Any track with $P_T > 5.0$ GeV is a seed track. Any tracks with $P_T > 1.0$ GeV within a 30° cone about the seed track are included in the cluster. A calorimeter cluster is defined as a region with 2 towers in ϕ by 6 towers in η about the seed track.

2. Require the tau cluster be in the central calorimeter and 15 GeV $< E_T <$ 55 GeV

3. Count tracks with $P_T > 1.0$ GeV in 10° cone about the seed track. Use as signal variable.

4. Require no tracks $P_T > 1.0$ GeV in 10° - 30° cone about seed track. Use as isolation variable.

5. Reconstruct π^o energy in tower as follows:

$$E_T(\pi^o) = E_T(EM + HAD) - \sum_{tracks} < E_T >$$

   where $\sum_{tracks} < E_T >$ is the estimated energy deposit of charged pions in the EM calorimeter. The $E_T(\pi^o)$ is then summed with total momentum of the tracks in the 10° cone to form a $\sum P_T$. then require

   (a) $\sum P_T > 17.5$ for 1 prong tau clusters

   (b) $\sum P_T > 20.0$ for 2 prong tau clusters

   (c) $\sum P_T > 22.5$ for 3 prong tau clusters

6. Electrons are removed by the logical or of two requirements

   (a) The tau cluster HAD/EM ratio $< .06$ and the ΔZ between the electron cluster track and the best strip chamber track be less than 5 cm. If there are two electron clusters then the ΔZ must be satisfied by at least one of them.

   (b) The electron cluster E/P between $0.5 < E/P < 1.5$

Bibliography

[1] P. Tipton *et al.*, CDF Collaboration, Proceedings of the XVI International Symposium on Lepton Photon Interactions, Ithaca, New York, 1993.

[2] G. Kane Proceedings of the eighteenth SLAC summer institute on Particle Physics P.123 using results from CELLO,AMY,JADE and TASO. 1990

G. Kane and M. Peskin, Nucl. Phys. B **195**, 29 (1982)

[3] UA1 Collaboration, C. Albajar *et al.*, Report No. CERN-PPE/91-54, 1991 (unpublished)

[4] C. Jarlskog, in Proceedings of XXVth international Conference on High Energy Physics, Singapore, 1990, edited by K.K. Phua and Y. Yamaguchi (World Scientific, Singapore, 1991)

[5] D. Schaile and P.M. Zerwas, Phys. Rev. D **45**, 3262 (1992)

[6] J. Carter, in Proceedings of the Joint International Lepton-Photon Symposium and Europhysics Conference on High Energy Physics, Geneva, Switzerland, 1991, edited by S. Hegarty, K. Potter, and E. Quereigh.

[7] TASSO Collaboration, W Braunshweig *et al.*, Z. Phys. C **48**, 433 (1990)

[8] P. Wells, in Proceedings of the 4th International Symposim on Heavy Flavor Physics, Orsay, France, 1991.

[9] "Gauge Theories in Particle Physics" I. Aitchinson and A. Hey Published by Adam Hilger, Bristol UK (1984)

"Collider Physics" V. Barger and R. Phillips Addison Wesley, New York USA (1987)

"Electroweak Interactions" P. Renton Cambridge University Press, Cambridge UK (1990)

[10] "Results from the L3 experiment at LEP", L3 Collaboration, CERN-PPE/93-31, 1993

[11] F. Abe *et al.*, CDF Collaboration, Phys. Rev. D **43**, 2070 (1991)

[12] "The Higgs Hunters Guide" J. Gunion,H. Haber,G. Kane,S. Dawson Addison Wesley, New York USA (1990)

[13] S. Glashow and S. Weinberg, Phys. Rev. D **15**, 1958 (1977)

[14] H.E. Haber and G.L. Kane, Phys. Rep. **117**, 75 (1985)

[15] L. Susskind, Phys. Rev. D **20**, 2619 (1979)

[16] J. Wess and B. Zumino, Nucl. Phys. B **70**, 39 (1974)

[17] H. Georgi and S. Glashow, Phys. Rev. D **6**, 429 (1972)

[18] D. Toussaint, Phys. Rev. D **18**, 1626 (1978)

[19] V. Barger,J.L. Hewett and R.J.N. Phillips, Phys. Rev. D **41**, 3421 (1990)

[20] V. Barger and R. Phillips, Phys. Rev. D **41**, 884 (1990)

[21] ALEPH Collaboration, Phys. Rep. **216**, 253 (1992)

DELPHI Collaboration, P. Abreu *et al.*Phys. Lett. B **241**, 449 (1990)

L3 Collaboration, B. Adeva *et al.*Phys. Lett. B **294**, 457 (1992)

OPAL Collaboration, M. Akrawy *et al.*Phys. Lett. B **253**, 511 (1991)

[22] ARGUS collaboration, Phys. Lett. B **192**, 245 (1987)

[23] S. Glashow and E. Jenkins, Phys. Lett. B **196**, 223 (1987)

[24] C. Bernard *et al.*, Phys. Rev. D **38**, 3540 (1988)

[25] L. Chau and W Keung Phys. Rep. **95**, 1 (1983)

[26] Particle Data Group, G. P. Yost *et al.*, Phys. Lett. B **204**, 1 (1988)

[27] J. Hewett, Phys. Rev. Lett. **70**, 1045 (1993)

[28] B. Grinstein and P. Cho, Nucl. Phys. B **365**, 279 (1991)

[29] M. Battle, et al, CLEO Collaboration, *Proceedings of the joint Lepton-Photon and Europhysics International Conference on High Energy Physics*, Geneva, Switzerland, August, 1991.

[30] CDF Collaboration, F. Abe *et al.*, Phys. Rev. D 44, 29 (1991)
UA2 Collaboration, J. Alitti *et al.*, Phys. Lett. B **276**, 354 (1991)
UA1 Collaboration, C. Albajar *et al.*, Phys. Lett. B **253**, 503 (1991)

[31] UA1 Collaboration, C. Albajar *et al.*, Phys. Lett. B **280**, 137 (1992)

[32] UA1 Collaboration, C. Albajar *et al.*, Z. Phys. C **48**, 125 (1990)

[33] UA2 Collaboration, J. Alitti *et al.*, Phys. Lett. B **257**, 459 (1991)

[34] R. Foot, H. Lew, and G. C. Joshi, University of Melbourne Report No. UM-P-88/53, 1988 (unpublished)

[35] CDF Collaboration, F. Abe *et al.*, Nucl. Instrum. Methods **271**, 387 (1988)

[36] CDF Collaboration, F. Abe *et al.*, Nucl. Instrum. Methods **268**, 75 (1988)

[37] CDF Collaboration, F. Abe *et al.*, Nucl. Instrum. Methods **268**, 50 (1988)

[38] CDF Collaboration, F. Abe *et al.*, Nucl. Instrum. Methods **267**, 272 (1988)

[39] CDF Collaboration, F. Abe *et al.*, Nucl. Instrum. Methods **267**, 301 (1988)

[40] CDF Collaboration, F. Abe *et al.*, Nucl. Instrum. Methods **267**, 257 (1988)

[41] CDF Collaboration, F. Abe *et al.*, Nucl. Instrum. Methods **268**, 33 (1988)

[42] CDF Collaboration, F. Abe *et al.*, Nucl. Instrum. Methods **269**, 51 (1988)

CDF Collaboration, F. Abe *et al.*, Nucl. Instrum. Methods **269**, 63 (1988)

CDF Collaboration, F. Abe *et al.*, Nucl. Instrum. Methods **269**, 93 (1988)

[43] G. Drake *et al.*, Nucl. Instrum. Methods **269**, 68 (1988)

[44] E. Barsotti *et al.*, Nucl. Instrum. Methods **269**, 82 (1988)

[45] Peter Berge and Aseet Mukherjee, CDF collaboration, private communication

[46] David Brown PhD Thesis, Harvard University 1989.

[47] F.E. Paige and S. D. Protopopescu, Report No. BNL-38034, 1986 unpublished). We used version 6.36.

[48] B. K. Bullock, K. Hagiwara, A. D. Martin Phys. Rev. Lett. **67**, 3055 (1991).

[49] 607 1988 P. Nason, S. Dawson, and R. K. Ellis, Nucl. Phys. B **303**, 607 (1988)

[50] "Applications of perturbative QCD" page 243, R.D. Field, published by Addison-Wesley, New York 1989

[51] C. Peterson *et al.*, Phys. Rev. D **27**, 105 (1983)

[52] L.H. Orr and J.L. Rosner, Phys. Lett. B **246**, 221 (1990)

[53] TRGSIM is a level 1 and 2 trigger simulation written by J. Hauser,UCLA and tuned for the $\not{E}_T$ trigger response by A. Roodman, U. Chicago.

[54] D. Brown, A Search for Double Parton Interactions in $p\bar{p}$ collisions at $\sqrt{s} = 1.8$ TeV, Ph.D. Thesis, Harvard University, Cambridge, USA, 1989.

[55] W. Trischuk, A Measurement of the W mass in $p\bar{p}$ collisions at $\sqrt{s} = 1.8$ TeV, Ph.D. Thesis, Harvard University, Cambridge, USA, 1990.

[56] The track quality cuts are implemented by an algorithm CTCSEL writen by J.P. Berge and A. Mukherjee, Fermilab.

[57] 8 3398 1992 . CDF Collaboration, F. Abe *et al.*, Phys. Rev. Lett. **68**, 3398 (1992).

A Roodman," A measurement of $\sigma(p\bar{p} \to W \to \tau\nu)/\sigma(p\bar{p} \to W \to e\nu)$ in $p\bar{p}$ coliisions at $\sqrt{s}$=1.8 TeV", Ph.D. Thesis, University of Chicago,1992.

[58] G.C.Fox and S. Wolfram, Nucl. Phys. B **168**, 285 (1980)

[59] T. Sjostrand, Phys. Lett. B **157**, 321 (1985)

[60] R.D. Field and R.P.Feynman, Nucl. Phys. B **136**, 1 (1978)

[61] V.A. Abramovskii,O.V.Kanchelli and V.N. Gribov. " Proceedings of the XVI International Conference on High Energy Physics, National Accelerator Laboratory, Batavia, Illinois, September 1972" edited by J.D.Jackson, A. Roberts and R. Donaldson.

[62] M. Diemoz *et al.*, Z. Phys. C **39**, 21 (1988)

[63] A.D. Martin,R.G.Roberts,W.J.Stirling, Phys. Rev. D **43**, 3648 (1991)

[64] J. Gannon *et al.*, Flying Wires at Fermilab, Proceedings of the 1989 IEEE Particle Accelerator Conference, March 1989, Edited by F. Bennet and J. Kopta, p.68.

[65] C.D. Moore *et al.*, Single Bunch Intensity Monitoring system using an improved Wall Current Monitor , Proceedings of the 1989 IEEE Particle Accelerator Conference, March 1989, Edited by F. Bennet and J. Kopta, p.1513.

[66] M. Bozzo *et al.*, UA4 Collaboration, Phys. Lett. B **147**, 392 (1984).

[67] S. Belforte and K. Goulianos, CDF internal note 256,1984

[68] T. Hessing, Ph.D Thesis, Texas A&M University, 1991.

T. Hessing, CDF internal note 1247, 1991

[69] CDF collaboration Phys. Rev. D 45 3921 (1992)

CDF collaboration Phys. Rev. Let. Lett. 64 148(1990)

CDF collaboration Phys. Rev. Lett. 64 148(1990

[70] F.A. Berends *et al.*, Nucl. Phys. B **357**, 32 (1991)

[71] CDF Collaboration, Abe *et al.*, Phys. Rev. Lett. **71**, 500 (1993).